UCRL-19666

c.2

FAR INFRARED STUDIES OF SOLIDS:
I. ELECTRONIC LEVELS OF d^1 IONS IN Al_2O_3
II. PHONON CONTRIBUTION TO ELECTROMAGNETIC ABSORPTION IN LEAD

Richard Ross Joyce
(Ph. D. Thesis)

August 1970

AEC Contract No. W-7405-eng-48

RECEIVED
LAWRENCE
RADIATION LABORATORY

SEP 22 1970

LIBRARY AND
DOCUMENTS SECTION

TWO-WEEK LOAN COPY

This is a Library Circulating Copy which may be borrowed for two weeks. For a personal retention copy, call Tech. Info. Division, Ext. 5545

UCRL-19666

c.2

25

LAWRENCE RADIATION LABORATORY
UNIVERSITY of CALIFORNIA BERKELEY

DISCLAIMER

This document was prepared as an account of work sponsored by the United States Government. While this document is believed to contain correct information, neither the United States Government nor any agency thereof, nor the Regents of the University of California, nor any of their employees, makes any warranty, express or implied, or assumes any legal responsibility for the accuracy, completeness, or usefulness of any information, apparatus, product, or process disclosed, or represents that its use would not infringe privately owned rights. Reference herein to any specific commercial product, process, or service by its trade name, trademark, manufacturer, or otherwise, does not necessarily constitute or imply its endorsement, recommendation, or favoring by the United States Government or any agency thereof, or the Regents of the University of California. The views and opinions of authors expressed herein do not necessarily state or reflect those of the United States Government or any agency thereof or the Regents of the University of California.

Contents

Abstract v

I. Introduction 1

II. Spectroscopic Techniques 5

A. Fourier Transform Spectroscopy 6

B. The Michelson Interferometer 10

C. Data Acquisition and Analysis 11

D. Noise in Fourier Spectroscopy 13

1. Lock-in Detection 14

2. Periodic Sampling 15

III. Bolometers 19

A. Bolometer Theory 19

1. Responsivity 19

2. Bolometer Noise 21

3. Design of an Optimum Bolometer 26

B. Bolometer Construction and Testing 29

1. Selection of suitable Material 29

2. Bolometer Mounting 31

3. Sensitivity Tests 33

IV. Experiments on Al_2O_3 Doped with Ti, V, and Cr 38

A. Introduction 38

B. Experimental Techniques 39

1. Experimental Apparatus 39

2. Sample Materials 40

C. Experiments with $Al_2O_3:Ti^{3+}$ and $Al_2O_3:V^{4+}$ 41

1. Crystalline Field Levels of d^1 Electrons in Al_2O_3 . . 42

2. Experimental Results 43

3. Comparison with MWS Theory 44

4. Conclusions 47

D. Ruby Experiments 48

E. $Al_2O_3:V^{3+}$ Experiments 50

V. Far Infrared Absorption Experiments on Lead 53

A. Introduction 53

B. Experimental Techniques 55

1. Experimental Apparatus 55

2. Sample Preparation 58

3. Data Analysis 58

C. Experimental Results 59

D. Discussion 62

1. Golden Rule Calculation 62

2. Corrections to the Phenomenological Theory 67

3. Nonlocal Calculation of R_S/R_N 69

E. Dirty Lead Experiments 70

VI. Conclusions 74

Acknowledgements 76

Appendix 77

A. A Fast Fourier Transform for the IBM 1620 77

References 84

Tables 88

Figure Captions 90

Figures 95

FAR INFRARED STUDIES OF SOLIDS:
I. Electronic Levels of d^1 Ions in Al_2O_3
II. Phonon Contribution to Electromagnetic Absorption in Lead

Richard Ross Joyce

Department of Physics, University of California
and
Inorganic Materials Research Division,
Lawrence Radiation Laboratory,
Berkeley, California 94720

ABSTRACT

Far-infrared spectroscopic techniques are used to study the low-lying electronic levels of impurity ions in Al_2O_3 and the electromagnetic absorptivity of Pb. The transmission spectra of Al_2O_3 doped with Ti, V, and Cr are measured in applied magnetic fields up to 55 kOe. The behavior of absorption lines due to the ions Ti^{3+} and V^{4+} is discussed in terms of a theoretical description of the energy levels of a single d electron in the Al_2O_3 crystalline field modified by a dynamic Jahn-Teller effect. An absorption line attributed to V^{3+} shows magnetic field behavior consistent with a spin Hamiltonian formulation, and the spin Hamiltonian parameters are directly obtained from the spectra. The low-temperature measurements of the absorptivity of superconducting and normal Pb show an onset of absorption when the photon energy is large enough to excite appreciable numbers of acoustic phonons. Most features of the data can be explained by a "Golden Rule" calculation of

the phonon generation process proposed by Holstein. Swihart's calculations of the surface resistance are found to be in good quantitative agreement with our data.

I. INTRODUCTION

Many elementary excitations in solids have characteristic energies in the meV range and can therefore be studied by the investigation of the optical properties of the solid in the far infrared. In cases where several types of excitations are present (such as low lying electronic and vibrational states), far infrared experiments can study not only the interaction between the electromagnetic radiation and the individual excitations, but also the interactions between the elementary excitations. This paper describes two separate experiments investigating the electronic excitation spectrum in solids having vibrational states in the same energy range. The electronic excitations in one case are the discrete energy levels of the transition metal ions Ti and V in an insulator (Al_2O_3); in the other case they are the continuous excitation spectrum of the conduction electrons in a superconducting metal (Pb).

When a paramagnetic ion is placed as a substitutional impurity in a crystal lattice, the highly degenerate electronic levels of the free ion are split by the electric fields of the ions surrounding the impurity site and by spin-orbit interactions. The result is a series of sublevels which are often further split by an external magnetic field. The methods of crystal field theory[1] can be used to derive parametric expressions for the energy levels in the absence of a magnetic field; the magnetic behavior of the ground state can often be described by a spin Hamiltonian.[1,2]

Paramagnetic resonance is a powerful technique for determining the spin Hamiltonian parameters of the low-lying levels, although it cannot

be used to measure zero-field splittings much greater than 1 cm^{-1}. Estimates of zero-field splittings larger than microwave energies can be obtained by specific heat and spin-lattice relaxation measurements. Magnetic susceptibility and anisotropy measurements can provide Zeeman splitting g-factors for the low-lying energy levels. Because each of these techniques usually determines only one or two of the spin Hamiltonian parameters, several experiments are required to obtain a reasonably complete description of the system. However, high frequency magnetic resonance measurements, utilizing far infrared spectroscopic techniques, can directly measure the zero-field splittings and spin Hamiltonian parameters.

We have used far infrared techniques to investigate the low-lying electronic states of Ti and V in Al_2O_3. We measured the transmission spectra of crystals of Al_2O_3 doped with Ti and V over the frequency range 5-200 cm^{-1} in applied magnetic fields up to 52 kOe. This method can be thought of as high frequency, high field paramagnetic resonance, with the ability to continuously vary both the frequency and magnetic field. Our results for the d^1 ions Ti^{3+} and V^{4+} yielded a sufficient number of spin Hamiltonian parameters to allow a quantitative comparison with a recent theory[3] of the energy levels of a d electron in Al_2O_3 including the effects of the interaction with the vibrational modes of the Al_2O_3 lattice. In addition, we were able to obtain all three spin Hamiltonian parameters for the d^2 ion V^{3+} in one experiment.

The technique of far infrared spectroscopy can be used with equal success in studying the electronic states in a metal by measurement of the absorptivity. This method has been used to confirm the prediction[4]

of a gap in the electromagnetic absorption spectrum of a superconductor.[5] Such research has generally been confined to the frequency region below 50 cm^{-1}.

The purpose of our experiment was to extend the frequency range of investigation to include the phonon frequencies. The acoustic phonons in a metal cannot interact directly with the electromagnetic radiation, but the presence of an electron-phonon interaction makes possible the indirect excitation of phonons by radiation, with the electrons acting as intermediaries. This would result in an increase in the electromagnetic absorption when the photon energy is large enough to create appreciable numbers of phonons. This effect was postulated by Holstein,[6] who estimated that the increase in absorptivity at optical frequencies due to phonon creation should be comparable in magnitude to the anomalous skin effect absorption[7] due to the excitation of the conduction electrons.

We have measured the absorption spectrum of pure Pb in the superconducting and normal states over the frequency region 15-340 cm^{-1}. The zone boundary phonon frequency region (35-80 cm^{-1}) lies well within our observing range, and the very strong electron-phonon coupling in Pb was expected to make any effects due to phonon creation quite large. Our absorption spectra show increases at the expected frequencies, and the details of the absorption can be fit quite well to a Golden Rule calculation of phonon generation.

This paper is organized as follows: Section II includes a discussion of the techniques of Fourier Transform spectroscopy and a description of the Michelson interferometer used in our experiments.

In Section III we describe the design and construction of the doped-Ge bolometers used as far infrared radiation detectors. In Section IV we describe the experiments on Al_2O_3 doped with Ti, V, and Cr. Section V describes our investigation of the phonon creation contribution to the absorptivity of Pb and includes a comparison of our results to the predictions of a phenomenological theory of phonon generation.

II. SPECTROSCOPIC TECHNIQUES

Experiments involving the measurement of the optical properties of a material over a wide region of the far infrared frequency range (2-300 cm^{-1}) have traditionally relied on the Hg arc lamp as a source of broadband radiation. Such experiments utilize only the very low frequency part of the blackbody radiation distribution of the Hg lamp, which may provide only a few microwatts throughout the far infrared region. Higher power levels are available from several gas laser lines[8] in this region, but these are useful only in certain solid state experiments (such as magnetic resonance or cyclotron resonance), where the effect can be tuned to the laser frequency. Recent developments in non-linear optics[9,10] have shown that far infrared difference frequency radiation can be generated by the interaction of two visible or near infrared laser beams in a non-linear crystal. Such methods can presently generate continuously tunable radiation from 1-250 cm^{-1}, but they are neither simple nor reliable enough to be used as standard sources in spectroscopic experiments. For the present, at least, we must still use the Hg arc in conjunction with a grating monochromator or an interferometer.

The monochromator uses a dispersive grating and two sets of slits to select a small region of the broadband spectrum sent into it. Aside from the technical problems of eliminating higher-order "false-energy", this method is very wasteful of the small amount of energy available in the far infrared. The experiments described in this thesis use a Michelson interferometer and the techniques of Fourier Transform spectroscopy. The output of the interferometer contains all frequencies in the broadband of radiation entering it and thus wastes far less

energy than does the monochromator. The interferometer serves only to modulate the energy in a precisely determined manner so that the frequency spectrum can be obtained.

A. Fourier Transform Spectroscopy

Fourier Transform spectroscopy has been described fully[11,12] in the literature, and only a brief description of the method will be presented here. In a Michelson interferometer, collimated broadband radiation is split into two beams, one of which is allowed to travel a distance Δ further than the other before they recombine. If the input radiation distribution $S(\nu)$ is monochromatic, that is, $S(\nu)=S(\nu_o)\delta(\nu-\nu_o)$, it is easy to show that the intensity output of the interferometer as a function of the path difference Δ is:

$$I(\Delta) = 1/2\ S(\nu_o)\ (1 + \cos 2\pi\nu_o\Delta). \qquad (1)$$

For a broadband distribution $S(\nu)$, this generalizes to:

$$I(\Delta) = 1/2 \int_o^\infty S(\nu)(1+\cos\ 2\pi\nu\Delta)d\nu = 1/2 I(0) + 1/2 \int_o^\infty S(\nu)\ \cos 2\pi\nu\Delta d\nu. \qquad (2)$$

The last integral in (2) is the cosine Fourier Transform of $S(\nu)$; inversion of the Fourier Transform yields

$$S(\nu) = 2 \int_o^\infty F(\Delta)\ \cos\ 2\pi\nu\Delta\ d\Delta \qquad (3)$$

where $F(\Delta) = I(\Delta) - 1/2\ I(0)$ is called the interferogram. In practice, one samples the interferogram at a finite number N of regular, discrete

points ($\Delta = n\Delta_o$). The integral in Eq. (3) is then converted to a sum and transformed on a high-speed digital computer. The calculated spectrum is

$$S(\nu) = 2\Delta_o[1/2F(0) + \sum_{n=1}^{N} F(n\Delta_o) \cos(2\pi n\nu\Delta_o)]. \qquad (4)$$

The sampling and truncation of $F(\Delta)$ has several effects on $S(\nu)$:

(a) The choice of Δ_o determines the maximum frequency calculated from Eq. (4). The sampling theorem says that this frequency is given by $\nu_{max} = \frac{1}{2\Delta_o}$; radiation at higher frequencies is "aliased down" into the region $0 < \nu < \nu_{max}$. An analogous situation occurs in the Brillouin Zone formulation of the states of an electron in a periodic lattice. In practice, one must use a low-pass filter to cut off radiation above ν_{max}.

(b) Truncation of $F(\Delta)$ at Δ_{max} leads to a finite resolution. A useful way to consider the problem is to use the convolution theorem. The convolution of two functions is defined by

$$h(x) = f(x) * g(x) = \int_{-\infty}^{\infty} f(u)\, g(x-u)\, du. \qquad (5)$$

This leads to the convolution theorem, which can be stated

$$FT[f(x)\, g(x)] = FT(f(x)) * FT(g(x)) \qquad (6)$$

i.e., the Fourier Transform of a product of two functions equals the convolution of the Fourier Transforms of the individual functions. When $f(x)$ and $g(x)$ are symmetric about zero (as they will be in the following

discussion), we can limit the integral in Eq. (5) from 0 to ∞ and use the Cosine Fourier Transform (CFT) in Eq. (6).

An interferogram $F(\Delta)$ truncated at Δ_{max} can be written $F'(\Delta) = \text{rect}\ (\Delta/\Delta_{max}) \cdot F(\Delta)$, where

$$\text{rect}\ (x) = \begin{cases} 1 & |x| < 1 \\ 0 & |x| > 1. \end{cases} \tag{7}$$

From Eq. (6) the spectrum $S'(\nu) = \text{CFT}\ [\text{rect}(\Delta/\Delta_{max}) \cdot F(\Delta)]$ $= \text{CFT}[\text{rect}(\Delta/\Delta_{max})] * \text{CFT}(F(\Delta)) = \text{CFT}[\text{rect}(\Delta/\Delta_{max})] * S(\nu)$. The spectrum of a truncated interferogram is therefore the convolution of the spectrum of the untruncated interferogram and the CFT of the truncating function.

As an example, consider a monochromatic input $S(\nu) = \delta(\nu-\nu_o)$. $\text{CFT}\ [\text{rect}\ (\Delta/\Delta_{max})] = \sin\ (2\pi\nu\Delta_{max})/2\pi\nu$, so the calculated spectrum is

$$\begin{aligned} S'(\nu) &= \Delta_{max} \int_o^\infty \frac{\sin(2\pi\nu'\Delta_{max})}{2\pi\nu'\Delta_{max}}\ \delta(\nu-\nu_o-\nu')\ d\nu' \\ &= \Delta_{max}\ \frac{\sin\ [2\pi(\nu-\nu_o)\ \Delta_{max}]}{2\pi(\nu-\nu_o)\ \Delta_{max}} \\ &= \Delta_{max}\ \ \text{sinc}\ \ [(\nu-\nu_o)\ \Delta_{max}]. \end{aligned} \tag{8}$$

The expression (Eq. (8)) is often called the instrumental scanning function (ILS) since it gives the instrumental response to a δ-function line. The sinc function has large sidelobes which fall off in amplitude only as $(\nu-\nu_o)^{-1}$ and are therefore appreciable in magnitude several resolution widths away from ν_o. These sidelobes, or feet, on Eq. (8) are especially

annoying because they may distort nearby features of the spectrum. These can be reduced considerably by multiplying the interferogram in Eq. (4) by a function which goes smoothly to zero at Δ_{max} (apodization), thus removing the discontinuity there.

The most significant advantage of Fourier Transform spectroscopy over grating spectroscopy is the enhancement of signal to noise on the spectrum. To illustrate this, we consider the observation of a broadband spectral region divided into N resolution widths during a total observing time T. A grating monochromator spends a time T/N observing the radiation from each resolution width. An interferometer, however, "looks" at the total spectrum at each position, and therefore observes each resolution width for the time T, a gain in time by a factor of N over the monochromator. If the noise is independent of the signal, this corresponds to a gain in the spectral signal-to-noise ratio of a factor of $N^{1/2}$. This is the multiplex or Fellgett advantage[13] realized in Fourier spectroscopy. Because of the cosine modulation term in Eq. (1), the average power output of an interferometer is 50% of the input, so the Fellgett advantage is thus $1/2N^{1/2}$. In most discussions the factor 1/2 is ignored by assuming equal energy available for detection.

The problem of overlapping spectral orders is also eliminated, and the only filtering requirement is a single low-pass filter to eliminate radiation above ν_{max}. These advantages far outweigh the disadvantage of obtaining data (the interferogram) which is not in a readily interpretable form. The presence of a nearby computing facility made this disadvantage a minor one in our case. Furthermore, with experience, one can extract the major features of a spectrum by visual inspection of the interferogram.

B. The Michelson Interferometer

The Michelson Interferometer which we constructed for use in the far infrared is illustrated in Fig. 1. It is quite similar to one described by Richards.[12] The blackbody radiation from a General Electric UA-3 Hg-arc lamp is collimated by f/1.5 optics and directed onto the beamsplitter, which is a thin film of Mylar tightly stretched on a hoop. After reflecting from the fixed and movable mirrors, the radiation is recombined and focused into a 1.1 cm i.d. light pipe, through which it is conveyed to the sample and detector. The radiation is chopped so that phase-sensitive detection techniques can be used. The interferometer and light pipe can be evacuated to remove water vapor, which has strong absorption lines in the far-infrared.

Several filtering methods could be employed to eliminate unwanted high-frequency radiation. Black polyethylene at the output of the interferometer removes virtually all radiation above 500 cm^{-1}. Lower cutoff frequencies could be obtained by use of Yoshinaga filters[14] mounted on a filter wheel at the interferometer output; these consist of polyethylene impregnated with various ionic compounds and could provide cutoff frequencies as low as 50 cm^{-1}. Still lower cutoff frequencies could theoretically be obtained by zero-order polyethylene transmission gratings[15] which scatter wavelengths shorter than the grating spacing out of the optical axis of the interferometer. These were not very effective in practice because they had to be placed before the chopping motor. Thus the chopped signal contained not only the modulated radiation transmitted by the filter but also the unmodulated room-temperature blackbody radiation of the filter itself. This resulted in a large

amount of unmodulated signal which seriously degraded the modulated signal-to-noise ratio. This could be avoided in the future by placing the chopper as close to the source as possible, preferably before the beamsplitter. The beamsplitter itself has (approximately) a $\sin^2(\nu/d)$ efficiency due to interference in the Mylar film of thickness d. This was used to advantage by choosing the beamsplitter thickness so that its first efficiency minimum occurs at the cutoff frequency ν_{max}, thus aiding in eliminating frequencies beyond ν_{max}.

The movable mirror is advanced by a stepping motor which is programmed to turn through a given angle of rotation each cycle. Since data are taken at regularly-spaced values of path difference, stepping the mirror in this manner makes the "dead time" spent moving between points a small fraction of the total running time.

The mechanical accuracy of the interferometer was very good, considering the size (15 cm) of the optics. The Mylar beamsplitter (20 cm. dia.) was flat enough to provide good modulation out to 700 cm^{-1}, the limit of the black polyethylene filter. The stepping motor could position the movable mirror to within .1μ; during a one-hour run the zero path difference point would rarely shift by more than 1μ. This dimensional stability made it possible to obtain good spectra to 500 cm^{-1}.

C. Data Acquisition and Analysis

A block diagram of the experimental setup is shown in Fig. 2. The chopped output of the interferometer is directed through the sample (for a transmission experiment) onto a doped Ge-bolometer operated at 1.2°K. The signal from the bolometer is amplified by a George 620 lock-in amplifier where it is converted to a dc voltage; the voltage is

measured by a digital voltmeter and recorded on punched cards.

Once the zero path difference point (the first point of the interferogram) is found, the operation of the system is automatic. The mirror is advanced by Δ_o, and data are taken for sufficient time to provide a good signal-to-noise, the result is punched on an IBM card, and the mirror is advanced again. The mirror advance and voltmeter integration are initiated by cam switches driven by a timer motor; this cycle is repeated N times, and provides the interferogram recorded in a form suitable for immediate analysis.

It was often desirable to know the results of one run before proceeding to the next one. An IBM 1620 computer was locally available to provide rapid recovery of the spectrum from the digitally recorded interferogram. This was done by computing

$$S_m = \Delta_o[1/2\ F_o + \sum_{n=1}^{N} F_n \cos(\frac{\pi mn}{N})] \qquad (9)$$

where $F_n=F(n\Delta_o)$, $S_m=S(m\nu_{min})=S(m\nu_{max}/N)$. This method, although direct, is slow, since an N point spectrum requires N^2 operations of cosine computation, multiplication, and addition. The calculation for N=200 took 10 minutes of computing time. We have recently instituted the use of a fast Fourier Transform program based on an algorithm[16] invented by Cooley and Tukey. This program, which is described in Appendix A, requires only $N \log_2 N$ operations, and will compute a 200-point transform in 20 seconds.

Problems can arise if the first point of the data is not exactly at zero path difference, since the method of cosine Fourier Transformation

requires the interferogram to be symmetric about $\Delta = 0$. If there is an error ε in locating the zero path difference point, then the argument of the cosine term in Eq. (3) becomes $2\pi\Delta(\nu-\varepsilon)$, and sine terms will appear in the computed spectrum. This will distort spectral lineshapes and even cause the spectrum to become negative at high frequencies. Computational methods exist[17,18] for the determination of ε from the interferogram and the subsequent correction of the spectrum. Fortunately, our Michelson interferometer could be set sufficiently close to $\Delta = 0$ to make any phase error negligible.

D. Noise In Fourier Spectroscopy

If we make successive measurements of the signal from the detector, we observe a degree of fluctuation around some average value. As a matter of definition, we call the average value the signal and the standard deviation of the fluctuations about this value the noise. In far-infrared experiments most of the noise is due to unavoidable thermal fluctuations in the detector and noise in the first stage of amplification of the signal. In the next chapter, we will discuss the minimization of this noise in more detail. The present discussion is concerned with methods of enhancing the signal-to-noise, i.e., amplifying as much of the (weak) signal and as little of the noise as possible. Our experimental technique is to chop the radiation signal at a frequency ω_o, amplify the resultant ac voltage signal from the detector with a lock-in amplifier, and integrate the dc output with a digital voltmeter for a predetermined time. This process is periodically repeated at successive points of the interferogram. We now discuss the

effect of these operations on the signal-to-noise.

1. Lock-in Detection

A lock-in amplifier is a wide-band high-gain amplifier followed by

(a) narrow band amplification

(b) phase sensitive detection

(c) a low pass filter

The power spectrum after the wide-band amplifier can be represented by Fig. 3(a). It consists of a signal component at ω_o, a "white" background due to detector noise, and a contribution $\propto\omega^{-1}$ from the amplifier.

The narrow band amplification (a) amplifies the power spectrum in a region $\Delta\omega_1$ centered at ω_o, and cuts out the signal outside this region. This is illustrated in Fig. 3(b).

In the phase detection (b), the ac signal is multiplied by an ac square wave at frequency ω_o. The power spectrum is just the Fourier Transform of the product of these two, and by use of the convolution theorem, this is the convolution of the FT of the square wave with the power spectrum into the phase detector. A square wave symmetric about zero voltage (Fig. 3(c)) has frequency components at ω_o, $3\omega_o$, $5\omega_o \ldots$. Convolving this with the signal power spectrum centered at ω_o will reproduce the signal power spectrum at frequencies $\omega = 0$, $2\omega_o$, $4\omega_o$, $6\omega_o \ldots$, as shown in Fig. 3(d). It is important to note that narrow-banding must occur before phase detection; if this were not done, the broad band noise power components at $3\omega_o$, $5\omega_o$, $7\omega_o, \ldots$ would overlap $\omega = 0$ by the convolution with the square wave spectrum.

A low pass filter (c) is necessary to eliminate the power spectrum components at $2\omega_o$, $4\omega_o, \ldots$ and is also useful in decreasing the width

$\Delta\omega_1$ of the noise spectrum about $\omega = 0$. By using an electronic RC filter of time constant $\tau = RC$, the width of the power spectrum can be decreased to $\Delta\omega_2 \simeq \tau^{-1}$ (Fig. 3(e)). Since $P(\omega)$ is a symmetric function, the figures show only the positive frequency scale, and the vertical scale has been doubled.

2. Periodic Sampling

The output signal from the lock-in illustrated in Fig. 3(e) thus contains a signal component at $\omega = 0$ and a noise component consisting of frequencies from 0 to $1/2\tau$. In our experiment this signal is integrated by a digital voltmeter for a time T_1; if digitizing noise is negligible, this is equivalent to reducing the noise band width to $1/T_1$. Thus the noise power bandwidth should be reduced by a factor T_1/τ and the signal-to-noise increased by $(T_1/t)^{1/2}$, as shown in Fig. 4(a). However, when an interferogram is being measured, the integration mentioned above is repeated with a period T_2. This periodic sampling can be seen to introduce extra noise into the integrated signal, in the sense that the signal-to-noise ratio of a periodically repeated (N times) measurement will increase more slowly than $N^{1/2}$. As an example, consider a noise component whose period is not an integral submultiple of T_1 or T_2. This component, integrated over T_1, will have a non-zero value whose modulus is the same for each successive integration interval. But because T_2 is not an integral number of periods, the phase of this noise signal will shift with each measurement, resulting in a slow modulation of the digital signal. In this way high frequency noise ($\omega < 1/2\tau$ though) can produce low frequency ($\omega < 1/T_2$) modulation of the interferogram.

A more sophisticated way to look at this is to consider the successive sampling as phase-sensitive detection at a frequency $1/T_2$ with an "on" time $T_1 < T_2$. This sampling function and its frequency spectrum are shown in Fig. 4(b). The power spectrum is similar to that for the lock-in amplifier with two exceptions:

(a) The sampling function is not symmetric about zero amplitude so it has a component at $\omega = 0$ (corresponding to the ability to measure a dc voltage) in addition to those at $\omega = 1/T_2, 3/T_2, 5/T_2 \ldots$.

(b) Unless $T_1 = 1/2T_2$, the amplitude of the nth harmonic components is not proportional to $1/n$.

The resultant power spectrum is obtained by the convolution of the sampling power spectrum with the spectral output of the lock-in amplifier followed by integration for a time T_1. The result is shown in Fig. 4(c). Note that the bandwidth of the output is still $1/2T_1$, as in Fig. 4(a), but there is additional noise power which will appear in this bandwidth (shaded area) because of convolution with higher harmonics of the sampling function. Thus the effective power bandwidth may be several times larger than that expected from a single integration for time T_1.

One solution to this might be to increase the lock-in time constant τ to $1/T_2$, thus cutting off the harmonic contributions to the noise. This is incompatible with our step-and-integrate method of sampling the interferogram, in which the "dead time" T_2-T_1 must be several times τ to allow the mirror to be advanced and the dc output of the lock-in to come to its new value. Since $T_2-T_1 < T_2$, it is impossible to make $\tau \sim T_2$ and use the step-and-integrate method because the large τ would distort the interferogram considerably. This distortion would be a

function of the path difference Δ and the relative values of T_1, T_2, and τ. A possible way to eliminate this distortion is to use a lock-in amplifier which discharges the time constant capacitor to zero during the period of mirror advance. This would entail minor modifications to the lock-in amplifier we used and might well be worthwhile.

If we advance the mirror continuously at a constant speed, there is a linear relationship between time and path difference. Although use of a large τ would still badly distort the interferogram, this linear relation makes it theoretically possible to define an average path difference during the integration time as well as a phase function which describes the distortion of the interferogram at each point. It would then be possible to recover the original interferogram.

Noise on a continuously driven interferogram appears as wiggles which can be thought of as corresponding to high frequency radiation modulated by the interferometer. If the sampling interval Δ_o is chosen to be small enough to sample the highest frequency interferogram noise, then the value of τ can be made small enough so that the interferogram obtained by continuous driving is undistorted. This value of Δ_o can define a ν_{max} considerably larger than that of the radiation signal present, in which case a large part of the computed spectrum will contain noise but no signal (Fig. 4(d)). The noise on the signal from 0 to ν_c will be smaller as a result of this oversampling; if Δ_o were chosen to be $1/2\nu_c$, the noise from ν_c to ν_{max} would be aliased back into the region $0 - \nu_c$. This method entails taking considerably more data points, however.

from the conduction band. This simplified model is supported by our experiments, which show that the resistivity obeys an approximate $e^{\Delta/T}$ dependence at low temperatures, and that the material is partially transparent to radiation of energies $\hbar\omega < k\Delta$. For our calculations we assume the material is characterized by an electrical resistance $R \propto e^{\Delta/T}$ and a large temperature coefficient of resistance $\alpha = \frac{1}{R}\frac{dR}{dT} = -\Delta/T^2$. Figure 5 shows a typical operating configuration. The bolometer element is mounted in a vacuum, supported by its electrical leads, which provide a thermal conductance G between the bolometer and a heat sink at a low temperature T_s. The bolometer element and electrical leads have a heat capacity C. The bolometer absorbs a fraction ε of the chopped radiation signal $P_1 e^{i\omega t}$ and the background radiation P_o, and responds with a temperature $T_o + T_1 e^{i\omega t}$ and resistance $R_o + R_1 e^{i\omega t}$. The resistance R_1 due to the signal is measured by biasing the detector with a constant current I and measuring the ac voltage IR_1 with a lock-in amplifier.

The total power input to the bolometer is $P_{in} = I^2R_o + \varepsilon P_o + \varepsilon P_1 e^{i\omega t} + I^2R_1 e^{i\omega t}$. Applying the energy conservation equation $C\frac{dT}{dt} + G(T-T_s) = P_{in}$ we get

$$\varepsilon P_o + I^2R_o - G(T_o - T_s) + [\varepsilon P_1 + I^2R_1 - GT_1 - i\omega CT_1]\, e^{i\omega t} = 0. \qquad (10)$$

The first three terms determine the operating temperature $T_o = T_s + (\varepsilon P_o + I^2R_o)/G$ due to the dc power input. The ac term can be simplified by writing $T_1 = R_1\, dT/dR = R_1/R_o\alpha = R_1T_o^2/R_o\Delta$. This gives

$$\varepsilon P_1 + R_1\left[I^2 + \frac{T_o^2(G+i\omega C)}{R_o\Delta}\right] = 0. \qquad (11)$$

Defining a time constant $\tau = C/G$, we can solve for the ac resistance signal

$$R_1 = \frac{-R_o \Delta\varepsilon P_1}{I^2 R_o \Delta + G T_o^2 (1+i\omega\tau)} . \tag{12}$$

The responsivity $S = IR_1/P_1$ is the measured voltage signal for unit signal power:

$$S = \frac{-R_o \Delta\varepsilon\ I}{I^2 R_o \Delta + G T_o^2 (1+i\omega\tau)} . \tag{13}$$

In an experiment, the relevant criterion of detector quality is the minimum signal which can be detected, usually called the noise-equivalent power (NEP). The desirable goal of minimizing the NEP is not automatically achieved by maximizing S, since there are circumstances in which the dominant source of noise is dependent on other parameters. It is therefore necessary to consider the contribution of each noise source to the total detector noise, in order that the dominant source be identified. In the following we will express the mean square NEP as a sum of various contributions to the detector noise, and consider its minimization in terms of the responsivity S and the bolometer parameters appearing in Eq. (13).

2. Bolometer Noise.

In a Ge bolometer, there are often several noise sources of comparable magnitude. These are Johnson noise, phonon noise, background radiation intensity fluctuations, and current noise. Since the experimental noise is measured at the output of the amplifier connected to the detector, it is important to also consider the amplifier contribution, which is quite

dependent on the relative impedances and temperatures of the detector and amplifier, and can often dominate the system noise.

a. Johnson noise. The Johnson noise of a resistor, which results from the dissipation of thermally induced current fluctuations, is given by

$$\bar{V}_J = (4kTRB)^{1/2} \tag{14}$$

where B is the noise bandwidth. Dividing this by the responsivity expresses this noise in terms of an optical noise power incident on the bolometer.

$$\bar{P}_J = (4kT_oR_oB)^{1/2}/S. \tag{15}$$

b. Phonon noise. Another contribution to the detector noise arises from random fluctuations in the phonon flux between the detector and the heat sink through the thermal link G. The resultant noise power is given by[22]

$$\bar{P}_T = (4kT_o^2\ GB)^{1/2}. \tag{16}$$

c. Background radiation noise. Fluctuations in the radiation from the source and from the room temperature background can also contribute to detector noise. The mean square noise power from a radiator at temperature T_R can be written[22]

$$\overline{P_R^2} = \frac{1}{2\pi}\,\Omega\,AB \int_0^\infty \frac{P(\nu)h\nu e^{h\nu/kT_R}\,d\nu}{(e^{h\nu/kT_R}-1)} \,. \tag{17}$$

Here Ω is the solid angle subtended by the body at the detector (assumed small compared to 2π), and A is the detector area. A focusing cone (Fig. 5) is commonly used to limit the field of view to one which just includes the image of the Hg arc source. A larger field of view would increase only the signal due to the background. The acceptance angle θ of the cone should thus be determined by the f-number of the spectrometer (for our f/1.5 optics, $\theta \approx 20°$). Eq. (17) can then be written

$$\overline{P_R^2} = 8\beta\,A\,\sigma\,kT_R^5 \sin^2(\tfrac{\theta}{2})\,B. \tag{18}$$

The factor β takes into account the bolometer absorptivity, the emissivity of the radiator, and the effects of any filters in the system. For the purposes of analysis, we can define $\beta A\,\sigma\,T_R^4 \sin^2(\frac{\theta}{2}) = W$, the power absorbed by the detector, in which case Eq. (18) assumes the simple form

$$\overline{P_R^2} = 8\,k\,T_R\,WB. \tag{19}$$

One source of this noise is the room temperature blackbody radiation from the mirrors and uncooled filters in the interferometer. For our f/1.5 system with room temperature black polyethylene filtering, $W \approx 10^{-5}$ watt, and $\overline{P_R^2} \approx 10^{-24}$ watt^2. This can be reduced considerably by coating the inside of the light pipe with soot, which absorbs high frequency radiation and re-radiates at a much lower temperature. In this case, θ is nearly the line-of-sight angle subtended by the room temperature background,

which is about 10^{-2} for a 1 m length of 1 cm dia light pipe. Cooled filters in the light pipe can reduce the background even more. A cold sapphire window, for example, will remove radiation above 200 cm^{-1}. Under these conditions, $W \approx 10^{-8}$ watt, and $\overline{P_R^2} \approx 10^{-27}$ $watt^2$.

The signal from the Hg arc source will also have fluctuations which contribute to radiation noise. For a typical transmission experiment, $W \sim 10^{-9}$ watt, and estimating the source temperature to be $T_R \sim 2000$ K, $\overline{P_R^2} \sim 2.5\times10^{-27}$ $watt^2$. For a signal power equal to the NEP (which we will assume to be smaller than 10^{-9} watt), the background radiation noise power $\overline{P_R} \approx 3\times10^{-14}$ watt is the contributing factor.

d. Current noise. Little is known about current noise theoretically. It is often found in carbon resistors and semiconductors, but appears to be absent in wire wound resistors. Experimentally, current noise can usually be expressed as

$$\overline{P_c} = (F\ I^{\gamma}\ \nu^{-\beta}\ B)^{1/2}\ /S \qquad (20)$$

where F is a constant, γ is near 2, and β is normally about 1. By use of single crystal bolometer material and carefully constructed electrical contacts, it appears possible to reduce current noise to a negligible value.[19]

e. Amplifier noise. The bolometer-amplifier circuit we used is shown in Fig. 6(a). For the purpose of analyzing the noise in this circuit, we replace each resistor with an equivalent noiseless resistor and a noise voltage source, as illustrated in Fig. 6(b). The load resistor R_L at temperature T_L produces a mean square voltage noise $e_L^2=4kT_LR_LB$;

the amplifier input resistance R_I at the amplifier temperature T_A produces $e_I^2 = 4kT_A R_I B$. The detector voltage noise $e_s^2 = 4kT_o R_o \alpha B$, where α includes the contribution of noise sources other than Johnson noise. In addition, we define an amplifier noise resistance R_A by $e_A^2 = 4kT_A R_A B$, where e_A is the measured input noise of the amplifier with the input shorted. The current generator i_g represents the grid current noise in the amplifier. This can be determined by measuring the mean square input noise with the terminals open, which is $e_A^2 + i_g^2 R_I^2 B$. This contribution will become negligible when $R_o \ll R_I$.

Following the method of Putley and Martin,[20] we can derive the noise figure (NF) for this equivalent circuit. This is defined as

$$NF = \frac{\text{Mean square noise/signal at output}}{\text{Mean square noise/signal at source}} . \tag{21}$$

For the circuit in Fig. 6b, with R_I, $R_L \gg R_A$, we obtain

$$NF = 1 + \frac{T_A}{\alpha T_o}\left[\frac{R_o T_L}{R_L T_A} + \frac{R_o}{R_I} + \frac{R_A}{R_o}\right] + \frac{i_g^2}{4kT_o R_o \alpha}\left[\frac{1}{1/R_I + 1/R_o + 1/R_L}\right]^2 . \tag{22}$$

From Eqs. (21) and (22) and the definition of e_s^2, we can obtain the mean square voltage noise/signal at the output. Division of this by S^2 expresses the voltage noise in terms of an optical noise power, thus giving the mean square NEP:

$$(NEP)^2 = \frac{4kT_o R_o B}{S^2} + 4kT_o^2 GB + 8kT_R WB + \frac{FI\gamma_\nu - \beta_B}{S^2}$$

$$+ \frac{4kT_A R_o B}{S^2}\left[\frac{R_o T_L}{R_L T_A} + \frac{R_o}{R_I} + \frac{R_A}{R_o}\right] + \frac{i_g^2 B}{S^2}\left[\frac{R_I R_L R_o}{R_I R_L + R_I R_o + R_L R_o}\right]^2 . \tag{23}$$

The first four terms are the detector noise sources described previously. The last two terms are the amplifier noise contribution, which in the limit $R_o \ll R_I$, R_L reduces to the mean square amplifier input noise power $4kT_A R_A B/S^2$. In general, it is dependent on the bolometer resistance R_o, and can be the dominant contribution when $T_A \gg T_o$.

3. Design of an Optimum Bolometer.

We can now make several general comments regarding minimizing the NEP, which is clearly a desirable goal in bolometer design. The first, fourth, fifth, and sixth terms in Eq. (23) can, in theory, be made arbitrarily small by increasing the responsivity. For this reason, it is desirable to maximize S, both by judicious choice of the bolometer parameters during construction, and by use of the proper bias current during an experiment. The third term can be reduced by the use of cooled filters. The ultimate NEP of the bolometer is thus determined by the phonon noise, and is given by the second term in Eq. (23).

In the remainder of this section, we will assume that the experimental variable (the current) is always set to maximize the responsivity for a given bolometer. We will then consider the effect of the design parameters on S and the NEP. The current dependence of S will be discussed in the following section on bolometer testing.

Maximizing Eq. (13) with respect to I gives the operating current $I_m = [G\, T_o^2(1+i\omega\tau)/R_o\Delta]^{1/2}$, for which

$$S_m \approx -\varepsilon/2I_m = -\varepsilon\, R_o^{1/2}\, \Delta^{1/2} \,/\, 2G^{1/2}\, T_o(1+i\omega\tau)^{1/2}. \qquad (24)$$

Because the parameters in Eq. (24) are not independent, it is worthwhile

to consider maximizing S_m in terms of the conditions available to the experimenter: the temperature, the bolometer size and doping, and the electrical lead geometry.

(a) Changing the temperature has pronounced effects on S_m, since it enters not only explicitly as T_o, but also implicitly in $G(\propto T_o)$, $t=C/G\ (\propto T_o^2)$, and $R_o(\propto e^{\Delta/T_o})$. It is clearly desirable to make T_o as small as possible; Drew and Sievers[23] report that decreasing T_o from 1.5 K to 0.4 K leads to an increase in S_m by two orders of magnitude. In practice, T_o is a rather inflexible parameter determined by the type of cryogenic system used. We used a pumped He^4 cryostat capable of attaining a bath temperature $T_s \sim 1.1$ K. Depending on the bolometer, T_o ranged from 1.3 K to 1.5 K.

(b) The bolometer doping determines the parameter Δ. Transmission experiments have shown[24] that Δ corresponds to an effective band gap, and that radiation of energy $< k_B\Delta$ is not absorbed efficiently by the material. Therefore, for the purposes of maximizing S, it is desirable to increase Δ (and thus R_o) until the resulting decrease in ε becomes important.

In practice, it is usually more important to choose Δ so that R_o minimizes the amplifier noise contribution to the NEP. From Eqs. (23) and (24), we can see that the only dependence of the NEP on R_o occurs in the amplifier noise terms (we are neglecting any consideration of the bolometer current noise). Minimizing this with respect to R_o yields the optimum condition

$$R_{om}^2 = \frac{R_A}{T_L/R_L T_A + 1/R_I + i_g^2/4kT_A} . \qquad (25)$$

For our amplifier system, $T_L = T_A = 300$ K, $R_L, R_I \approx 10^7\ \Omega$, $i_g \approx 10^{-13}$ amp/Hz$^{1/2}$, and $R_A \approx 2\times10^4\ \Omega$, for which the optimum bolometer resistance $R_{om} \approx 2\times10^5\ \Omega$. For our cryogenic system and bolometer dimensions, this condition restricts the useful values of Δ to the range 8 - 10 K. For a He^3 cryostat,[23] values near 4 K are appropriate.

(c) The size of the bolometer is often determined by the experimental requirements that it be large enough in area to intercept the desired radiation and thick enough to be highly absorbing. Further increases in these dimensions will have little effect on ε, but will increase the heat capacity C. If we are operating in the region $\omega\tau > 1$, Eq. (24) shows that $S_m \propto C^{-1/2}$.

The electrical leads furnish the thermal conductance G between the bolometer and the heat sink. When we insert S_m from Eq. (24) into Eq. (23), we find that all terms in the mean square NEP, except background radiation fluctuations, are proportional to G. It is clearly desirable to minimize G. Unless the system is dominated by phonon noise, the effective lower limit on G (keeping the other parameters constant) is provided by the condition that the thermal response of the detector be rapid enough to follow the chopping modulation of the radiation signal. Using the definition of $\tau = C/G$, this requires that $G \gtrsim \omega C$. For the operating condition $\omega\tau = 1$, the mean square NEP can be written

$$(\mathrm{NEP})^2 \approx \frac{20kT_o^3\omega CB}{\varepsilon^2\Delta} + 4\,kT_o^2\omega CB + 8k\,T_R WB + \frac{20\,kT_A T_o^2 R_A \omega CB}{\varepsilon^2\Delta\,R_{om}} + \frac{6\,i_g^2 R_{om} T_o^2 \omega CB}{\varepsilon^2\Delta}\,. \tag{26}$$

Here we have assumed the bolometer current noise to be negligible and have set the terms in brackets in the fifth term of Eq. (23) equal to R_A/R_{om}, and have assumed $R_{om} \ll R_I, R_L$ in the last term. It is found for most amplifiers that the input noise resistance R_A varies as ω^{-1} at low frequencies, so the fourth term in Eq. (26) is actually frequency independent. Eq. (26) does show the motivation for making ω and C as small as possible. In practice, we determine C by the minimum volume for efficient absorption, select the chopping frequency to be as slow as is convenient (we used values between 11 Hz and 42 Hz), and adjust the bolometer lead length until $\omega\tau \approx 1$.

B. Bolometer Construction and Testing

1. Selection of Suitable Material

All of the bolometers we constructed were made from single crystals of Ga-doped Ge. Three pieces of material were initially available, of which only one was found to be suitable for 1.2 K bolometer construction. The room temperature resistivities ranged from 0.11 to 0.18 Ω-cm, but these values were only roughly correlated with the low temperature behavior. The energy gap parameter Δ is extremely sensitive to impurity concentration, and small scale fluctuations in concentration were found to produce 20 per cent differences in Δ between two bolometers cut from adjacent positions in the original crystal. The only way to determine the suitability of bolometer material is to obtain Δ by low temperature resistivity measurements.

Several chips about 4 mm square and from 0.5 mm to 0.7 mm thick were cut from each sample of doped Ge. The area was made large enough to cover the exit hole of the focusing cone (Fig. 5), whose diameter is

determined by the throughput of the spectrometer. The throughput is defined as the product of the aperture and the solid angle subtended by the detector, and is constant for an optical system. The output of our spectrometer is focused by an f/1.5 mirror ($\Omega \approx .15\ \pi$) into a light pipe about 1 cm^2 in area, so the minimum output area of the focusing cone (for which $\Omega = 2\pi$) is 0.07 cm^2, corresponding to a diameter of 3 mm. A smaller exit would not pass all of the f/1.5 radiation; a larger one would project the radiation into a solid angle smaller than 2π. The thickness requirement was determined from transmission measurements of a piece of 0.5 mm thick material, which was opaque above 30 cm^{-1}, but transmitted about 30 per cent at 10 cm^{-1}.

These chips were etched in a solution of 5 parts HNO_3, 3 parts CH_3COOH, and 3 parts of 30 per cent H_2O_2. Several cm of #34 Cu wire (0.16 mm dia.) were soldered to opposite edges with In solder. We found that good contacts could be made using a regular soldering iron and $ZnCl_2$ flux, as long as great care was taken to avoid contamination of the soldering tip or the flux with materials which could form a p-n junction in the solder joint. We then made resistivity measurements of these chips between 4.2 K and 1.2 K to determine Δ.

Only a narrow range of Δ was desirable for our bolometers. One of the pieces of source material had a characteristic value $\Delta \sim 3$ K which is too small for a 1.2 K bolometer, although it would be quite acceptable for a He^3 bolometer.[23] Another piece had $\Delta \gtrsim 15$ K, too large to produce bolometers with acceptable low-frequency absorptivity. Chips out from the third piece had $7 < \Delta < 10$ K and $10^4 < \rho < 5\times10^4$ Ω-cm at 1.2 K. All of our bolometers were made from this material.

2. Bolometer Mounting

The chips which were determined to have values of Δ in the desirable range were mounted as shown in Fig. 5. The electrical leads were glued into a hole in an Al heat sink, which in turn was glued to a wall of the bolometer cavity, which is in intimate thermal contact with the He bath. The length of the leads between the bolometer and Al heat sink was chosen to provide the optimum value of G for the particular bolometer; as determined by the chopping frequency and an estimate of the heat capacity C of the bolometer, solder, and electrical leads.

A typical chopping frequency in our experiments is 33 Hz, for which $\omega = 208\ \mathrm{sec}^{-1}$. Satisfying the optimum operating condition $\omega\tau = 1$ then requires $\tau \simeq 5$ msec. The heat capacity of Ge at these temperatures is due to the lattice, and has the approximate value

$$C_{Ge} = 6.8\times10^{-2}\ T^3 V \quad \mathrm{erg/K^4 - mm^3}. \tag{27}$$

For an 11 mm^3 bolometer at a typical operating temperature T_o=1.4 K, C_{Ge}=2.6 erg/K. The heat capacity of the In solder (typically 2 mg) is $\approx$ 0.2 erg/K at this temperature. The electronic heat capacity of the 0.18 mm dia. Cu leads can be written

$$C_{Cu} \approx 0.4\ T\ell \quad \mathrm{erg/cm\ -K^2} \tag{28}$$

where ℓ is the length of each lead. Thus, at T=1.4 K, the total heat capacity $C=C_{Ge}+C_{In}+C_{Cu} \approx (2.8+0.6\ell)$ erg/K.

The thermal conductivity of the Cu wires is proportional to tempera-

ture in this range, and assuming a value $\kappa = 1$ W/cm -K at T=1 K, the thermal conductance of the two leads is

$$G \approx 4\times10^3\ T\ell^{-1} \quad \text{erg -cm/sec - K}^2. \tag{29}$$

At T = 1.4 K, $G \approx 5.6\times10^3\ \ell^{-1}$ erg - cm/sec - K. Solving the equation $C/G = \tau = 5$ msec leads to a solution for the length of the leads $\ell = 5$ cm, with C = 5.8 erg/K and $G = 1.1\times10^{-4}$ erg/sec - K.

Initial tests with an existing bolometer indicated that a lead length of about 1.5 cm was sufficient to make $\tau \approx 5$ msec, which implied a lead thermal conductance smaller by a factor of four than that given by Eq. (29). One explanation for this discrepancy is that the Cu wire we used for our leads has a thermal conductivity smaller than the handbook value. A more serious possibility is that the glue bond between the leads and the heat sink is poor. This is undesirable because the temperature of the Cu leads is then very close to the elevated value T_o, rather than being distributed between T_o and T_s along the length of the wire. This will make C_{Cu} larger. Furthermore, such a tenuous thermal link can change with time, resulting in erratic performance.

These results indicate that our bolometer mounting is probably not an optimum design. A more flexible method would involve the use of very thin electrical leads of a poor thermal conductor. The thermal link is then provided by a He exchange gas. This has the dual advantages of substituting the small heat capacity of the He gas for that of the Cu leads, and of providing a thermal conductance which can be varied during the course of an experiment.

3. Sensitivity Tests

Aside from the absorptivity, ε, the responsivity of a bolometer can be measured by purely electrical means. Jones[21] discusses several methods for doing this, all of which use the known electrical heating power in the bolometer as the power input. Our method is to measure the current-voltage characteristic (load curve), which contains all the information necessary to determine the dc responsivity. The dc responsivity is, from Eq. (13),

$$S(0) = -\varepsilon/I(1+GT_o^2/I^2R_o\Delta). \tag{30}$$

The second term in the denominator can be written

$$\frac{GT_o^2}{I^2R_o\Delta} = -\frac{G}{I^2R_o\alpha} = -\frac{1}{I^2}\frac{dP}{dT}\frac{dT}{dR} = -\frac{1}{I^2}\frac{dP}{dR} \equiv -H. \tag{31}$$

Since the only power input is the dc heating $P = I^2R_o$, $H = d(\log P)/d(\log R)$, and

$$S(0) = \varepsilon/I(H-1). \tag{32}$$

This is obtained by plotting the load curve on log-log paper. A 45° rotation transforms the log I and log V coordinates into log P and log R, and the slope of the load curve with respect to the latter set of coordinates is H. Figure 7 shows the load curve for our best bolometer, along with the dc responsivity calculated from Eq. (32).

Since the experimental quantity of interest is the responsivity at

the chopping frequency, ω, it is necessary to calculate $S(\omega)$ from Eq. (13). Using the fact that $H(\omega) = H(1+i\omega\tau)$, the responsivity can be written in the intuitive form

$$S(\omega) = S(0)/(1+i\omega\tau_e) \tag{33}$$

where

$$\tau_e = H\tau/(H-1). \tag{34}$$

Eq. (34) indicates that τ_e is a function of the bias current I, so the dynamic responsivity curve cannot be obtained from the dc responsivity curve by a constant multiplicative factor. This is illustrated in Fig. 8, where the dc responsivity (circles) is plotted along with a measured ac response curve, which was obtained by illuminating the bolometer with a chopped radiation signal of unknown magnitude and plotting the lock-in amplifier output as a function of I. In practice, we determined τ_e for a particular value of I (and H) by measuring the frequency dependence of the bolometer response to a chopped radiation signal and using Eq. (33). We could then determine $\tau_e(I)$ from Eq. (34) and calculate the dynamic responsivity. The results of this approach are indicated by the squares in Fig. 8. The shape of the curve outlined by these points is a considerably improved fit to the experimental curve.

Eqs. (33) and (34) are approximate in that they ignore the effects of a finite load resistance R_L in the bias current supply and the temperature dependence of $\tau = C/G$. The former situation is discussed

by Jones,[21] and is of little consequence here, since we always kept $R_L \gg R_o$ in our experiments. The latter problem is more serious, since it is difficult to treat analytically. However, we found that calculation of τ as a function of current, using calculated values of C and measured values of $G = I^2R/(T_o-T_s)$ gave values of τ which were almost constant over the range 2μa - 15 μa; furthermore, this τ was quite close to that determined experimentally by measuring $S(\omega)$. The approximations inherent in Eqs. (33) and (34) are thus relatively unimportant, and the poor fit in Fig. 8 at small current is probably due to the inaccuracy in measuring the very large slope of the load curve (relative to log R) in this region. For this reason, we used the experimental responsivity curve to determine the optimum operating current, and fit the theory to the experiment in the range 10 μa - 20 μa to obtain the scale factor for the experimental curve.

We also determined the NEP by measuring the rms noise voltage at the output of the amplifier with no chopped radiation signal incident on the bolometer and dividing this by the responsivity.

The measured parameters for our best bolometer are presented in Table I. The values of S, NEP, e_s, R_o, T_o, and I_{op} are those at the minimum NEP. The values I_m and S_m are those at the maximum S, which often occurs at a different operating point when amplifier noise predominates. Because amplifier noise (Eq. (23)) depends on both S and R_o, it will not necessarily be minimized either at S_m or the value of R_{om} given by Eq. (25). G was obtained from the load curve and the measured $R_o(T)$ curve. The value of τ obtained by dividing the theoretical heat capacity by the experimental G was quite close to the experimental

value. The load curve analysis thus provides a quite accurate method of bolometer calibration, although the calculations for the dynamic responsivity can be tedious. We found it more efficient to test several bolometers at once by mounting them in a cavity in such a way that they were illuminated by approximately equal amounts of radiation. By using a calibrated bolometer as a control, the responsivities of the others could be obtained by measurement of the relative responses to the applied radiation.

In Fig. 9 we show the NEP calculated from Eq. (23), using the measured values of T_o, R_o, G, and S for several values of I. The two curves represent the NEP for the conditions $T_L = T_A = 300$ K (our experimental condition), and $T_A = 300$ K, $T_L = 4$ K (obtained by cooling the load resistor). The background radiation noise power was calculated to be 3×10^{-14} watt from Eq. (19), but an error in this estimate would have negligible effects on the NEP, since the amplifier noise was by far the dominant factor. The open terminal input noise was measured to be $\sim 1\mu v/Hz^{1/2}$, corresponding to a grid current noise $i_g \sim 10^{-13}$ amp/$Hz^{1/2}$.

The experimental NEP (points) shows the same general current dependence as the theoretical curve, and the quantitative agreement is very good except at very small bias current. As indicated in Fig. 9, the operating current I_{op} is different from I_m, the current at maximum responsivity. This indicates that we are limited by the noise in the amplifier. Insertion of the bolometer parameters at I_{op} into Eq. (23) shows that the amplifier Johnson noise and current noise make approximately equal contributions which are about 50 times larger than the mean square detector noise.

Severe amplifier noise limitation is difficult to avoid in a system consisting of a room temperature amplifier and a low temperature detector. The other theoretical curve in Fig. 9 shows the value of cooling as much of the amplifier system as possible. Helium temperature load resistors have been used by Low[19] and others, and could reduce the NEP of our system by 10 per cent. The more radical solution of cooling the amplifier would achieve a spectacular reduction in NEP (provided the current noise also decreases with temperature), although this is not practical at present.

In summary, we have constructed bolometers with measured values of NEP as low as 9×10^{-13} W/Hz$^{1/2}$ at a chopping frequency of 42 Hz. Our analysis indicates that this could be reduced by 10 per cent by cooling the load resistor. Because the amplifier noise is the dominant factor, further reductions in NEP can be obtained only by increasing the responsivity. Low[25] has achieved an NEP of 3×10^{-14} W/Hz$^{1/2}$ by decreasing the bolometer volume to 0.2 mm^3 (which allows a consequent reduction of G), but such a small bolometer would be inefficient in intercepting much radiation in our experimental configuration. A highly desirable alternative is the use of He^3 cryogenics to reduce T_o to 0.4 K; with such a system, Drew and Sievers[23] have constructed a bolometer 8 mm^3 in volume with an NEP = 3×10^{-14} W/Hz$^{1/2}$.

IV. EXPERIMENTS ON Al_2O_3 DOPED WITH Ti, V, and Cr

A. Introduction

Our first experimental program with the apparatus described above was the investigation of the transmission properties of Al_2O_3 doped with Ti, V, and Cr over the frequency range 5 cm^{-1} - 120 cm^{-1} in applied magnetic fields up to 55 kOe. Previous zero field experiments on Al_2O_3 doped with Ti and V by Nelson *et al*[26] and Wong *et al*[27] had shown absorption lines which they attributed to transitions between the electronic levels of Ti^{3+} and V^{4+} in the Al_2O_3 lattice. Their assignment was reinforced by calculations made by MacFarlane, Wong, and Sturge[3] (MWS) of the expected energy levels of a single d electron in the Al_2O_3 crystalline field modified by a dynamic Jahn-Teller effect. The lines attributed to Ti^{3+} had been seen by previous workers, and there was a degree of controversy over their assignment. Very similar lines were observed by Hadni[28] in a ruby sample with no suspected Ti impurity. They were later observed in Ti-doped Al_2O_3 by Perry.[29] More recently, Moser *et al* had observed the same lines in samples of Al_2O_3 doped with Ti, V, and Cr. Since the line strengths did not seem to correlate with spectrographic analyses of Ti impurity, they were attributed to lattice vibrational modes.[30] Our magnetic field experiments were expected to resolve this discrepancy and to provide a critical test of the (MWS) theory in the event the absorption lines were due to the Ti and V impurities.

The samples we measured included Ti, V, and Cr doped material studied by Nelson[26] and Wong[27] and Ti and Cr doped material used by Moser *et al*.[30] Our results confirm the assignment to

electronic levels of Ti^{3+} and V^{4+} and all in reasonably good agreement with the MWS theory. In addition, we investigated an absorption line near 8 cm^{-1} in the V-doped sample. Our magnetic field results confirmed the assignment of this line to a low-lying electronic level of the $(d)^2$ ion V^{3+}. We obtained an excellent fit to the theoretical magnetic field dependence derived from a spin-Hamiltonian.

B. Experimental Techniques

1. Experimental Apparatus

The cryostat which we constructed for transmission measurements in a magnetic field is shown in Fig.10 . The sample is mounted in a light pipe which can be removed from the cryostat, and samples can be changed without appreciable loss of He. The NbZr superconducting solenoid is capable of producing a field of 55 kOe. Radiation from the Michelson interferometer described in Section II is directed through the sample to the detector chamber, where it is focused by a light cone onto the detector. We used our best In-doped Ge bolometer, which had an NEP $\approx 10^{-12}$ $W/Hz^{1/2}$. The radiation exiting from the cone is distributed over a hemisphere, so the bolometer is mounted in a non-resonant integrating cavity to maximize the absorption. The detector chamber is thermally separated from the sample cavity and has its own He tank which can be pumped to provide the low temperature necessary for efficient bolometer operation. Because of the excellent radiation shielding provided by the surrounding 4.2 K He, bolometer temperatures as low as 1.0 K could be reached. The sapphire windows used to separate the bolometer vacuum jacket from the sample cavity also served as a cooled

filter to eliminate room temperature background radiation.

All of our experiments on Al_2O_3 were done with the sample at 4.2 K, as shown in Fig.10. Temperatures as low as 1.5 K could have been obtained by pumping on the large He bath. When elevated temperatures are desired, the vent holes shown in Fig.10 can be closed and the sample cavity evacuated. A sample insert with a heater can provide temperatures to 50 K. This feature has been used to investigate low critical temperature ferromagnets and transitions which are relatively insensitive to magnetic field.[31]

2. Sample Materials

The samples used for our primary investigations were crystals of Ti, V, and Cr doped Al_2O_3 used by Nelson[26] and Wong.[27] These had been carefully grown to assure that only the nominal impurity was present in any appreciable quantity. This was important in light of our suspicion that the "vibrational modes" observed by Moser *et al* may have been due to trace amounts of unintentional Ti impurity in all of his samples.

The Ti-doped samples were single crystals about 1 cm in diameter and 1 to 5 mm thick, some of which had the optic axis (referred to here as the $\underset{\sim}{c}$ axis) in the plane of the crystal (and thus perpendicular to the magnetic field), while others had the $\underset{\sim}{c}$ axis normal to the plane. By doing experiments on both types we were able to orient our solenoidal magnetic field both parallel to and perpendicular to the $\underset{\sim}{c}$ axis. X-ray analysis of these crystals confirmed these orientations to within 3°. The concentration of Ti was 0.15 per cent by weight of the oxide; it is not known how much of this was in the 3+ oxidation state.

The Al_2O_3:V crystal was approximately a cube 1 cm on a side. The V concentration was 0.3 per cent by weight of the oxide, corresponding to ~ .15 wt per cent of V. Slack[32] estimated the concentration of V^{3+} at about 0.06 wt per cent from optical absorption experiments; the remainder was V^{2+} and V^{4+}. During his experiments, Wong had irradiated the sample with X-rays, resulting in the net reaction $h\nu + 2V^{3+} \rightarrow V^{4+} + V^{2+}$. Both the V^{4+} and V^{2+} concentrations approximately tripled from previously small values as a result of this treatment. The V^{4+} concentration in our experiments was thus about 0.04 wt per cent.

The Al_2O_3:Cr sample was a single crystal 15 cm long and 1.5 cm in diameter. The Cr concentration was 1 per cent by weight of the oxide.

In addition, we measured the transmission of four of Moser's samples, two of which were heavily doped (2 per cent and 5 per cent) with Cr, and one which was approximately 0.1 per cent V. All of these samples had Ti concentrations of less than 20 ppm by spectrographic analysis.

The samples were mounted on a disc of crystal quartz which was wedged to prevent interference effects. The quartz disc was fastened to the sample holder, with the sample sticking into the light pipe. A short section of light pipe butted against the quartz on one end and extended close to the sapphire window at the bottom; this method minimized the gaps in the light pipe, which are very wasteful of radiation. When this was installed in the cryostat, the sample was immersed in the liquid He, so its temperature was maintained at 4.2 K.

C. Experiments with $Al_2O_3:Ti^{3+}$ and $Al_2O_3:V^{4+}$

Our initial experiments on Ti and V-doped samples yielded zero-field

transmission spectra which were consistent with Wong's[26] and Nelson's[27] results. In the $Al_2O_3:Ti^{3+}$, absorption lines were seen at 37.8 cm^{-1} and 107 cm^{-1}. A similar pair of lines at 28.1 cm^{-1} and 53 cm^{-1} was observed in the V-doped sample. Furthermore, the lower frequency line in each sample was observed to split in a magnetic field applied parallel to the $\underset{\sim}{c}$ axis. This behavior supports the assignment to Ti^{3+} and V^{4+} ions, but is inconsistent with the assignment to vibrational modes[30] or exchange-coupled Cr^{3+} ions.[28] The similarity of the lines in the Ti and V samples (one narrow line at low frequency and a broader one at a higher frequency) further supports this assignment, since Ti^{3+} and V^{4+} are isoelectronic and should have similar electronic levels. Our following experiments studied the magnetic behavior of the lines with the intention of providing a quantitative test of the MWS theory of d^1 electronic levels in Al_2O_3.

1. Crystalline Field Levels of d^1 Electrons in Al_2O_3

In the samples studied, the impurity ion is assumed to be substituted directly for an Al^{3+} ion. The Al^{3+} lattice symmetry is trigonal, but the six O^{2-} ions adjacent to an Al site lie at the corners of a not too badly distorted octahedron; thus the crystalline field seen by an ion substituted for Al is largely cubic with a small trigonal distortion. Both Ti^{3+} and V^{4+} have an electronic configuration consisting of a closed Ar shell and a single 3d electron. The lowest levels of these ions are thus those corresponding to the single d electron. The ground state of the free ion, a tenfold degenerate ^2D level, is split by the cubic and trigonal crystalline fields into an upper level having E_g symmetry and lower A_{1g} and E_g levels. In addition, the lower E_g

level is split by spin-orbit coupling and the upper E_g level is split by the Jahn-Teller effect.[33] The resulting configuration is shown in Fig.11. Only the three lowest levels, labeled $E_{3/2}$, ${}_1E_{1/2}$, and ${}_2E_{1/2}$ in order of increasing energy, are of interest in our experiment. These levels are Kramers doublets, which can be split only by an external magnetic field. The magnetic behavior can be described by the spin-Hamiltonian

$$\mathcal{H}_n = g_{n\parallel}\beta\, S_z H_z + g_{n\perp}\beta\,(S_x H_x + S_y H_y) \qquad (35)$$

where n=1,2,3 refers to the $E_{3/2}$, ${}_1E_{1/2}$, and ${}_2E_{1/2}$ states, respectively, and the $\parallel$ and $\perp$ subscripts refer to magnetic fields parallel to and perpendicular to the $\underset{\sim}{c}$-axis. This behavior is illustrated in Fig.11.

2. Experimental Results

Our zero field experiments described above showed two absorption lines for each of the Ti and V doped samples. These correspond to the transitions δ_1 and δ_2, which are 37.8 cm^{-1} and 107 cm^{-1} for Ti^{3+}, and 28.1 cm^{-1} and 53 cm^{-1} for V^{4+}. Unfortunately, the higher frequency transition in each sample was quite broad, and observation of its Zeeman splitting would have been difficult in the available magnetic field. The 107 cm^{-1} and 53 cm^{-1} had full widths at half the peak value of absorption coefficient of about 19 cm^{-1} and 8 cm^{-1}, respectively. The corresponding linewidths for the δ_1 transitions were about 1 cm^{-1} for each case. Therefore we were only able to determine the values of g_o and g_1.

When a magnetic field was applied to the Ti-doped samples with

$\underset{\sim}{c} \parallel \underset{\sim}{H}$, the 37.8 cm^{-1} line split into four lines as indicated in Fig. 12. The effect of the thermal depopulation of the upper Zeeman level of the ground state at 4.2 K was clearly seen. Because we are observing transitions between two Zeeman split doublets with g-factors g_o and g_1, the difference transitions shown in Fig.12 appear to split with g-factors $g_a = 1/2(g_o+g_1)$ and $g_b = 1/2(g_o - g_1)$. We thus obtain parallel g-factors $g_{o\parallel} = 1.11 \pm 0.03$ and $g_{1\parallel} = 2.00 \pm 0.06$. When the samples were oriented with $\underset{\sim}{c} \perp \underset{\sim}{H}$, no broadening or splitting of the 37.8 cm^{-1} line was observed, implying that the perpendicular field g-factors for both the ground and first excited states are less than 0.1.

The results for the V-doped sample were quite similar. The splitting of the 28.1 cm^{-1} line in a magnetic field parallel to $\underset{\sim}{c}$ is shown in Fig. 13. The three-line pattern is a special case of the four-line pattern of Fig.12 which occurs when the g-factors of the two Zeeman split levels are the same. This interpretation is reinforced by the strength of the central line, which as about twice that of the stranger of the two satellite lines. Our data indicate that $g_{o\parallel} = g_{1\parallel} = 1.43 \pm 0.04$. With $\underset{\sim}{c} \perp \underset{\sim}{H}$, no splitting of the 28.1 cm^{-1} line occurred, indicating $g_{o\perp}$, $g_{1\perp} < 0.2$.

Our results for g_o in both the Ti and V-doped samples are in good agreement with previous results obtained by electron paramagnetic resonance. Two groups[34, 35] have measured values of $g_{o\parallel} = 1.07$ and $g_{o\perp} < 0.1$ for $Al_2O_3:Ti^{3+}$. Merritt[36] obtained a value of $g_{o\parallel} = 1.39$ in $Al_2O_3:V^{4+}$.

3. <u>Comparison with the MWS Theory</u>

Our experimental observations of two zero field transitions which display a Zeeman effect are in qualitative agreement with the static crystalline field theory of d^1 electronic states illustrated in Fig.11.

Attempts to obtain a quantitative fit are, however, unsuccessful. The energy eigenvalues $\delta_o = 0$, δ_1, and δ_2 can be expressed in terms of the cubic field parameter Δ, the trigonal field parameter v, and the spin-orbit parameter ζ. Using representative values for v and ζ and the measured value of Δ, MWS obtained $\delta_1 = 109\ cm^{-1}$, $\delta_2 = 771\ cm^{-1}$ for Ti^{3+}, and $\delta_1 = 169\ cm^{-1}$, $\delta_2 = 831\ cm^{-1}$ for V^{4+}. Clearly, the static crystalline field theory is unable to account for the experimental observations.

MWS extended the crystalline field picture by considering the interaction between the d^1 electronic levels and the vibrational modes of the Al_2O_3 lattice. Because the vibrational, trigonal crystalline field, and spin-orbit perturbations are of the same order of magnitude, the calculations are quite complicated. Only a brief description of the theory will be given here, along with the results of our attempts to fit our data to the theory.

Because the cubic crystalline field strength is very large, the octahedral $^2T_2$ and ^2E levels are taken as the unperturbed system, and the interaction with the lattice is a perturbation on this system. This interaction results in a physical displacement of the electronic system to a new position of minimum potential energy and lower crystalline field symmetry. This phenomenon is known as the static Jahn-Teller effect. The gain in the Jahn-Teller potential energy (E_{JT}) is balanced by the loss in elastic energy due to the displacement from the equilibrium position. The interaction of the octahedral $^2T_2$ level in Al_2O_3 with the lattice vibrational mode considered by MWS results in three equivalent configurations to which the system can distort, and in the static Jahn-Teller effect, the electronic system randomly occupies one of these

three energy minima, provided $k_BT << E_{JT}$. The lower symmetry at this new position splits the previously degenerate level; Fig. 11 illustrates this effect on the upper octahedral ^2E level.

The $^2T_2$ level does not exhibit this static distortion, because the added trigonal and spin-orbit perturbations are comparable in magnitude with E_{JT}. These perturbations will cause rapid transitions between the three Jahn-Teller potential minima. This dynamic Jahn-Teller effect results in a partial averaging of the trigonal and spin-orbit perturbations, as illustrated in Fig. 14.

To first order, this causes a reduction of all of the trigonal and spin-orbit matrix elements by a constant factor γ (the Ham effect[37]). This correction is insufficient to explain the experimental data, since the Ham effect reduces the values of δ_1 and δ_2 by the same multiplicative factor, whereas the experimental values for Ti^{3+} are, respectively, 0.35 and 0.14 of the estimated static crystalline field values.

The MWS theory treats the dynamic Jahn-Teller effect to second order within the manifold of basis states for the $^2T_2$ level and between the basis states for $^2T_2$ and those for ^2E. They obtained analytical expressions for the energy splittings δ_1 and δ_2 and the parallel field g-factors g_o, g_1, and g_2. The independent variables involved are the trigonal and spin-orbit parameters v and ζ, and the Ham quenching factor $\gamma = \exp(-3E_{JT}/2\hbar\omega)$, where $\hbar\omega$ is the energy of the vibrational mode responsible for the Jahn-Teller effect.

These analytical expressions of MWS were fitted to our experimental data for Ti^{3+} and V^{4+}. We used a trial and error method to obtain values of v, ζ, and E_{JT} which gave close agreement between the theoretical

and experimental values of δ_1 and δ_2. The values of v, ζ, and E_{JT} were then used to calculate g_o, g_1, and g_2. This process was then repeated many times in an attempt to fit the theoretical values of g_o and g_1 to our experimental results. Several results of this procedure are tabulated in Table II, along with the data. The analytical expressions are quite complicated and sufficiently sensitive to a small change in some of the variables to make the fit somewhat arbitrary.

4. Conclusions

Our experiments on $Al_2O_3:Ti^{3+}$ and $Al_2O_3:V^{4+}$ strongly indicate that the observed absorption lines are due to the low-lying electronic states of the nominal impurity ion in the effective crystalline field of the Al_2O_3 lattice. The Zeeman splitting of the low-frequency absorption line in each case shows that they cannot be due to lattice vibrational modes. The general agreement of our results with the MWS theory leads to the conclusion that the vibrational interaction correction to the static crystalline field can largely explain the electronic levels of a d^1 impurity ion in Al_2O_3. As shown in Table II, this agreement is not perfect. Since our fit was made by adjustment of the parameters to fit only two of the five variables (δ_1 and δ_2), there is considerable freedom of choice for the values of several parameters. However, the theoretical value of $g_{o\parallel}$ was rather insensitive to variations in v and ζ, and the 10% disagreement between the experimental and theoretical values of $g_{o\parallel}$ for $Al_2O_3:V^{4+}$ is probably due to the incomplete picture provided by the perturbation approach of MWS. Because V^{4+} is more positive than Ti^{3+}, the surrounding O^{2-} ions are drawn closer to the V^{4+} ions in $Al_2O_3:V^{4+}$ than to the Ti^{3+} ions in $Al_2O_3:Ti^{3+}$. Thus V^{4+} will

exhibit a more pronounced dynamic Jahn-Teller effect than will Ti^{3+}, and inadequacies of the theory become more apparent for V^{4+}. However, the 10% disagreement is not bad for a second-order perturbation approach involving three perturbations of the same order of magnitude, and the agreement is sufficient to confirm the assignment of the Ti^{3+} and V^{4+} lines. A more complete consideration of the interaction with the lattice could be expected to improve the fit with the experimental data.

D. Ruby Experiments

Because previous workers had observed absorption lines in $Al_2O_3:Cr^{3+}$ (ruby), we made transmission measurements of several ruby samples in magnetic fields in an attempt to explain their observations.

In 1964, Hadni[28] observed absorption lines in ruby at 37 cm^{-1} and 100 cm^{-1}, which he assigned to exchange coupling between pairs of Cr^{3+} ions. Exchange coupled energy levels have been indirectly observed by optical methods, but the direct transition is between states of different spin and is forbidden. Nelson et al.[26] found no absorption lines in a 15 cm long sample of 1 per cent Cr_2O_3 in Al_2O_3. We repeated the experiment with the same sample and obtained similar negative results for all values of magnetic field. These results, as well as the similarity in frequency, width, and relative strength between the lines seen by Hadni and those subsequently found for Ti^{3+} strongly suggest that he was seeing Ti^{3+} as an unintentional impurity in his ruby.

Later, Moser et al.[30] reported lines at 37.75 cm^{-1} and 108 cm^{-1} in samples of Al_2O_3 doped with Ti, V, and Cr. These were attributed to lattice vibrational modes because the line strengths did not correspond

with those expected from analyses of the amount of Ti present. However, the coincidence of their reported lines with our Ti^{3+} spectrum and the lack of any lines in our ruby sample raised doubts as to the correctness of this assignment. We performed transmission measurements on four of their samples, each of which had Ti concentration of less than 20 ppm by spectrographic analysis. We observed the line at 37.8 cm^{-1} in their two ruby samples as well as in a V-doped sample, in agreement with their observations. However, in all cases, the 37.8 cm^{-1} line exhibited a Zeeman splitting consistent with the assumption that it was due to Ti^{3+}.

Our conclusion is that Hadni's and Moser's ruby samples contained Ti^{3+} as an unintentional impurity. Although their spectrographic analyses indicated a Ti concentration of less than 20 ppm, we believe that such a concentration of Ti^{3+} would produce detectable characteristic absorption lines. This conclusion is reinforced by our transmission experiments on a 1 cm thick 1.2 per cent ruby of Swiss origin. Although the Ti concentration was only ~ 100 ppm, we found a strong absorption line at 37.8 cm^{-1} (with a peak absorption coefficient $\alpha \sim 2.4$ cm^{-1}) and at 107 cm^{-1} ($\alpha \sim 0.8$ cm^{-1}), which split in a manner indicating Ti^{3+}. The 37.8 cm^{-1} line strength was at least ten times the minimum observable value.

The lack of good correlation between the 37.8 cm^{-1} line strength and the Ti concentration given by spectrographic analysis is probably the result of a variation from sample to sample of the fraction of the Ti in the 3+ oxidation state. The use of spectrographic analysis as an indication of Ti^{3+} concentration is therefore of questionable value, because it can provide no more than an upper limit. The proportion of

Ti in the 3+ state will depend on the conditions under which the crystal was grown and aspects of its past history, such as exposure to radiation, which may temporarily oxidize some Ti^{3+} into Ti^{4+}. Wong[27] has produced large changes in V^{3+} and V^{4+} concentrations in Al_2O_3:V by radiation. The possibility also exists that the transition probability for a given ion may depend on the presence of defects or other ions (such as Cr) in close proximity.

E. $Al_2O_3:V^{3+}$ Experiments

The V^{3+} ion has two d electrons, and the effect of the Al_2O_3 crystalline field on the free-ion ^3F state, shown in Fig. 15, is more complicated than for the ^2D state of V^{4+}. Only the lowest level ($^3A_2$) is of interest here, since the trigonal splitting is believed[38] to be ~ 1200 cm^{-1}, so the mixing between the $^3A_2$ and ^3E states is small.

The sample was the same one used for the $Al_2O_3:V^{4+}$ experiments, and all measurements were done with the sample at 4.2 K. In zero magnetic field, a strong line with a peak absorption coefficient $\alpha \sim 1.5$ cm^{-1} was observed at 8.25 cm^{-1}. In a field parallel to the $\underset{\sim}{c}$ axis, this line split linearly with field. When the applied field direction was perpendicular to the $\underset{\sim}{c}$ axis, a quadratic Zeeman effect was observed. Fig. 16 shows the behavior of the 8.25 cm^{-1} line in both field orientations.

The ground ($^3A_2$) state is a spin triplet with zero orbital angular momentum. Mixing with the higher states will, however, give rise to second-order spin-orbit splitting. Because of the large trigonal splitting, such mixing is small, and the spin states $|+\rangle$, $|0\rangle$, and $|-\rangle$ are reasonably good basis states for $^3A_2$. The magnetic properties of the ground state can then be described by means of the spin-Hamiltonian

$$\mathcal{H} = DS'^2_z + g_{\parallel}\beta S'_z H_z + g_{\perp}\beta\,(S'_x H_x + S'_y H_y) \qquad (36)$$

where S' is the effective spin of the ground state ($|S'| = 1$). Mixing with the higher states will tend to quench the Zeeman splitting of the $^3A_2$ level, giving values of $g_{\parallel}$ and $g_{\perp}$ smaller than 2.0 by an amount which depends on the ratio of the spin-orbit coupling to the trigonal splitting.[2]

The first term in $\mathcal{H}$ represents the second-order spin-orbit interaction, which splits the $^3A_2$ level into two levels separated by D, the doubly degenerate M = ±1 level lying higher. The effect of a magnetic field parallel to $\underset{\sim}{c}$ is represented by the second term; this perturbation does not mix states of different M, and the M = ±1 level is split by $2\,g_{\parallel}\beta H$, as shown in Fig. 15. The third term in $\mathcal{H}$ represents a magnetic field perpendicular to $\underset{\sim}{c}$, which mixes the three spin states. This results in a quadratic Zeeman effect. Fig. 16 shows the experimental data (points) and the theoretical results (lines) obtained by adjusting $g_{\parallel}$ and $g_{\perp}$ for the best fit. An excellent fit is obtained for both field orientations, yielding the results $g_{\parallel} = 1.92 \pm 0.03$ and $g_{\perp} = 1.74 \pm 0.02$.

Our results are in excellent agreement with those of other workers. A recent microwave absorption experiment[39] yielded the results $D = 8.26 \pm 0.01\ cm^{-1}$ and $D = 8.27 \pm 0.01\ cm^{-1}$ by two different techniques. Within the limits of our experiment, we find $D = 8.25 \pm 0.02\ cm^{-1}$. Electron paramagnetic resonance experiments[40,41] have obtained the respective results $g_{\parallel} = 1.915$ and $g_{\parallel} = 1.910$. Smith and Mires[42] have measured $g_{\perp} = 1.74 \pm 0.01$ by a torque method.

The technique of far-infrared spectroscopy used in this experiment can be thought of as high-field, high-frequency electron paramagnetic resonance, with the additional ability to continuously vary the frequency. This technique allows us to measure all three spin-Hamiltonian parameters in the $Al_2O_3:V^{3+}$ experiment, which previously required three separate methods of measurement. Furthermore, the $Al_2O_3:Ti^{3+}$ experiments demonstrate the ability to measure zero-field splittings of more than 100 cm^{-1}, far above the frequencies available by microwave techniques.

V. FAR-INFRARED ABSORPTION EXPERIMENTS ON LEAD

A. Introduction

In the previous section, we described the measurement of the electronic excitation spectrum of ions in an insulator, which was seen to consist of discrete energy levels. The experiments described in this section are concerned with the excitation spectrum in a metal.

If we consider a metal to be a free electron gas at T=0, the excitation spectrum of the conduction electrons is the continuum

$$E_k = \varepsilon_k - \varepsilon_F = \hbar^2 (k^2 - k_F^2)/2m \tag{37}$$

where $\varepsilon_F = \hbar^2 k_F^2/2m$ is the Fermi energy. Because of the periodicity of the metallic lattice, the electronic states have a well-defined momentum, and the analysis of the electromagnetic absorption must consider both energy and momentum conservation selection rules.

A plane electromagnetic wave $e^{i(kx-\omega t)}$, of energy $\hbar\omega$ and free space wave vector $k=\omega/c$, normally incident on a metal has a solution inside the metal of the form $e^{i(x/\delta-\omega t)}\, e^{-x/\delta}$. This describes a wave which is attenuated in the metal over a distance δ, called the skin depth. The wave vector distribution of this wave is a continuum, $0 < k \lesssim \delta^{-1}$. Therefore, only a small portion of this power spectrum will satisfy both the energy and wave vector conservation requirements necessary to transfer energy to a particular conduction electron. Even when this process is integrated over the electronic states, the total skin-effect absorptivity of a metal is extremely small, on the order of 10^{-3}. The actual calculation of the skin-effect absorptivity is, of course, a self-consistent one.

A real metal also has excitations corresponding to the vibrational modes of the lattice. These acoustic phonons do not interact directly with electromagnetic radiation, but can interact indirectly through the electrons since there exists an interaction between the electrons and the lattice. This implies an additional mechanism for radiation absorption, in which the electromagnetic wave (photon) creates both an electronic excitation and an acoustic phonon. Since this is a second-order process, the matrix element connecting the initial and final states is considerably smaller than that for the first-order skin effect absorption process. However, the addition of the phonon to the final state provides an extra degree of freedom for satisfying the energy and wave vector conservation requirements. As a result, for photon energies large enough to excite any allowed phonon mode ($\hbar\omega > k\Theta_D$), this process could be expected to provide absorption of electromagnetic radiation comparable in magnitude to that expected from the skin effect. Holstein[6] was the first to postulate the existence and approximate magnitude of the phonon creation contribution to the absorptivity of a metal (Holstein effect) in order to account for the results of near-infrared absorptivity experiments.[43]

The calculations of Scher[44] in the phonon frequency region of a normal metal indicated that the absorption due to the Holstein process should begin around the transverse phonon frequency, increase rapidly up to the Debye frequency, and approach a high-frequency value about half that estimated by Holstein.

This chapter describes our observation of the onset of the Holstein effect in superconducting and normal Pb. We measured the far-infrared

absorption in single crystals of pure Pb over the frequency region 15-340 cm^{-1}. Pb is well-suited to this experiment, since the phonon frequencies (30-80 cm^{-1}) lie well within our observing range. Also, the electron-phonon coupling is very strong, so the Holstein effect should be correspondingly large. Finally, we could study the Holstein absorption in the superconducting and normal states of the same metal, in which the electronic excitation spectra are well-known and dramatically different.

Our experimental absorption spectra provide the first observation of the Holstein effect in the zone boundary phonon frequency region. The spectrum of the normal metal shows a dramatic increase around the transverse phonon frequency $\Omega_t \approx 35$ cm^{-1}; a more abrupt onset occurs around $\Omega_t + 2\Delta \approx 55$ cm^{-1} in the superconductor. In addition, the spectra show structure which can be correlated to the transverse and longitudinal peaks in the phonon density of states. Most features of the data can be explained by a Golden Rule calculation of the Holstein phonon generation process, which will be described in Section D. We will also discuss recent calculations[45] which indicate that the features of our data, including the Holstein effect, can be derived by a rigorous solution for the surface resistance of the metal using strong-coupling superconductivity theory.

B. Experimental Techniques

1. Experimental Apparatus

We measured the direct absorption in our bulk lead samples by a calorimetric method. The sample was illuminated by far-infrared radiation from the Michelson interferometer described in Section II, and the

temperature rise due to absorption in the sample was measured by a doped-Ge thermometer cemented to the back. Because the sample absorbs a very small fraction of the incident radiation, care must be taken to avoid spurious contributions to the signal due to resonant modes in the surrounding cavity or to direct absorption of stray radiation by the highly absorbing thermometer.

A sample mounting geometry (Fig. 17) similar to that used by Biondi et. al.[46] was employed to minimize the spurious signals described above. The sample, about 7mm × 7mm × 0.5mm in size, was soldered with In to a length of 0.15 mm wall stainless steel tubing, which provided a thermally insulating support for the sample and prevented stray radiation from falling on the thermometer. Drew and Sievers[47] employed a similar mounting technique, but they inserted a sheet of mylar between the sample and the stainless steel to reduce the thermal conductance to the stainless tube, and thus increase the sensitivity of the thermometer. However, they experienced difficulties due to leakage of radiation through the mylar insulation. The In solder joint in our apparatus was completely effective in blocking stray radiation.

The cavity itself was machined from brass, and completely filled with epoxy heavily impregnated with graphite to make it absorbing in the far-infrared. The final cavity shape was then machined to a rough finish in order to avoid highly polished parallel sections of the wall, which could produce resonant mode structure on the absorption spectra. In general, it was intended that radiation leaking between the focusing cone and the sample should require several reflections from the highly absorbing cavity walls to reach the stainless steel tubing at the back

of the sample. Because of the thermal link between the stainless steel and the sample, absorption in the support could cause heating of the sample and a spurious signal. The sample was mounted in the cavity so that the radiation baffle at the back and the light cone were very close (0.1 mm) to the sample surface. This was small enough to prevent excessive leakage and large enough to insure that dimensional changes upon cooling would not bring the sample into contact with the cavity.

The thermometer, a small (2mm × 1mm × 0.4mm) In-doped Ge bolometer, was glued to the back of the sample with GE 7031 varnish. A piece of ZIG-ZAG cigarette paper between the sample and thermometer provided good thermal conductance and electrical insulation. The thermal link to the He bath was provided by the 1 cm long 0.1mm dia. Cu electrical leads to the thermometer, which had a thermal conductance $G \approx 2\times10^{-4}$ W/K at 1.2 K.

Lead, because of its low Debye temperature, has a much larger lattice specific heat at 1.2 K than does a Ge bolometer the same size. In the superconducting state, only the lattice heat capacity is dominant at 1.2 K, with a value for our sample $C_S \approx 50$ erg/K. When the sample is driven into the normal state by a magnetic field, the electrons provide an equivalent contribution, and $C_N \approx 100$ erg/K. The large thermal time constants $\tau_S \approx 25$ msec and $\tau_N \approx 50$ msec require a slow chopping frequency for efficient operation. We used our lowest available frequency of 11 Hz. A He exchange gas cannot be used as a thermal link because it will conduct heat from the cavity walls (which absorb the radiation leakage) to the thermometer, resulting in a large spurious signal.

2. Sample Preparation

Our samples were made from large single crystals of very pure Pb. Resistivity measurements on this material gave values of the resistivity ratio (R_{300}/R_T) of 1.3×10^4 at 4.2 K and 8.5×10^4 at 1.2 K. At the latter temperature, which was that used in our experiments, the mean free path of an electron is ~ 0.4mm.

A sample about 8mm square and 5mm thick was cut from one of the large crystals using a string saw and a cutting solution of equal parts CH_3COOH and 30 per cent H_2O_2. After the stainless steel support was soldered to a square face, the sample was acid lapped to its final dimensions of 7mm square and 0.5mm thick on a cloth mat saturated with the same solution used for cutting. A final polish was obtained by agitating the sample in a solution of 4 parts CH_3COOH and 1 part 30 per cent H_2O_2 for about 10 seconds. This was immediately followed by rinsing with distilled water and ethyl alcohol, after which the surface was quickly dried with nitrogen. The rinsing and drying were necessary to prevent tarnishing of the surface. The polishing was repeated many times to obtain a clean, highly reflecting surface. The surface flatness was not critical in our experiment, and the commonly observed "orange peel" texture resulting from the acid polish was considered acceptable if the surface was clean.

3. Data Analysis

All of our absorption experiments were done at 1.2 K on samples in the superconducting state and in the normal state produced by an external magnetic field of ~ 1200 Oe applied parallel to the sample surface. Reference spectra were obtained by substituting a highly absorbing carbon

resistance bolometer for the lead sample.

Two methods of data analysis were employed. In the first, the absolute absorptivities of the superconducting and normal lead were obtained by dividing their absorption spectra by that of the carbon bolometer. Because the resonant characteristics of the sample cavity changed when the highly absorbing carbon bolometer was substituted for the highly reflecting lead sample, the data obtained from this analysis displayed structure due to cavity modes and were useful only for determining the general shape and magnitude of the absorption spectrum. Far better results were obtained by calculating the ratio of the superconducting and normal lead absorption spectra, since the structure due to cavity modes should cancel out when the ratio is computed (because the absorptivity is small in both cases).

Because of the small absorptivity of the sample, the signal-to-noise on a single spectral run was quite poor. To enhance the signal-to-noise and to minimize systematic sources of spurious structure, we did a large number of experiments on several samples in two different cavities. The resulting spectra were then averaged and standard deviation confidence levels were calculated.

C. Experimental Results

The absolute absorptivities of the superconducting and normal lead relative to the carbon bolometer are shown in Fig. 18. No significant differences were found in the spectra obtained for the (111) and (100) sample orientations, so Fig. 18 contains the average of both orientations. The solid line is the frequency-dependent (surface) absorption arising from the ordinary skin-effect theory. This was calculated from Dingle's

tables[48] using the electronic relaxation time derived from the resistance ratio measurement and Chambers' value[49] of $\sigma/\ell = 9.4\times10^{10}\ \Omega^{-1}\text{-cm}^{-2}$. The shape of this theoretical curve is not very sensitive to errors in the chosen parameters. The absolute accuracy of the measurements is poor so the scale factor is established by fitting the normal curve in the region from 25 to 40 cm^{-1} where the theory is expected to be valid. The fit in this region is probably accurate to 2 per cent. The superconducting curve is fit to the normal curve at high frequencies, where A_S/A_N is expected to be unity.

The spectrum for the superconducting sample shows a well-defined energy gap absorption edge at 22 cm^{-1} with very little signal at lower frequencies; this indicates that at least 95 per cent of this signal is due to absorption in the lead sample. Our data are in good agreement with the more recent measurements in the gap region.[5] In addition, the absorption increases sharply at about 55 cm^{-1}. A similar but less sharp increase begins at about 35 cm^{-1} in the normal sample. Although the onset of the additional absorption is slow in the normal state, it must be invoked to explain the fact that the spectrum becomes concave upward. The skin-effect theory predicts a curve which is concave downward throughout this frequency region.

The accuracy of the data in Fig. 18 decreases toward each end of the measured frequency range, as indicated by the error bars. The fine structure at high frequencies is not considered significant, since only five runs on one sample were averaged in the region from 180-340 cm^{-1}. Fig. 18 does indicate that the onset of the Holstein absorption occurs at the expected frequencies, and that its magnitude is comparable with

the skin-effect absorption for frequencies above the phonon range.

The details of the onset of absorption are seen more clearly in Fig. 19, where the ratio of superconducting to normal absorption is plotted. The ratio rises rapidly from the gap at $2\Delta=22$ cm^{-1} to a maximum at 35 cm^{-1}. The decrease from 35 to 55 cm^{-1} is due to the absorption onset in the normal spectrum. The ratio then rises in two steps, centered at ~ 65 cm^{-1} and ~ 95 cm^{-1}, which are due to the onset of absorption in the superconducting spectrum. In addition, the ratio decreases gradually in the region 120 cm^{-1} - 240 cm^{-1}, remaining constant thereafter.

Many random and systematic errors are expected to disappear from the ratio shown in Fig. 19. The data in the region from 20-180 cm^{-1} are probably accurate to ± 0.02; because of the smaller number of high frequency runs, the confidence limits above 180 cm^{-1} are ± 0.04. Thus the fine structure near 30 cm^{-1} and beyond 100 cm^{-1} is probably not significant, while the sharp feature near 85 cm^{-1} could be. The scale factor was established by setting the high frequency ratio to its expected value of unity.

As an independent check of our absorption measurements, we measured the power reaching a bolometer after many reflections in a non-resonant cavity whose walls were slabs of single-crystal Pb, a cavity used previously[50] to study energy-gap absorption edges in superconductors. The ratio of superconducting to normal absorptivity derived from this experiment was in good agreement with our direct absorption data over the range (20-130 cm^{-1}) covered in this experiment.

D. Discussion

The Holstein process involves the scattering of a conduction electron which absorbs a photon and emits a phonon. A rigorous treatment of the absorptivity due to this process involves solving the Boltzmann equation to obtain the conductivity. Holstein[51] has formulated the problem to high order in perturbation theory to obtain the Boltzmann equation for normal Pb, and Scher[44] has recently solved this to calculate the Holstein absorption in this case. The Boltzmann equation for the superconducting case is considerably more complicated, and we are not aware of any solution for Pb.

We employed the far simpler procedure of treating the Holstein process as a quantum mechanical transition and using Fermi's Golden Rule to calculate the transition probability.[52] This is equivalent to first order iteration of the Boltzmann equation, and is formulated in terms of well-known quantities for both the normal and superconducting cases.

1. Golden Rule Calculation

Our phenomenological approach assumes the conduction electrons to be a free electron gas at T=0 and explicitly includes energy conservation but not wave vector conservation selection rules. The initial state contains the full Fermi sea and a photon of energy ω; the final state is an electron of energy ε_1, a hole of energy ε_2, and a phonon of energy Ω. The density of final states is assumed to be the convolution of the independent densities of states of the electron, hole, and phonon. The Holstein volume absorptivity is then proportional to

$$P_v \propto \omega^{-1} \int N_e(\varepsilon_1)\ N_h(\varepsilon_2)\ \alpha^2(\Omega)F(\Omega)\ \delta(\varepsilon_1+\varepsilon_2+\Omega-\omega)d\varepsilon_1 d\varepsilon_2 d\Omega \tag{38}$$

where N_e and N_h are the electron and hole densities of states, and $\alpha^2(\Omega)\ F(\Omega)$ is the product of the square of the electron-phonon matrix element and the phonon density of states. The factor ω^{-1} in front of the integral is found to arise in a treatment of the Holstein process by second-order perturbation theory. The frequency dependence of the electron-phonon interaction is contained in $\alpha^2F(\Omega)$. Substitution of a constant N_o for the normal electron density of states and a BCS density of states in the superconductor gives the expressions

$$P_{vN} \propto (N_o^2/\omega) \int_o^{\omega} (\omega-\Omega)\ \ \alpha^2F(\Omega)d\Omega \tag{39}$$

$$P_{vN} \propto (N_o^2/\omega) \int_o^{\omega-2\Delta} \alpha^2F(\Omega)[(\omega-\Omega)\ E(a) - \frac{2\Delta^2}{(\omega-\Omega)} K(a)]d\Omega \tag{40}$$

for the Holstein absorptivity in the normal and superconducting states, respectively. $K(a)$ and $E(a)$ are complete elliptic integrals with $a^2 = 1 - 4\Delta^2/(\omega-\Omega)^2$.

We calculated the above integrals using the α^2F defined by

$$\alpha_o^2(\Omega)F(\Omega) = (N_o/2)\ \langle\langle |M_{kk'}|^2\ \delta(\Omega_Q-\Omega)\rangle\rangle \tag{41}$$

where the brackets indicate an average over the Fermi surface. $M_{kk'}$ is the matrix element for scattering an electron from a Bloch state $\underset{\sim}{k}$ to $\underset{\sim}{k}'$ by means of a phonon of wave vector $\underset{\sim}{Q} = \underset{\sim}{k}'-\underset{\sim}{k}$. In particular, α_o^2F can

be obtained[53] from superconducting tunneling data; we used Rowell and McMillan's values[53] of α_o^2F for Pb. Our results for P_{vS} and P_{vN} are shown in Fig. 20. The shape of our P_{vN} curve is in excellent agreement with that obtained by Scher's[44] solution of the Boltzmann equation.

We then calculated a total absorption spectrum by adding the superconducting or normal theoretical Holstein volume absorptivity P_v to the theoretical anomalous skin effect absorptivity P_s. The skin effect absorptivities are proportional to the surface resistances R_S and R_N in the superconducting and normal states. Our total absorptivities are thus

$$A_S = R_S + \gamma P_{vS}$$
$$A_N = R_N + \gamma P_{vN} \tag{42}$$

where $\gamma = P_v/P_s$ is the ratio of the Holstein and skin effect absorptivities.

(a) In his original paper, Holstein drew an analogy between the electron-phonon scattering processes involved in the Holstein effect and those involved in high-temperature ($T \gg \Theta_D$) electrical conductivity. In the limit $\hbar\omega \gg k\Theta_D$, where both P_v and P_s are independent of frequency, he estimated $\gamma = 16\ \Theta_D\delta_f/\ 15\ Tv_F\tau$. Here δ_f is the high-frequency skin depth c/ω_p), and T is the temperature, large compared to Θ_D, at which the phonon-limited relaxation time τ is evaluated. The composite absorption in this high-frequency limit has been used successfully to fit the near-infrared absorptivity in copper and silver at low tempera-

tures.[54] Using the experimental value $\sigma/\ell = 9.4\times10^{10}\ \Omega^{-1} - \mathrm{cm}^{-2}$ and McLean's value[55] for the London penetration depth $\lambda_L = c/\omega_p = 305$ Å, we estimate $\gamma = 1.9$. We found, however, that a reasonable fit to our data required the smaller value $\gamma \approx 1$. This is quite close to Scher's result $\gamma \approx 0.9$. We would expect Scher's estimate to be more correct, since his theoretical treatment included higher order phonon scatterings, whereas Holstein considered a single scattering only.

(b) The normal state skin-effect absorptivity R_N was calculated from Dingle's tables of surface resistance, and is the theoretical curve shown in Fig. 18. The superconducting surface resistance was obtained by multiplying R_N by R_S/R_N, which was calculated from theoretical values[56] of σ_1/σ_N and σ_2/σ_N. This was done in three limits, which we will discuss in detail. The resultant values of A_S/A_N are shown in Fig. 21, along with our data (curve A); the data are fit to the expected high-frequency limit $A_S/A_N = 1$.

In curve B, we used the obviously incorrect value $R_S/R_N = 1$, ignoring the effects of the superconducting energy gap on the skin-effect absorptivity. This is useful in showing the structure due to the Holstein effect. The shape of curve B clearly accounts for many of the major features of the data. The computed curve drops smoothly above 35 cm^{-1} as a result of the onset of absorption in the normal state obtained from Eq. (39). It then rises in two steps as a result of the Holstein absorption in the superconducting state. This two step absorption can be seen clearly in the theoretical P_{vS} in Fig. 20, and even in the experimental absolute absorptivity shown in Fig. 18. This arises from the presence of the sharply peaked BCS density of states, which weights

the phonon density of states for Ω near $(\omega-2\Delta)$. Thus the peaks in $\alpha_o^2F(\omega-2\Delta)$ shown in curve E contribute step increases to Eq. (40) and thus to A_S/A_N. The normal density of electronic states is far less selective, and only a small "knee" can be detected in P_{vN}.

Curves C and D represent the attempts to include the superconducting energy gap effects by calculating R_S/R_N in the two limits for which the solution has a closed form. Using the values of $\sigma_S/\sigma_N \equiv \sigma_1(\omega) - i\sigma_2(\omega)$ calculated from strong-coupling superconductivity theory for Pb[56], R_S/R_N is given in the Pippard ($\xi_o \gg \lambda_L$) and London ($\xi_o \ll \lambda_L$) limits by

$$R_S/R_N = \mathrm{Re}(\sigma_1-i\sigma_2)^{-1/3} - \sqrt{3}\ \mathrm{Im}\ (\sigma_1-i\sigma_2)^{-1/3} \qquad \text{(Pippard)} \qquad (43)$$

$$R_S/R_N = \mathrm{Re}(\sigma_1-i\sigma_2)^{-1/2} - \mathrm{Im}\ (\sigma_1-i\sigma_2)^{-1/2} \qquad \text{(London)} \qquad (44)$$

The values of $\sigma_1(\omega)$ and $\sigma_2(\omega)$ are the same for both limits. Both curves C and D underestimate the steepness of the absorption edge above the energy gap. This is not surprising, since even for very pure lead, $\xi_o/\lambda_L \approx 3$, and neither the Pippard nor the London limit is applicable. In addition, the theoretical curves show a fall off above 120 cm^{-1}, resulting from a dispersion in the strong-coupled superconducting gap function.[56] The theoretical feature is similar in shape to, but much smaller than, the experimental decrease. We subsequently found that a more complete evaluation of Eq. (38) for the superconducting case considerably improved the theoretical agreement to the data at high frequencies.

2. Corrections to the Phenomenological Theory

A more detailed treatment of the Golden Rule formalism of the Holstein effect by Allen[57] revealed that our phenomenological theory expressed by Eq. (38) is basically correct, but that our specific expressions for P_{vS} and P_{vN} derived from this require modification.

Firstly, our use of $\alpha_o^2F(\omega)$ assumes that the electron-phonon coupling is isotropic for both modes of acoustic phonons. The transverse phonons couple to electrons mainly by umklapp processes, and the isotropic assumption is not bad. The longitudinal phonons couple by both umklapp and normal processes, and for the latter, the scattering angle is small. As a result, the actual transport electron-phonon coupling is smaller than that assumed previously, i.e. $\alpha_{tr}^2 < \alpha_o^2$. Furthermore, α_{tr}^2/α_o^2 should decrease above the transverse phonon frequency where the longitudinal phonons become important. The function $\alpha_{tr}^2F(\omega)$ estimated by Allen[57] is shown along with $\alpha_o^2F(\omega)$ in Fig. 22.

The second modification involves the inclusion of coherence effects in the calculation of P_{vS}. These effects result from the pairing of electrons in a superconductor, which requires the process of electron scattering in a superconductor to be treated differently from that in a normal metal. For example, in the normal state, the scattering from a state of momentum k and spin σ to the state $k'\sigma'$ is entirely independent of transitions from $-k'-\sigma'$ to $-k-\sigma$, as well as of all other transitions. The probability of both transitions is thus proportional to the sum of the squares of the two matrix elements, that is, $|M_{k\sigma,k'\sigma'}|^2+|M_{-k'-\sigma',\ -k-\sigma}|^2$. In a superconductor, however, the states $k\sigma$ and $-k-\sigma$ are coupled by the pairing interaction, and the two scattering processes described above are

coherent. Thus we must add the matrix elements before scattering, obtaining the result $|M_{k\sigma,\, k'\sigma'} + M_{-k'-\sigma',\, -k-\sigma}|^2$. When the effects of this are taken into account in the calculation of P_{vS}, the result is simply the cancellation of the term involving $K(a)$ in Eq. (40).

These two modifications give the amended expressions for the Holstein absorptivity.

$$P_{vN} \propto (N_o^2/\omega) \int_o^{\omega} (\omega-\Omega)\, \alpha_{tr}^2\, F(\Omega)\, d\Omega \tag{45}$$

$$P_{vS} \propto (N_o^2/\omega) \int_o^{\omega-2\Delta} (\omega-\Omega)\, E(a)\, \alpha_{tr}^2\, F(\Omega)\, d\Omega \tag{46}$$

These were used to calculate A_S/A_N as before, with $\gamma=1$; this is shown in Fig. 23 along with the experimental data. The London limit of R_S/R_N was used, since it gives a steeper onset above the superconducting energy gap.

The inclusion of coherence considerably improves the appearance of the theory at high frequencies, since the decrease in the theoretical A_S/A_N above 100 cm^{-1} is now roughly the same magnitude as that of the experimental A_S/A_N. As is the case with the steps in A_S/A_N due to the Holstein absorption, the fall off in the data above 100 cm^{-1} is broadened and shifted up in frequency. The effects of using $\alpha_{tr}^2 F(\Omega)$ in Eqs. (45) and (46) are less conclusive. From Eq. (46), one would expect the step heights in P_{vS} due to the transverse and longitudinal phonons to be proportional to the area under the respective phonon peaks in $\alpha^2 F$. For $\alpha_o^2 F$, this ratio is 2:1; for Allen's $\alpha_{tr}^2 F$, this is increased to about 3.5:1. The experimental ratio of the two step heights is

approximately 1.8:1, which is considerably closer to that expected from the use of α_o^2F.

The fit of the theoretical and experimental results is sufficient to verify that we have observed the Holstein effect in Pb. Our results indicate that the absolute absorptivity due to real phonon creation is comparable in magnitude to the skin-effect absorptivity. Also, the Holstein absorption in the superconductor shows structure (which is absent in the normal state) which is related to the shape of the phonon density of states. Our Golden Rule calculation of this absorption explains most features of the data; a quantitative explanation requires a rigorous treatment of the phenomenon.

3. Nonlocal Calculation of R_S/R_N

Because the electromagnetic absorption in a metal is proportional to the surface resistance, it is expected that a calculation of R_S/R_N using the nonlocal wave vector-dependent values $\sigma_1(\underset{\sim}{k},\omega)$ should reproduce our results, including the effects due to real phonon creation (Holstein effect), as well as those due to virtual phonon effects, such as the steep absorption edge above 2Δ and the fall off at high frequencies. In contrast, our phenomenological analysis attempted to incorporate the real phonon effects only in P_{vS} and the virtual phonon effects in R_S/R_N, with moderate success.

The computation involved in the nonlocal calculation of R_S/R_N is exceedingly tedious, involving the determination of $\sigma_1(\underset{\sim}{k},\omega)$ and $\sigma_2(\underset{\sim}{k},\omega)$ from strong-coupling superconductivity theory, and an integration over the allowed values of $\underset{\sim}{k}$ for each ω. Shaw and Swihart[45] have calculated R_S/R_N in this manner for several frequencies up to 95 cm^{-1}. Their

results, which are calculated for the cases of diffuse and specular reflection of electrons from the sample surface, are compared to our data in Fig. 24. The curve for specular reflection is in very good quantitative agreement with our data, except in the region from 45-60 cm^{-1}, where it is about 5 per cent smaller than our results. The diffuse scattering theoretical curve underestimates the peak in the experimental A_S/A_N above the energy gap, but agrees well above 50 cm^{-1}. The better fit of the specular reflection theory is somewhat surprising, since it is believed[7] that conduction electrons are diffusely scattered from the surface, except in metals such as bismuth with low carrier densities. Nevertheless, both curves accurately reproduce the steepness of the absorption edge above the energy gap and show the Holstein effect structure at the correct frequencies.

The fit of the nonlocal R_S/R_N calculations is sufficiently accurate to raise the possibility of using the observed A_S/A_N to determine α^2F for a particular sample. Although the computation involved would be extremely tedious, this technique could be of value in studying superconductors such as Nb_3Sn and V_3Si, which are not amenable to investigation by the standard method of superconducting tunneling.

E. Dirty Lead Experiments

We have recently investigated the Holstein effect in samples of Pb alloyed with about 1 per cent by weight of Bi. This was expected to show the effects of changing the electronic mean free path on the Holstein absorption, since the concentration of Bi was small enough to leave the phonon density of states essentially unchanged.

The samples were made by preparing a molten mixture of 99 parts

pure Pb and 1 part Bi, and pouring small pellets about 8mm dia. and 1mm thick onto a clean flat surface. This quenching procedure was necessary to avoid the selective crystallization and inhomogeneous samples which can result from allowing the alloy to cool slowly. The samples were manufactured in a nitrogen atmosphere to avoid oxidation of the surfaces. The front surface was generally quite flat and shiny, with some striations around the edge, probably resulting from the tendency of the molten material to solidify from the center of the face outward. The mounting procedures were the same as those for the pure Pb, although the samples were not chemically polished in any way. The resistivity ratio of the material at 4.2 K was about 30.

Fig. 25 shows our results for A_S/A_N compared with those obtained for pure Pb. Only five spectra on one sample of the alloy are averaged in these preliminary data, so the oscillatory structure above 130 cm^{-1} is probably a cavity resonance. Furthermore, the experiments were not carried out to high enough frequencies to establish the scale factor, and we arbitrarily fit the alloy data to the pure Pb data in the region around 50 cm^{-1}. This could be in error by 5 per cent, but it is sufficient to allow meaningful comparison of the two sets of data.

The magnitude of the structure due to the Holstein effect is smaller in the alloy than in the pure Pb. This is probably a result of the increased magnitude of the skin effect absorptivity rather than a change in the Holstein absorptivity. At the energy gap frequency, $\ell \simeq 3\ \delta_{cl}$ in the alloy ($\delta_{cl} = c/\sqrt{2\pi\omega\sigma}$ is the classical skin depth), so we are just into the anomalous region described by Reuter and Sondheimer.[7] For the pure Pb, $\ell \simeq 5\times10^5\ \delta_{cl}$, and we are in the extreme anomalous limit

for the purposes of calculating the skin effect absorptivity. The skin effect absorptivity calculated from Dingle's tables is about 50 per cent larger for the alloy than for the pure Pb, so the value of $\gamma = P_v/P_s$ is expected to be correspondingly smaller in the alloy, provided the Holstein absorptivity is unchanged. This would account for the observed magnitude of the structure on the A_S/A_N curve.

The lack of any notable change in the shape of the structure on the A_S/A_N data is probably due to the fact that our alloy sample is not dirty enough. The magnitude of the normal state absorptivity is dependent on the ratio ℓ/δ_{cl}. Although the pure metal value is reduced by a factor of 10^5 by the addition of the impurity, the alloy is still in the anomalous $(\ell/\delta_{cl} > 1)$ region. The superconducting absorptivity depends on ξ/λ, the ratio of the coherence length to the penetration depth. In the pure metal with $\ell \gg \xi_o$, $\xi \approx \xi_o \approx 960$ Å,[55] $\lambda \approx \lambda_L \approx 305$ Å,[55] so $\xi/\lambda \approx 3$. In our alloy, $\ell \sim 1500$ Å, which is still larger than ξ_o. If we use the approximation $\xi^{-1} \approx \xi_o^{-1} + \ell^{-1}$, we obtain $\xi \approx 600$ Å. λ increases with decreasing ℓ, but not significantly until $\ell < \xi_o$. For our alloy, we thus estimate $1 < \xi/\lambda < 2$, which is not radically changed from the pure metal value. We should thus not expect to see major changes in the Holstein absorptivity structure until $\ell < \xi_o, \delta_{cl}$.

A smaller ℓ can be obtained by increasing the concentration of Bi in the alloy. However, it appears that Bi is a "poor" impurity because of its similarity to Pb in density and atomic weight. The average distance between Bi atoms in a 1 per cent alloy is approximately 20 Å, whereas the measured mean free path is 1500 Å. This indicates that the Bi atoms are ineffective in scattering electrons through a large

angle. More substantial reductions in ℓ may be obtained by use of an impurity such as In, rather than by increasing the Bi concentration. We are presently investigating both types of alloys.

VI. CONCLUSIONS

We have used the techniques of Fourier Transform spectroscopy in the far-infrared to measure the low-lying electronic energy levels of Ti and V ions in Al_2O_3 and the electromagnetic absorption in Pb. We constructed a Michelson interferometer and several low temperature doped Ge bolometers for use in the far-infrared. A noise analysis of the bolometer-amplifier circuit indicated that the NEP was severely limited by the amplifier noise, and could be reduced by increasing the detector responsivity. This could be achieved by use of He^3 cryogenics to reduce the detector temperature by a factor of three.

Our transmission measurements on Ti and V-doped Al_2O_3 confirmed the assignment of perviously observed zero-field absorption lines to the electronic levels of the d^1 ions Ti^{3+} and V^{4+} in the Al_2O_3 crystalline field. We investigated the Zeeman splitting of these levels and found good agreement with a theoretical prediction of the energy levels of a single d electron in the Al_2O_3 crystalline field modified by a dynamic Jahn-Teller effect. An additional absorption line attributed to the d^2 ion V^{3+} exhibited a Zeeman splitting which was in excellent agreement with the theoretical magnetic field dependence obtained from a spin Hamiltonian.

We used a calorimetric method to measure the far-infrared absorption in single crystals of pure Pb in the normal and superconducting states. Our results show the first example of structure on the absorptivity of a metal due to the excitation of phonons. The absorption spectrum for the normal metal increases dramatically near the transverse

phonon frequency $\omega_t \approx 35\ cm^{-1}$; a sharper absorption onset is observed at $\omega_t + 2\Delta \approx 55\ cm^{-1}$ in the superconducting state. In addition, the spectrum for the superconductor shows structure which can be correlated with the transverse and longitudinal peaks in the phonon density of states. We have thus observed the onset of the volume phonon generation process proposed by Holstein.

Most of the features of our data can be explained by a "Golden Rule" calculation of the absorptivity expected from the Holstein process. Recent calculations by Swihart of the non local surface resistance of Pb below 100 cm^{-1} are in very good agreement with our data. This indicates that strong-coupling superconductivity theory can explain features in the surface impedance due to real phonons (the Holstein absorption) as well as virtual phonons (the steep absorption edge above the energy gap). This represents a possible method for obtaining information on the phonon density of states in materials which cannot be easily investigated by the standard method of superconducting tunneling.

ACKNOWLEDGEMENTS

I would like to express my deep gratitude to Professor P. L. Richards for suggesting the research topics and providing guidance and encouragement throughout the course of my research. Thanks are also due Dr. J. Y. Wong and Dr. J. F. Moser for providing the doped Al_2O_3 crystals used in our experiments. My understanding of the Holstein process has benefited greatly from many discussions with Professor L. M. Falicov and Dr. P. B. Allen. I would also like to thank Professor J. C. Swihart and Dr. H. Scher for sending me prepublication results of their calculations of the Holstein effect in lead.

In addition, I would like to acknowledge the valuable assistance of Mr. L. Blake during the tedious hours of data acquisition and analysis.

Finally, I want to thank Miss Kathy Williams for her skill in transforming my barely legible handwriting into the typed manuscript.

This work was supported in part by the United States Atomic Energy Commission.

APPENDIX

A. A Fast Fourier Transform Program for the IBM 1620

This Appendix contains a description and printout of FCOOL, a fast Fourier Transform program written for the IBM 1620 computer. The local availability of this facility allowed us to rapidly obtain the frequency spectrum of one experimental run before proceeding to the next one. A previously existing program, which calculated the spectrum point-by-point using Eq. (9), was limited to an interferogram length of 300 points and an output length of 200 points; calculation of this spectrum required 720 seconds of computing time. The program described here is capable of calculating a 256 point spectrum from a 512 point interferogram in 40 seconds.

The fast Fourier Transform program is based on an algorithm[16] invented by Cooley and Tukey. Connes[18] gives an excellent descritpion of the steps involved in the computation of the spectrum by this technique.

The core storage limitations of the IBM 1620 required the program to be broken up into three subprograms, COOLA, COOLB, and COOLC. The main program FCOOL calls each of these subprograms in sequence, and the auxiliary disk is used to store the data during the intermediate stages of computation.

Subroutine COOLA reads in the data, ten points to a card, and computes the interferogram. Although the Cooley-Tukey algorithm requires the number of input points to be an integral power of two, interferograms of arbitrary length can be read in, and COOLA extends the data to the next highest power of two with zeros. The computation of the frequency spectrum occurs in subroutine COOLB. The spectrum is

plotted out as a histogram by COOLC.

The Cooley-Tukey algorithm calculates the complex Fourier Transform, and thus requires an N point complex interferogram consisting of N/2 real and N/2 imaginary points. The output consists of N/2 sine transform points and N/2 cosine transform points. For the real, symmetric interferogram obtained in our experiments, N/2 of the input points would consist of zeros, and the sine and cosine transforms obtained are, respectively, antisymmetric and symmetric about the N/4th output point. The maximum value N=512 imposed by the memory of the IBM 1620 allows a maximum interferogram length of 256 points and computes a maximum of 128 spectral points when only the Cooley-Tukey algorithm is used. However, the subroutine COOLB utilizes the symmetry of the sine and cosine transforms of the real interferogram to allow the interferogram and spectrum lengths to be doubled. The first half of COOLB calculates the N/4 significant sine and cosine transform points of an N-point real interferogram. These are then reordered in the second half of COOLB to obtain an N/2 point cosine transform. A description of this method is given by Connes.[18]

```
C     PROGRAM FCOOL
C
C     THIS PROGRAM CALCULATES THE FOURIER TRANSFORM OF A REAL INTER-
C     FEROGRAM USING THE COOLEY-TUKEY FAST FOURIER TRANSFORM ALGORITHM.
C     THIS PROGRAM UTILIZES THE SYMMETRY OF THE COSINE AND SINE TRANSFORMS
C     OF THE REAL INTERFEROGRAM, AND CALCULATES ONLY THE COSINE FOURIER
C     TRANSFORM OF THE INPUT DATA.  MAXIMUM NUMBER OF OUTPUT POINTS IS
C     ONE-HALF THE NUMBER OF INPUT POINTS.  INPUT DATA FORMAT IS AS FOLLOWS
C
C     MIN-MAX CARD...NUMBER OF FIRST AND LAST OUTPUT POINTS. FORMAT(2I4)
C     TITLE CARD...DELTA IN MM, FORMAT(F5.3).  COMMENTS
C     DATA, TEN POINTS PER CARD, FORMAT(10F7.2)
C
C     IF NUMBER OF INPUT POINTS IS NOT A POWER OF TWO, THE DATA ARE
C     EXTENDED TO THE NEXT POWER OF TWO WITH ZEROS.  ARE SQUARED JAY
C     MARCH 1970 TARG
C
      DEFINE DISK(10, 900)
      FIND(1)
      SAM = COSF(1.)
   10 CALL COOLA
      CALL COOLB
      CALL COOLC
C
C     SENSE SWITCH 1 ON FOR MULTIPLE SETS OF DATA
C
      IF (SENSE SWITCH 1) 10, 20
   20 CONTINUE
      CALL EXIT
      END
C
C
C
C
      SUBROUTINE COOLA
C
C     SUBROUTINE COOLA READS IN DATA, AVERAGES LAST TEN POINTS TO
C     OBTAIN I(INFINITY), AND CALCULATES THE INTERFEROGRAM F(DELTA) =
C     4.*DELTA*(I(DELTA) - I(INFINITY)).
C
      DIMENSION COMM(19), DATUM(10), DATA(520)
      NUMBER = 0
      AVE = 0
      READ 1, MIN, MAX
      READ 2, DELTA, COMM
      PRINT 4, COMM
      PRINT 5
   10 READ 3, DATUM
      PRINT 6, DATUM
      DO 30 I = 1, 10
      IF (DATUM(I)) 50, 50, 20
   20 NUMBER = NUMBER + 1
   30 DATA(NUMBER) = DATUM(I)
      GO TO 10
   50 J = NUMBER - 9
      DO 60 I = J, NUMBER
   60 AVE = AVE + DATA(I)
      AVE = .1*AVE
      J = 0
      DO 80 I = 1, NUMBER
```

```
      DATA(I) = 4.*DELTA*(DATA(I) - AVE)
   80 CONTINUE
      N = 1
   81 M1 = 2**N
      IF(NUMBER - M1) 82, 82, 83
   83 N = N + 1
      GO TO 81
   82 MUMBER = NUMBER + 1
      DO 90 I = MUMBER,M1
   90 DATA(I) = 0.0
C
C     JO = 2**N = NUMBER OF INPUT POINTS ROUNDED OFF TO NEXT HIGHEST
C     POWER OF TWO.
C
      JO = 2**N
      LUCY = JO/2 + 1
      DATA(1) = DATA(1) *.5
      INDISK = 1
      RECORD (INDISK) N, MIN, MAX, JO, LUCY, DELTA
      RECORD (INDISK) COMM
      L = 0
      DO 100 I = 1, M1
      L = L + 1
      DATUM(L) = DATA(I)
      IF (10-L) 100, 101, 100
  101 RECORD (INDISK) DATUM
      L = 0
  100 CONTINUE
      L = L + 1
      DO 102 I = L, 10
  102 DATUM(I) = 0.0
      RECORD (INDISK) DATUM
      PRINT 308
    1 FORMAT (2I4)
    2 FORMAT (1F5.3, 18A4, 1A3)
    3 FORMAT (10F7.2)
    4 FORMAT (1H1, 16X, 19A4)
    5 FORMAT (14H0INPUT DATA IS)
    6 FORMAT (1H , 16X, 10F10.1)
  308 FORMAT (15H0OUTPUT DATA IS)
      RETURN
      END
C
C
C
C
      SUBROUTINE COOLB
C
C     SUBROUTINE COOLB CALCULATES THE COSINE FOURIER TRANSFORM USING
C     THE COOLEY-TUKEY ALGORITHM IN A PROGRAM OBTAINED FROM MERTZ.
C     INTEGRATION WITH FIRST POINT ONE-HALF OF ITS INPUT VALUE
C
      DIMENSION OUT(10), DATA(520)
      INDISK = 1
      FETCH (INDISK) N, MIN, MAX, JO, LUCY
      INDISK = 4
      FIND (INDISK)
      J = 0
  310 FETCH (INDISK) OUT
```

```
      DO 320 I = 1, 10
      J = J + 1
      IF (J - JO) 311, 311, 312
  311 DATA(J) = OUT(I)
  320 CONTINUE
      GO TO 310
  312 INDISK = 4
      FIND (INDISK)
C
C     THE FOLLOWING COMPUTES A JO/2 ORDER FOURIER TRANSFORM, OBTAINING
C     JO/4 COSINE AND JO/4 SINE OUTPUT POINTS.
C
      J = 1
      DO 105 I = 1, JO, 2
      IF (I-J) 101, 102, 102
  101 TEMPR = DATA(J)
      TEMPI = DATA(J+1)
      DATA(J) = DATA(I)
      DATA(J+1) = DATA(I+1)
      DATA(I) = TEMPR
      DATA(I+1) = TEMPI
  102 M = JO/2
  103 IF (J-M) 105, 105, 104
  104 J = J-M
      M = M/2
      IF (M-2) 105, 103, 103
  105 J = J + M
      MMAX = 2
  106 IF (MMAX - JO) 107,110,110
  107 ISTEP = 2 * MMAX
      AMAX = MMAX
      THETA = 6.28318531/AMAX
      SINTH = SINF(THETA/2.)
      WSTPR = -2.*SINTH*SINTH
      WSTPI = SINF(THETA)
      WR = 1.
      WI = 0.
      DO 109 M = 1, MMAX, 2
      DO 108 I = M, JO, ISTEP
      J = I + MMAX
      TEMPR = WR*DATA(J) - WI*DATA(J+1)
      TEMPI = WR*DATA(J+1) + WI*DATA(J)
      DATA(J) = DATA(I) - TEMPR
      DATA(J+1) = DATA(I+1) - TEMPI
      DATA(I) = DATA(I) + TEMPR
  108 DATA(I+1) = DATA(I+1) + TEMPI
      TEMPR = WR
      WR = WR*WSTPR - WI*WSTPI + WR
  109 WI = WI*WSTPR + TEMPR*WSTPI + WI
      MMAX = ISTEP
      GO TO 106
C
C     THE JO/4 COSINE AND JO/4 SINE TRANSFORMS ARE REORDERED TO OBTAIN
C     A JO/2 ORDER COSINE FOURIER TRANSFORM OF THE JO INPUT POINTS.
C
  110 DATA(1) = DATA(1) + DATA(2)
      DO 150 I = 3, LUCY, 2
      J = JO + 2 - I
      TEMPI = I - 1
      TEMPR = JO
```

```
      WR = DATA(I) + DATA(J)
      WI = (DATA(I+1) + DATA(J+1))*COSF(3.1415926535*TEMPI/TEMPR) +
     1(DATA(I) - DATA(J))*SINF(3.1415926535*TEMPI/TEMPR)
      DATA(I) = (WR + WI)*.5
  150 DATA(J) = (WR - WI)*.5
      L = 0
      J = MAX - MIN + 1
      DO 330 I = 1, J
      L = L + 1
      M = 2*MIN - 3 + 2*I
      OUT(L) = DATA(M)
      IF (10-L) 330, 340, 330
  340 RECORD (INDISK) OUT
      PRINT 309, OUT
      L = 0
  330 CONTINUE
      L = L + 1
      DO 350 I = L, 10
  350 OUT(I) = 0.0
      PRINT 309, OUT
      RECORD (INDISK) OUT
  309 FORMAT (1H , 16X, 10F10.1)
      RETURN
      END
C
C
C
C
      SUBROUTINE COOLC
C
C     SUBROUTINE COOLC PLOTS OUT THE SPECTRUM FROM MIN TO MAX.  THE
C     VERTICAL SCALE CONTAINS 100 RESOLUTION WIDTHS.
C
      DIMENSION DATA(256), COMM(19), LIST(50), DATUM(10)
      SMIN = 0.0
      SMAX = 0.0
      INDISK = 1
      FIND (INDISK)
      DO 10 I = 1, 50
   10 LIST(I) = 0
      FETCH(INDISK) N, MIN, MAX, JO, LUCY, DELTA
      DEN = 2**N - 1
      NUMBER = MAX - MIN + 1
      DEN = 5./(DEN * DELTA)
      FREQ = MIN - 1
      FREQ = 2.*FREQ*DEN
      NN = 1
      FETCH (INDISK) COMM
      PRINT 2, COMM
      INDISK = 4
      FIND (INDISK)
   20 FETCH (INDISK) DATUM
      DO 80 I = 1, 10
      IF (NN - NUMBER) 30, 30, 90
   30 IF (DATUM(I) - SMIN) 40, 40, 50
   40 SMIN = DATUM(I)
   50 IF (DATUM(I) - SMAX) 70, 60, 60
   60 SMAX = DATUM(I)
   70 DATA(NN) = DATUM(I)
```

```
 80 NN = NN + 1
    GO TO 20
 90 S1 = 99./(SMAX - SMIN)
    S2 = 1. - S1*SMIN
    NN = S2
    M1 = (NN + 1)/2
    M2 = NN + 2 - 2*M1
    M2 = (2 - M2) * 2
    M2 = 70*10**M2
    DO 130 I = 1, NUMBER
    NN = S1*DATA(I) + S2
    N1 = (NN + 1)/2
    N2 = NN + 2 - N1*2
    DO 95 NN = 1, N1
 95 LIST (NN) = 6767
    LIST (M1) = M2
    GO TO (100, 110) , N2
100 LIST (N1) = 6700
    GO TO 120
110 LIST (N1) = 6767
120 PRINT 1, FREQ, DATA(I), LIST
    FREQ = FREQ + 2.*DEN
    DO 130 NN = 1, N1
130 LIST (NN) = 0
  1 FORMAT (1H , 1F7.2, 1F9.1, 3X, 50A2)
  2 FORMAT ( 1H1, 2X, 23HUNAPODIZED SPECTRUM FOR, 2X, 19A4,///)
    RETURN
    END
```

REFERENCES

1. Carl J. Ballhausen, Introduction to Ligand Field Theory (McGraw-Hill Co., Inc., New York, 1964); M. Tinkham, Group Theory and Quantum Mechanics (McGraw-Hill Book Co., Inc., New York, 1962).

2. A. Abragam and M. H. L. Pryce, Proc. Roy. Soc. A205, 135 (1951).

3. R. M. MacFarlane, J. Y. Wong, and M. D. Sturge, Phys. Rev. 166, 250 (1968).

4. J. Bardeen, L. N. Cooper, and J. R. Schrieffer, Phys. Rev. 108, 1175 (1957).

5. D. M. Ginsberg and L. C. Hebel, in Superconductivity, edited by R. D. Parks (Marcel Dekker, New York, 1969), Vol. 1, Chap. 4; M. Tinkham, in Optical Properties and Electronic Structure of Metals and Alloys, edited by F. Abeles (North-Holland Publishing Co., Amsterdam, 1966), pp. 431-451.

6. T. Holstein, Phys. Rev. 96, 535 (1954).

7. A. B. Pippard, Metallic Conduction at High Frequencies and Low Temperatures, in Advances in Electronics and Electron Physics (Academic Press, New York, 1954), Vol. 6, p. 1.

8. C. K. N. Patel, in Lasers, edited by A. K. Levine (Marcel Dekker, New York, 1968), Vol. 2, Chap. 1.

9. D. W. Faries, K. A. Gehring, P. L. Richards, and Y. R. Shen, Phys. Rev. 180, 363 (1969).

10. N. Van Tran and C. K. N. Patel, Phys. Rev. Letters 22, 463 (1969).

11. J. Connes, Rev. Opt. 40, 45 (1961); 40, 116 (1961); 40, 171 (1961); 40, 231 (1961).

12. P. L. Richards, in Spectroscopic Techniques for Far Infra-Red, Submillimetre, and Millimetre Waves, edited by D. H. Martin (North-

Holland Publishing Co., Amsterdam, 1967), Chap. 2.

13. P. Fellgett, J. Physique 19, 187 (1958).

14. Y. Yamada, A. Mitsuishi, and H. Yoshinaga, J. Opt. Soc. Am. 52, 17 (1962).

15. K. D. Möller and R. V. McKnight, J. Opt. Soc. Am. 55, 1075 (1965).

16. J. W. Cooley and J. W. Tukey, Math. of Computation 19, 297 (1965).

17. H. Sakai and G. A. Vanasse, Fourier Spectroscopy, in Progress in Optics (North-Holland Publishing Co., Amsterdam, 1967), Vol. 6, pp. 261-330.

18. J. Connes, Computing Problems in Fourier Spectroscopy, in Proceedings of the 1970 International Conference on Fourier Spectroscopy, held in Aspen, March 1970 (To be issued as AFCRL Report).

19. F. J. Low, J. Opt. Soc. Am. 51, 1300 (1961).

20. E. H. Putley and D. H. Martin, in Spectroscopic Techniques for Far Infra-Red, Submillimetre, and Millimetre Waves, edited by D. H. Martin (North-Holland Publishing Co., Amsterdam, 1967), Chap. 4; R. A. Smith, F. E. Jones, and R. P. Chasmar, The Detection and Measurement of Infra-Red Radiation (Oxford University Press, London, 1968), Chaps. 3 and 4.

21. R. C. Jones, J. Opt. Soc. Am. 43, 1 (1953).

22. R. A. Smith, F. E. Jones, and R. P. Chasmar, The Detection and Measurement of Infra-Red Radiation (Oxford University Press, London, 1968), Chap. 5.

23. H. D. Drew and A. J. Sievers, Appl. Optics 8, 2067 (1969).

24. P. L. Richards, Pure and Applied Chemistry 11, 535 (1965).

25. F. J. Low, Proc. IEEE 54, 477 (1966).

26. E. D. Nelson, J. Y. Wong, and A. L. Schawlow, Phys. Rev. 156, 298 (1967).

27. J. Y. Wong, M. J. Berggren, and A. L. Schawlow, J. Chem. Phys. 49, 835 (1968).

28. A. Hadni, Phys. Rev. 136, A758 (1964).

29. C. H. Perry, R. Geick, and E. F. Young, Appl. Opt. 5, 1171 (1966).

30. J.-F. Moser, W. Zingg, H. Steffen, and F. Kneubühl, Phys. Letters 24A, 411 (1967); J.-F. Moser, H. Steffen, and F. Kneubühl, Phys. Kondensierten Materie 7, 261 (1968).

31. G. C. Brackett, Ph.D. thesis, University of California, Berkeley, 1970 (unpublished).

32. G. A. Slack (General Electric Research and Development Laboratory, Schenectady, New York), private communication, September 1968.

33. D. S. McClure, J. Chem. Phys. 36, 2757 (1962).

34. N. E. Kask, L. S. Kornienko, T. S. Mandel'shtam, and A. M. Prokhorov, Fiz. Tverd. Tela 5, 2306 (1963) [English translation: Soviet Phys. - Solid State 5, 1677 (1964)].

35. D. W. Feldman, D. C. Burnham, and J. G. Castle, Jr., in Quarterly Scientific Report, Westinghouse Research Lab., Report No. 4, 1964.

36. F. R. Merritt, private communication, December 1967.

37. F. S. Ham, Phys. Rev. 138, A1727 (1965).

38. Z. Goldschmidt, W. Low, and M. Foguel, Phys. Letters 19, 17 (1965).

39. E. A. Vinogradov, N. A. Irisova, T. S. Mandel'shtam, A. M. Prokhorov, and T. A. Shmanov, Pis'ma v Redaktsiyu 4, 373 (1966) [English transl., Soviet Phys. - JETP Letters 4, 252 (1966)].

40. G. M. Zverev and A. M. Prokhorov, Zh. Eksperim. i Teor. Fiz. 40, 1016 (1961) [English transl., Soviet Phys. - JETP 13, 714 (1961)].

41. M. Sauzade, J. Pontnau, P. Lesas, and D. Silhouette, Phys. Letters

19, 617 (1966).

42. A. R. Smith and R. W. Mires, Phys. Rev. 172, 265 (1968).

43. M. A. Biondi, Phys. Rev. 96, 534 (1954).

44. H. Scher (Bell Telephone Laboratories, Murray Hill, New Jersey), private communication, April 1970; Bull. Am. Phys. Soc. 12, 672 (1967).

45. W. Shaw and J. C. Swihart (Indiana University, Bloomington, Indiana), private communication, April 1970.

46. M. A. Biondi, M. P. Garfunkel, and W. A. Thompson, Phys. Rev. 136, A1471 (1964).

47. H. D. Drew and A. J. Sievers, Phys. Rev. Letters 19, 697 (1967).

48. R. B. Dingle, Physica 19, 311 (1953).

49. R. G. Chambers, Proc. Roy. Soc. (London), Ser. A215, 481 (1952).

50. P. L. Richards, Phys. Rev. Letters 7, 412 (1961).

51. T. Holstein, Ann. Phys. (N.Y.) 29, 410 (1964).

52. This approach was suggested by L. M. Falicov (University of California, Berkeley, California), private communication, October 1969.

53. W. L. McMillan and J. M. Rowell, in Superconductivity, edited by R. D. Parks (Marcel Dekker, New York, 1969), Vol. 1, Chap. 11.

54. M. A. Biondi, Phys. Rev. 102, 964 (1956).

55. R. F. Gasparovic and W. L. McLean, Phys. Rev. (to be published).

56. W. Shaw and J. C. Swihart, Phys. Rev. Letters 20, 1000 (1968); also (to be published).

57. P. B. Allen (Bell Telephone Laboratories, Murray Hill, New Jersey), private communication, May 1970.

Table I. Ge Bolometer Data

$S = 6\times10^{4}$ v/W	$S_m = 7\times10^{4}$ v/W	$\Delta = 8$ K
$NEP = 9\times10^{-13}$ W/Hz$^{1/2}$		$T_s = 1.08$ K
$G = 5\times10^{-5}$ W/K		$T_o = 1.30$ K
$R_o = 5.5\times10^{5}$ Ω		$\tau \approx 4$ msec
$R_L = 9\times10^{6}$ Ω		$\nu = 42$ Hz
$I_{op} = 4.6$ μa	$I_m = 2.6$ μa	$B = 1$ Hz
$e_s = 5.5\times10^{-8}$ v/Hz$^{1/2}$		Vol = 11 mm^3

Table II. Calculated and experimental values (in units of cm^{-1}) of the zero-field energy splittings δ_1 and δ_2 and the g-factors for the low lying energy levels of the d^1 ions Ti^{3+} and V^{4+} in Al_2O_3. Comparison with experiment is made for several values of the crystalline field parameters v and ζ and the Jahn-Teller energy E_{JT}.

Sample	v	ζ	E_{JT}	δ_1	δ_2	$g_{0\parallel}$	$g_{0\perp}$	$g_{1\parallel}$	$g_{1\perp}$	$g_{2\parallel}$
	700	120	200	44.98	104.21	1.16	0.0	-2.22	< 0.2	1.88
$Al_2O_3:Ti^{3+}$	680	90	187	37.96	106.53	1.13	0.0	-2.30	< 0.2	1.93
		Experimental		37.8	107	1.11	<0.1	-2.00	< 0.1	
	970	195	320	27.93	53.15	1.59	0.0	-2.00	< 0.5	1.86
$Al_2O_3:V^{4+}$	750	290	333	27.80	53.20	1.60	0.0	-1.70	< 0.5	1.66
		Experimental		28.1	53	1.43	<0.2	-1.43	< 0.2	

FIGURE CAPTIONS

Fig. 1. Far-infrared Michelson interferometer used in the frequency range 2-350 cm^{-1}.

Fig. 2. Block diagram of the experimental apparatus, including cryostat for low-temperature transmission measurements.

Fig. 3. (a) Power spectrum of the measured signal after wide-band amplification. The coherent signal is represented by the spike at ω_o; the noise consists of a "white" detector background and a contribution $\propto \omega^{-1}$ due to the amplifier.

(b) Power spectrum after narrow band amplification in a region $\Delta\omega_1$ centered at ω_o.

(c) Power spectrum of a square wave of frequency ω_o symmetric about zero voltage.

(d) Power spectrum of the measured signal after phase detection; this is the convolution of Fig. 3b and Fig. 3c.

(e) Power spectrum after a low pass filter of time constant τ=RC. The noise power bandwidth is reduced from $\Delta\omega_1$ to $1/\tau$.

Fig. 4. (a) Power spectrum of the signal after digital integration for a time T_1.

(b) The periodic sampling function used in our data acquisition and its power spectrum.

(c) Power spectrum resulting from periodic sampling of the signal. The noise power in the shaded area will appear in the frequency region 0 - $(2T_1)^{-1}$ as a result of convolution with the sampling power spectrum in Fig. 4b.

(d) Frequency spectrum obtained by oversampling of the interferogram. High frequency noise on interferogram appears as spectral noise in the region $\nu_c - \nu_{max}$.

Fig. 5. Upper: Bolometer mounting geometry used in transmission experiments.

Lower: Schematic of bolometer circuit. C= heat capacity of bolometer and electrical leads. G= thermal conductance of leads. T_s= temperature of heat sink. $P_o + P_1 e^{i\omega t}$= power incident on bolometer. T= bolometer temperature. R= bolometer resistance. V= bias source. R_L= bias current-regulating load resistor.

Fig. 6. (a) Schematic of bolometer-amplifier circuit. V= bias source. R_L= load resistor. R_o= bolometer resistance. R_I= input resistance of amplifier.

(b) Equivalent circuit of Fig. 6a for purposes of noise analysis. e_L= voltage noise in load resistor R_L. e_o= voltage noise in bolometer R_o. E= signal. e_I= voltage noise in input resistor R_I. i_g= grid current noise in amplifier. e_A= input noise of amplifier with terminals shorted.

Fig. 7. Load curve (solid curve), and theoretical dc responsivity (dashed curve) of a Ge bolometer.

Fig. 8. Current dependence of theoretical dc responsivity (circles) and theoretical ac responsivity (squares) at 42 Hz obtained from the load curve shown in Fig. 7. The solid curve is the experimental responsivity at 42 Hz for the same bolometer fitted to the theoretical ac curve above 10 μa.

Fig. 9. Experimental (points) and theoretical (solid lines) current

dependence of the NEP for the bolometer whose load curve is plotted in Fig. 7. The upper and lower curves represent the NEP for load resistor temperatures of 300 K (our experimental condition) and 4 K, respectively, obtained from Eq. (23).

Fig. 10. Cryostat containing superconducting solenoid for transmission measurements in a magnetic field.

Fig. 11. Low-lying electronic energy levels of $Al_2O_3:d^1$.

Fig. 12. Zeeman splitting of the 37.8 cm^{-1} line in $Al_2O_3:Ti^{3+}$ in a magnetic field oriented parallel to the optic axis. The points are averages of several measurements of the transmission minima.

Fig. 13. Zeeman splitting of the 28.1 cm^{-1} line in $Al_2O_3:V^{4+}$ in a magnetic field oriented parallel to the optic axis.

Fig. 14. Energy level diagram for $Al_2O_3:d^1$ illustrating the inclusion of the dynamic Jahn-Teller effect. The right side shows the decomposition of the free ion ^2D level in the static crystalline field (Fig. 11). The left side shows the degenerate vibronic levels of a vibrational mode of energy $\hbar\omega$ in the cubic field. The inclusion of the crystalline field and the vibrational mode yields the "intermediate" energy splittings δ_1 and δ_2.

Fig. 15. Low-lying electronic energy levels of $Al_2O_3:d^2$.

Fig. 16. Zeeman splitting of the 8.25 cm^{-1} line in $Al_2O_3:V^{3+}$. The circles and squares represent experimental values for the magnetic field oriented, respectively, parallel to and perpendicular to the optic axis. Except where indicated by flags, the linewidth at one-half the peak absorption coefficient is ~ 0.3 cm^{-1}.

Fig. 17. Sample mounting geometry employed in the direct absorption

experiments on lead.

Fig. 18. Measured frequency-dependent absorptivity in superconducting (circles) and normal (squares) lead compared with the prediction of normal state anomalous skin effect theory. The limits of the error bars are plus and minus one standard deviation (75 per cent confidence).

Fig. 19. Measured ratio of the absorptivity in superconducting and normal lead normalized to the high frequency limit $A_S/A_N=1$. The limits of the error bars are plus and minus one standard deviation.

Fig. 20. The Holstein absorptivities P_N and P_S for normal and superconducting lead, respectively, obtained from Eqs. (39) and (40).

Fig. 21. Measured ratio (curve A) of the absorptivity in superconducting and normal lead compared with (curve B) a theoretical estimate of A_S/A_N which ignores the effect of the energy gap on the superconducting anomalous skin effect absorption, and estimates of A_S/A_N with the surface absorption taken from the extreme anomalous limit (curve C) and the local limit (curve D) of strong-coupling superconductivity theory. Curve E is $\alpha_o^2\ (\nu-2\Delta)\ F(\nu-2\Delta)$, the square of the electron-phonon coupling constant times the phonon density of states shifted in frequency by 2Δ. Curves A, B, C, and D are plotted on the same scale, but B has been shifted vertically for clarity.

Fig. 22. $\alpha_o^2\ F(\nu)$ for lead (solid curve) obtained by Rowell and McMillan, compared with Allen's estimate of $\alpha_{tr}^2 F(\nu)$ (dashed curve).

Fig. 23. Measured A_S/A_N for lead (points) compared with a theoretical estimate (solid curve) obtained from Eqs. (45) and (46), including

α^2_{tr} $F(\omega)$ and the effects of superconducting coherence.

Fig. 24. Measured A_S/A_N for lead (curve A) compared with Swihart's nonlocal calculations for R_S/R_N for diffuse (curve B) and specular (curve) reflection of conduction electrons from the surface.

Fig. 25. Measured A_S/A_N for pure lead (circles) compared with the measured A_S/A_N for an alloy of 1 per cent bismuth in lead. The data for the alloy are fitted to those for the pure lead in the region around 50 cm^{-1}; the scale factor established by this fit may be in error by 5 per cent.

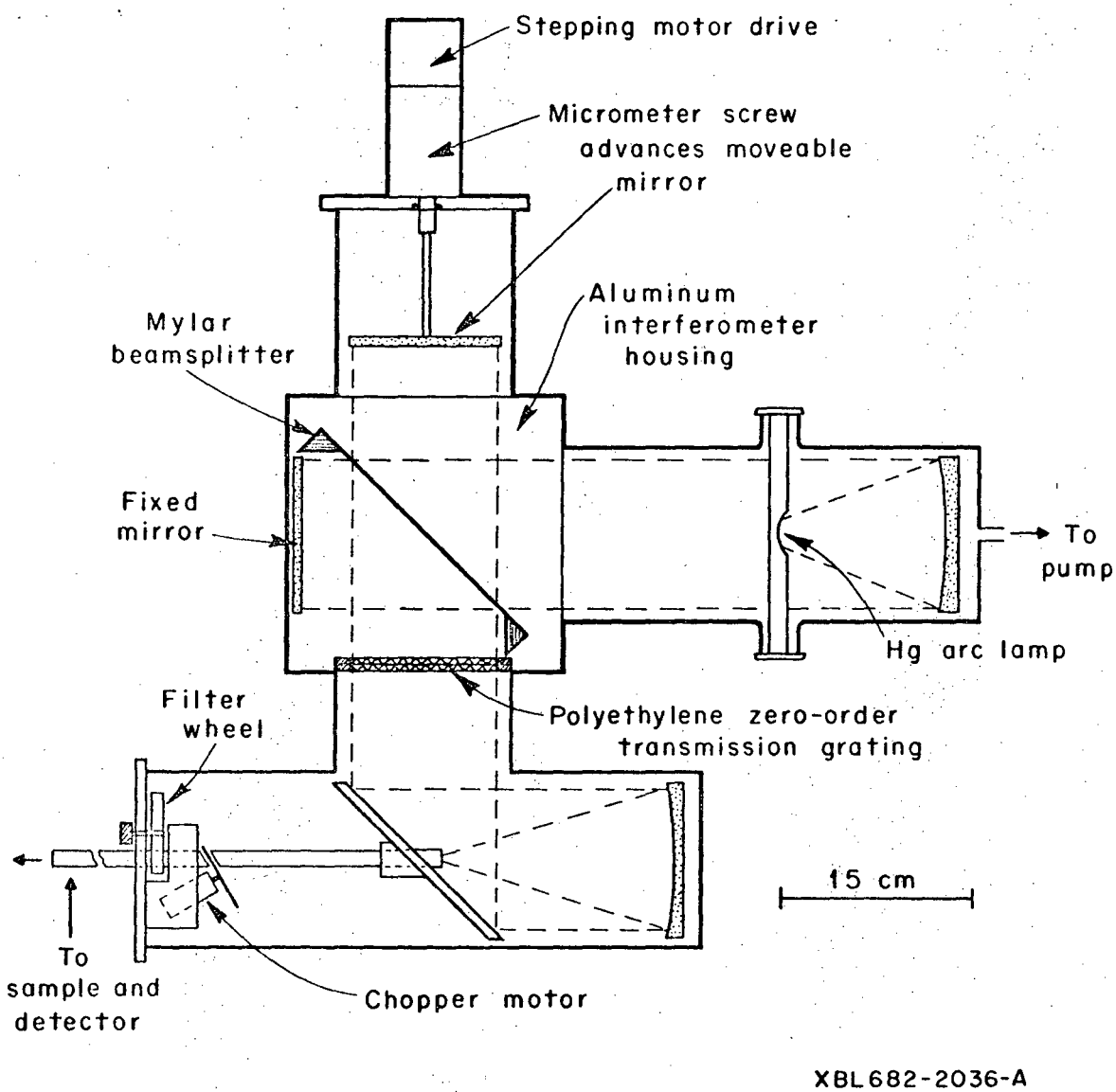
Stepping motor drive
Micrometer screw advances moveable mirror
Aluminum interferometer housing
Mylar beamsplitter
Fixed mirror
To pump
Hg arc lamp
Filter wheel
Polyethylene zero-order transmission grating
15 cm
To sample and detector
Chopper motor
XBL682-2036-A

Fig. 1

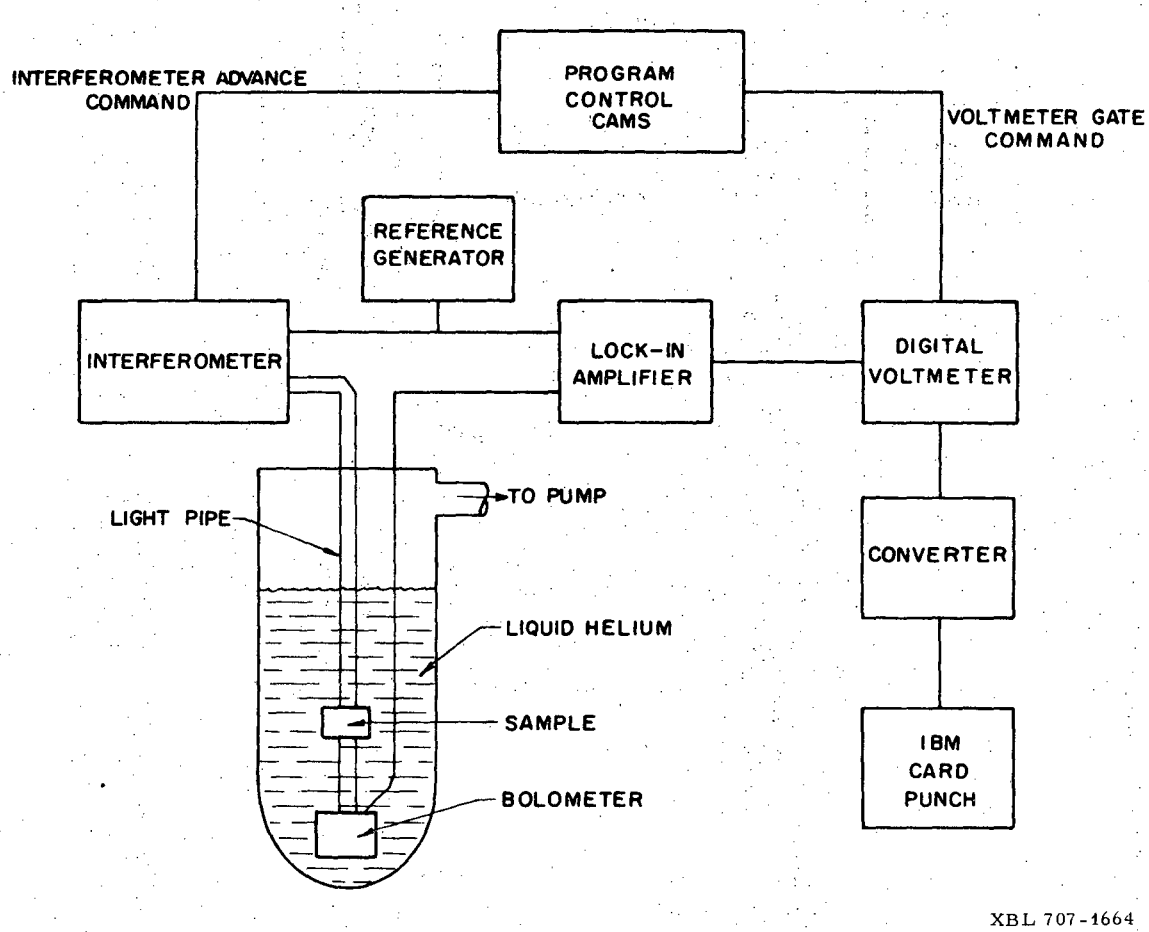
INTERFEROMETER ADVANCE COMMAND
PROGRAM CONTROL CAMS
VOLTMETER GATE COMMAND
REFERENCE GENERATOR
INTERFEROMETER
LOCK-IN AMPLIFIER
DIGITAL VOLTMETER
TO PUMP
LIGHT PIPE
CONVERTER
LIQUID HELIUM
SAMPLE
IBM CARD PUNCH
BOLOMETER
XBL 707-1664

Fig. 2

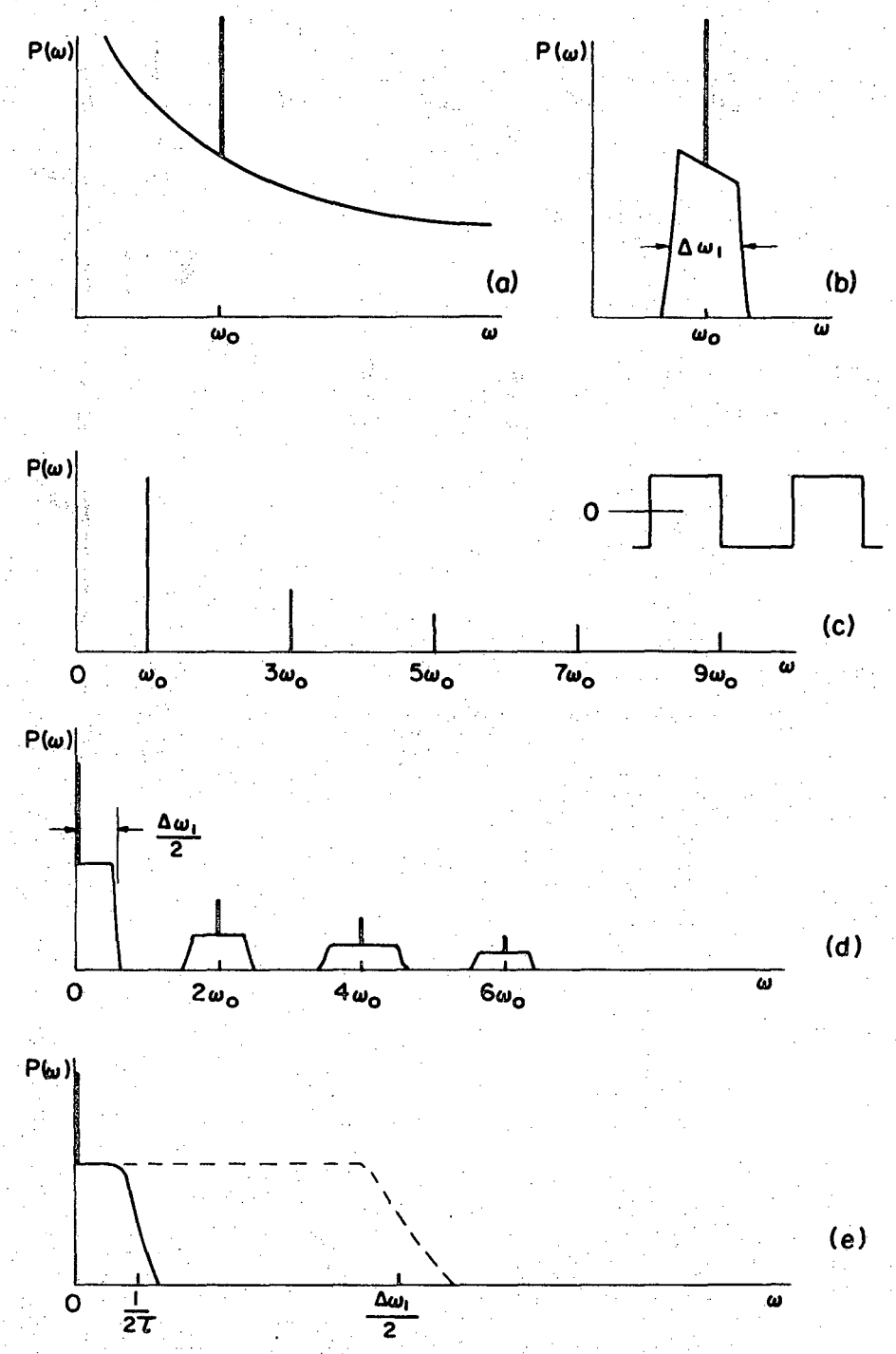

XBL 707-1663

Fig. 3

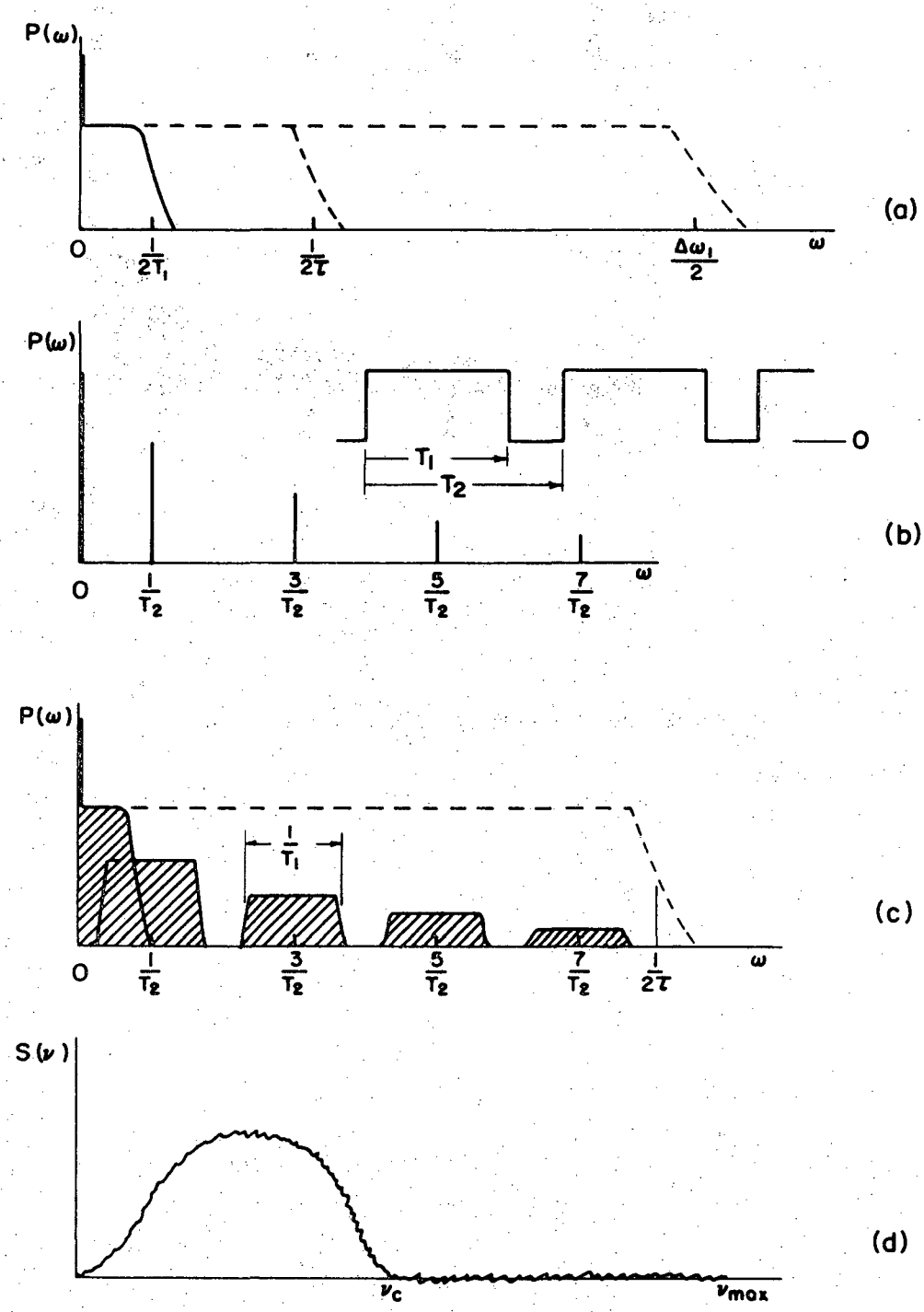

XBL 707-1662

Fig. 4

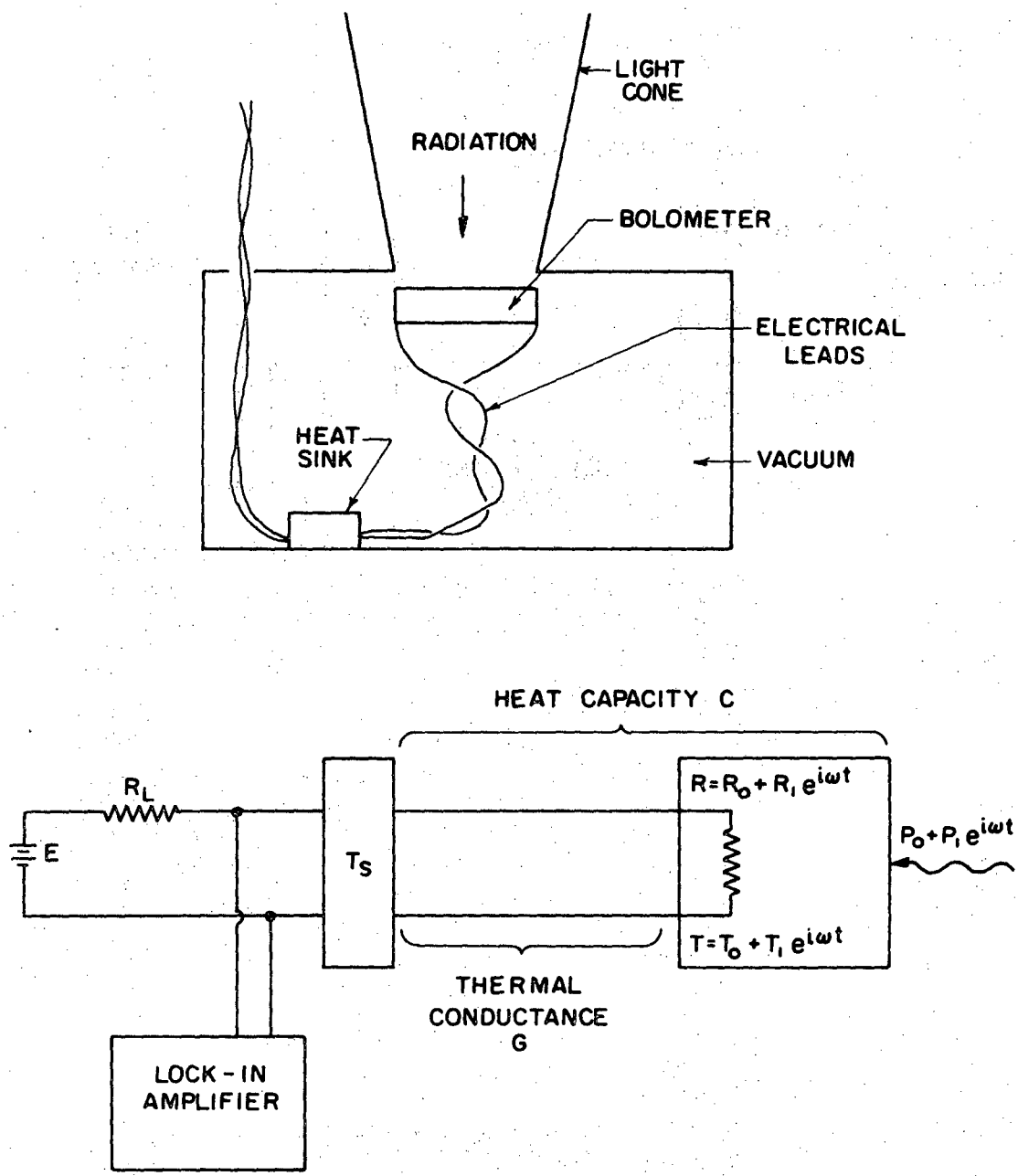

XBL 707-1661

Fig. 5

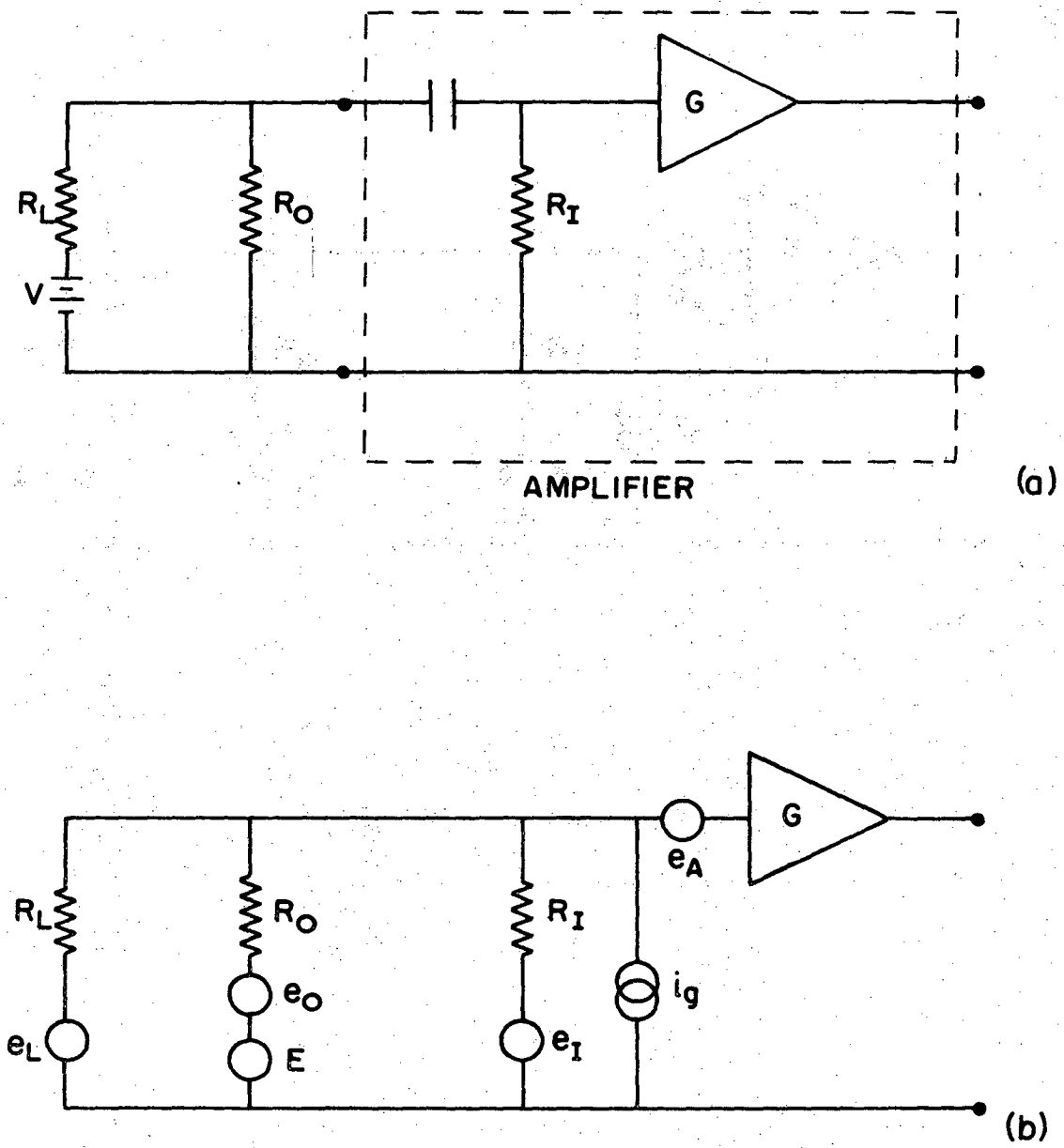

XBL 707-1660

Fig. 6

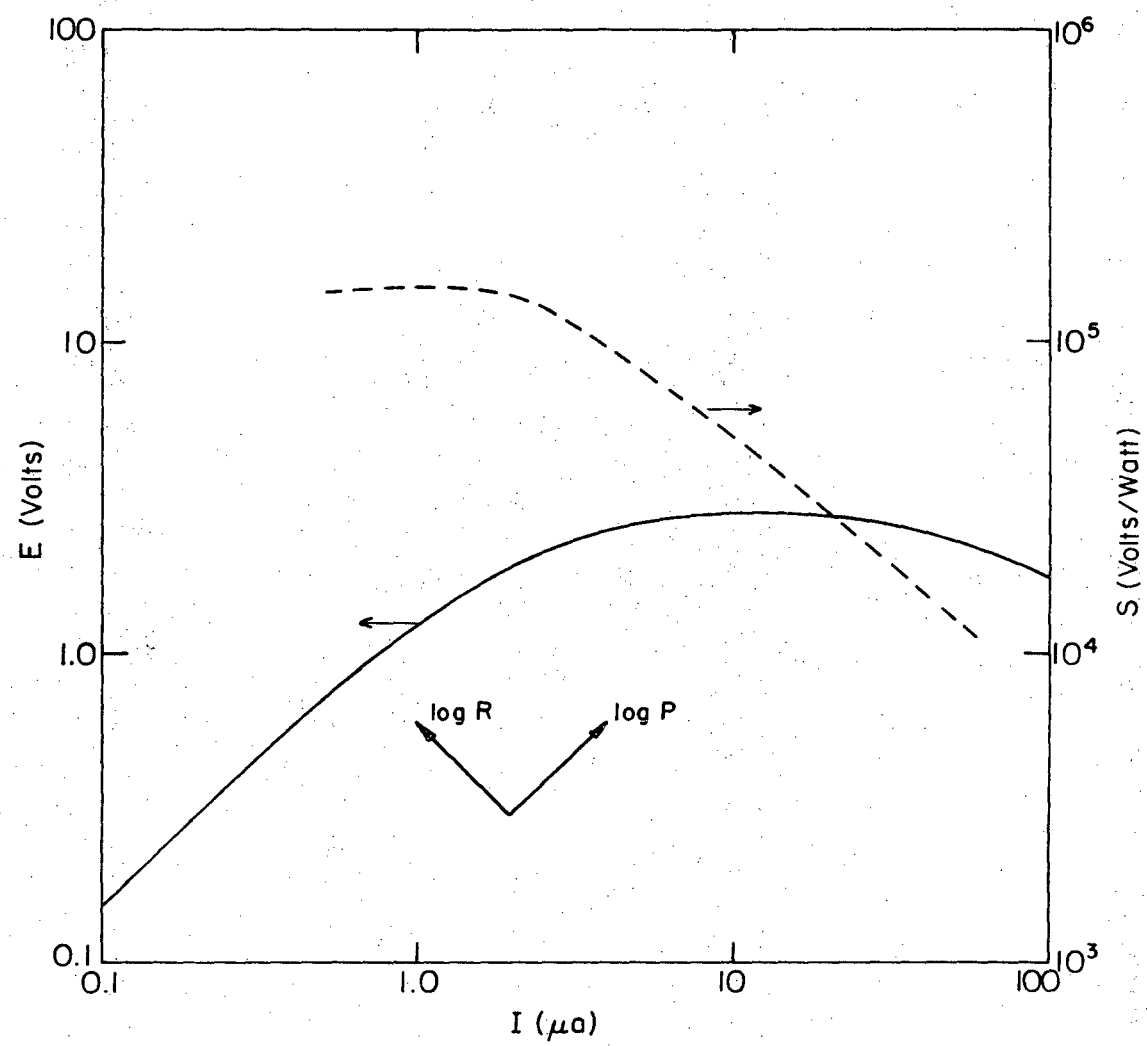

XBL 707-1653

Fig. 7

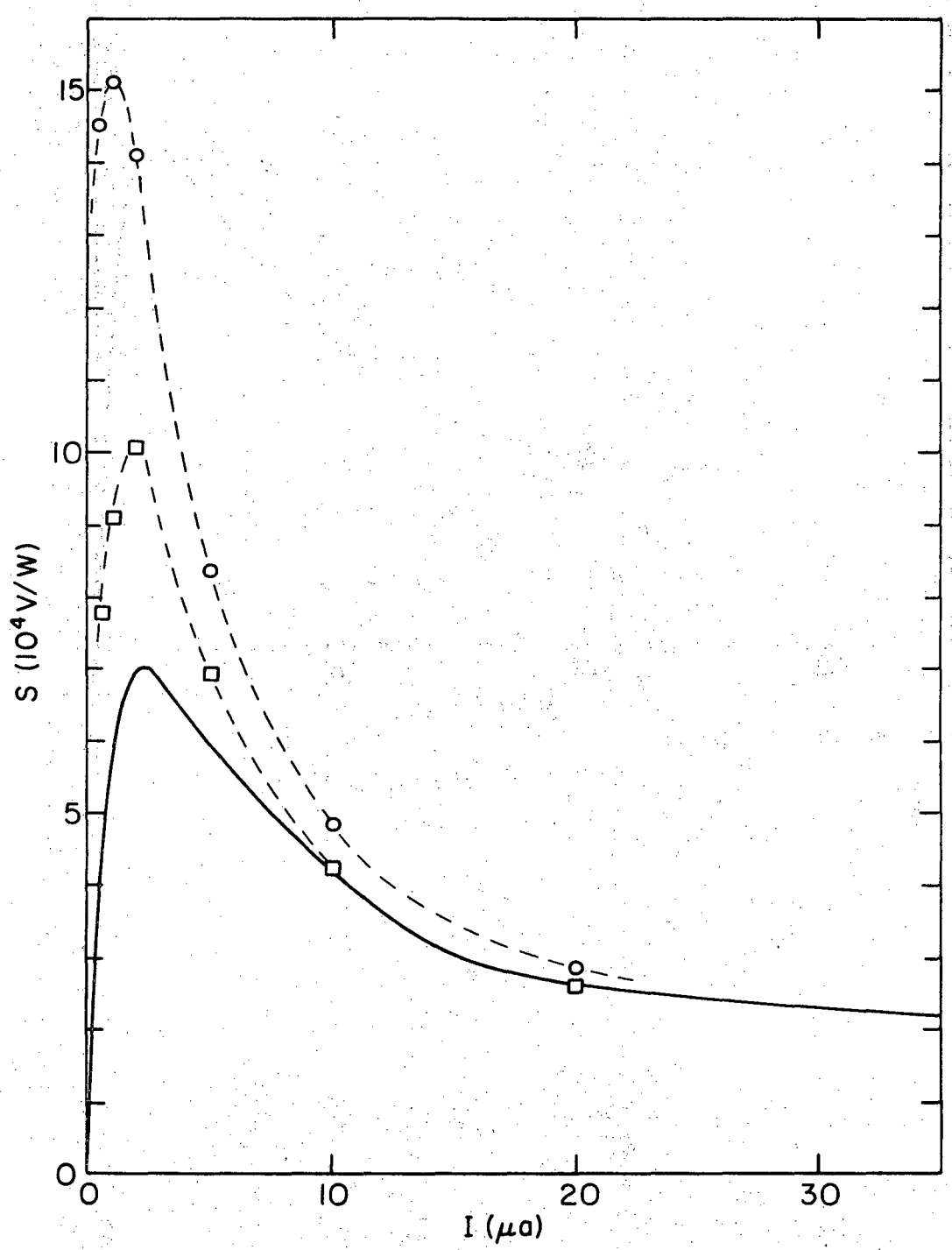

XBL 707-1659

Fig. 8

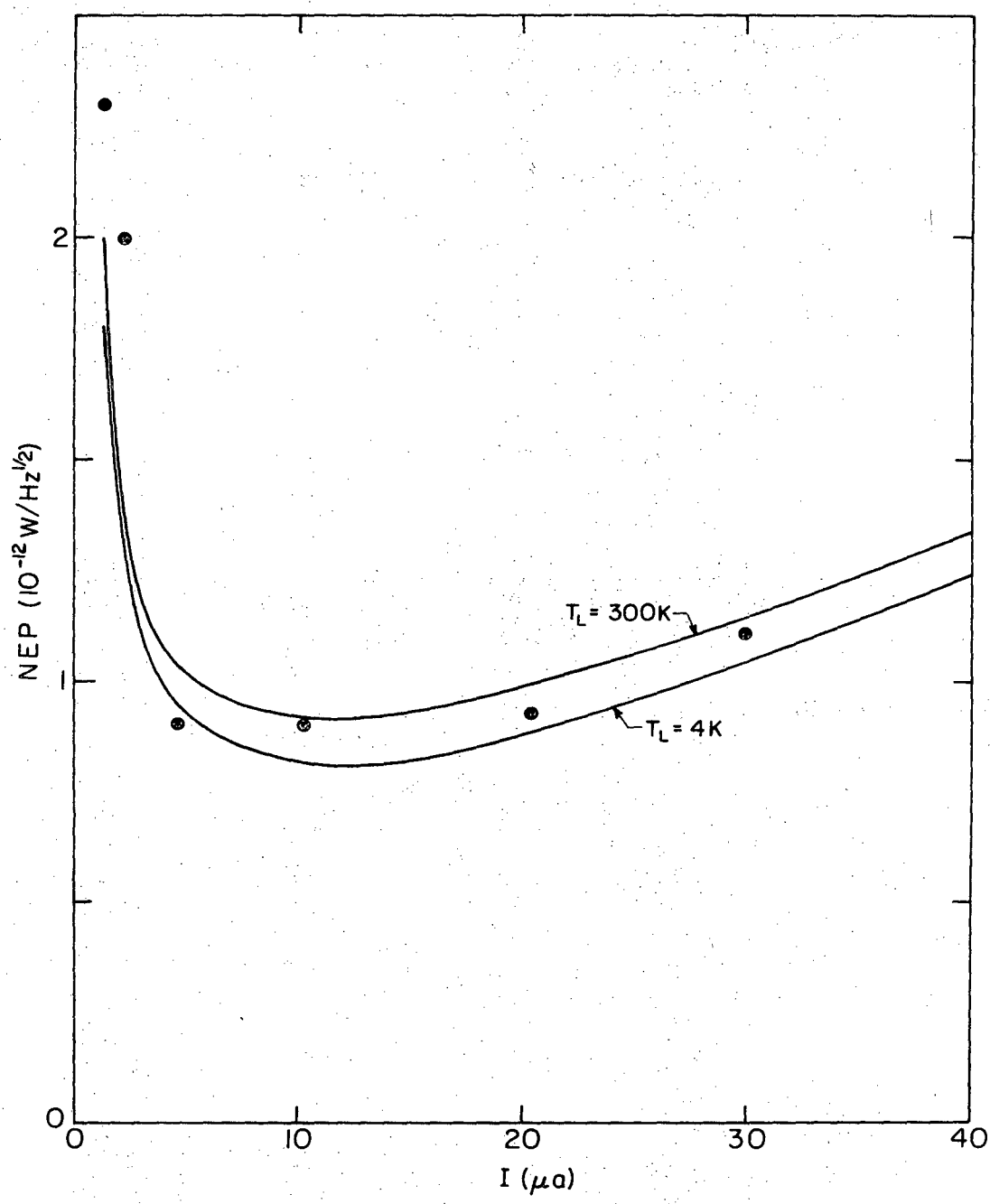

XBL 707- 1650

Fig. 9

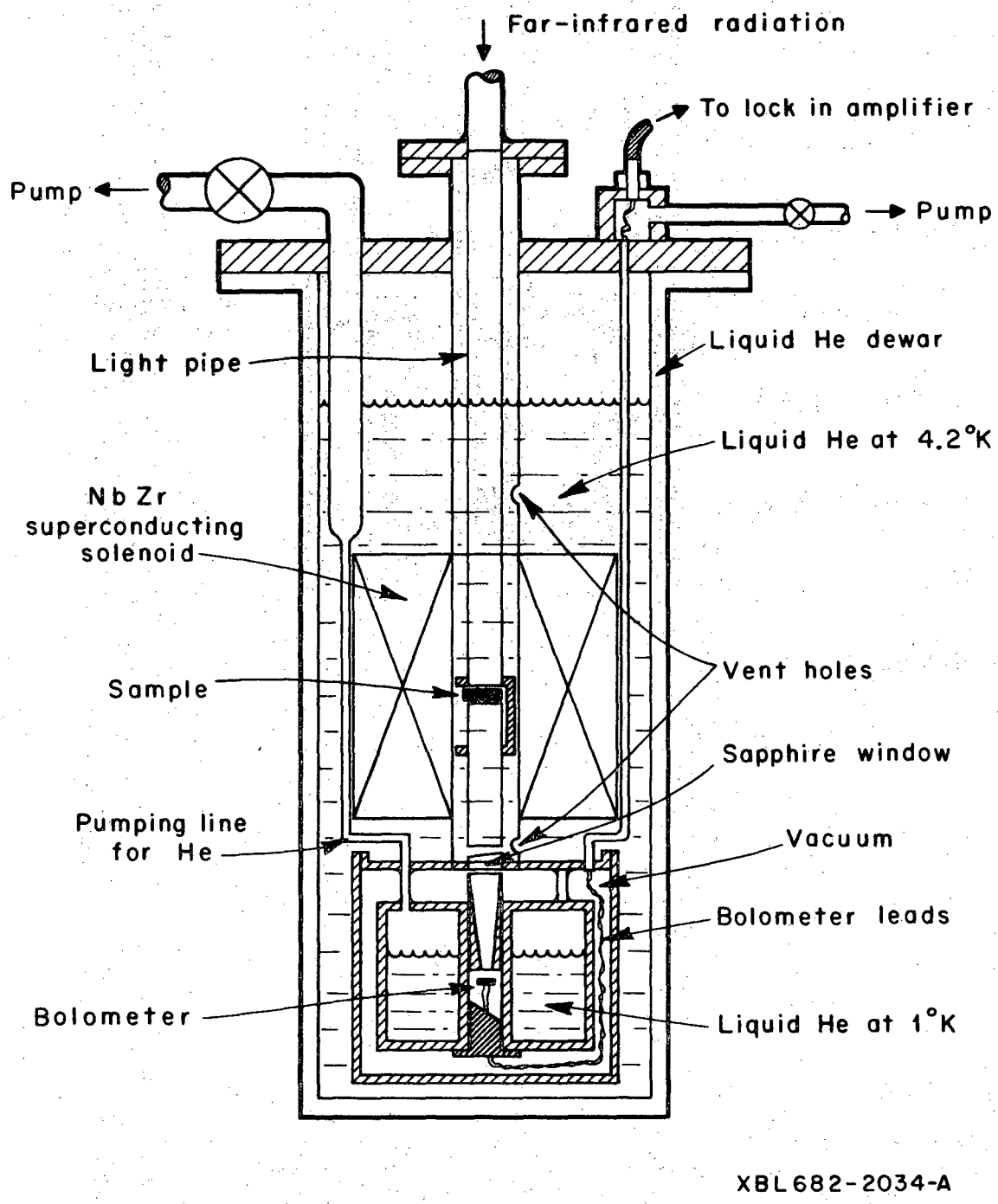
Far-infrared radiation
To lock in amplifier
Pump
Pump
Light pipe
Liquid He dewar
Liquid He at 4.2°K
Nb Zr
superconducting
solenoid
Vent holes
Sample
Sapphire window
Pumping line
for He
Vacuum
Bolometer leads
Bolometer
Liquid He at 1°K
XBL682-2034-A

Fig. 10

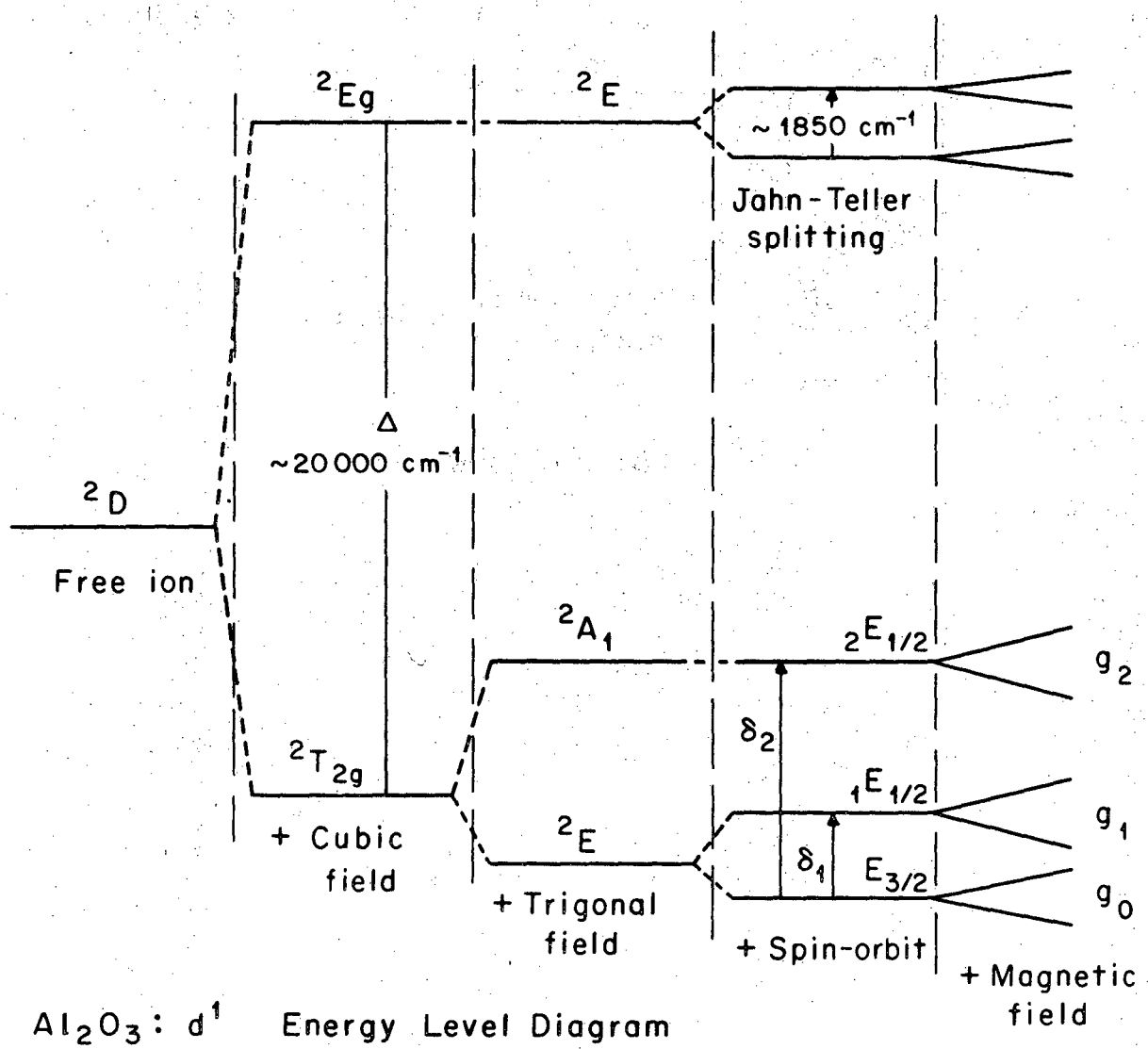

Al_2O_3: d^1 Energy Level Diagram

XBL682-2035

Fig. 11

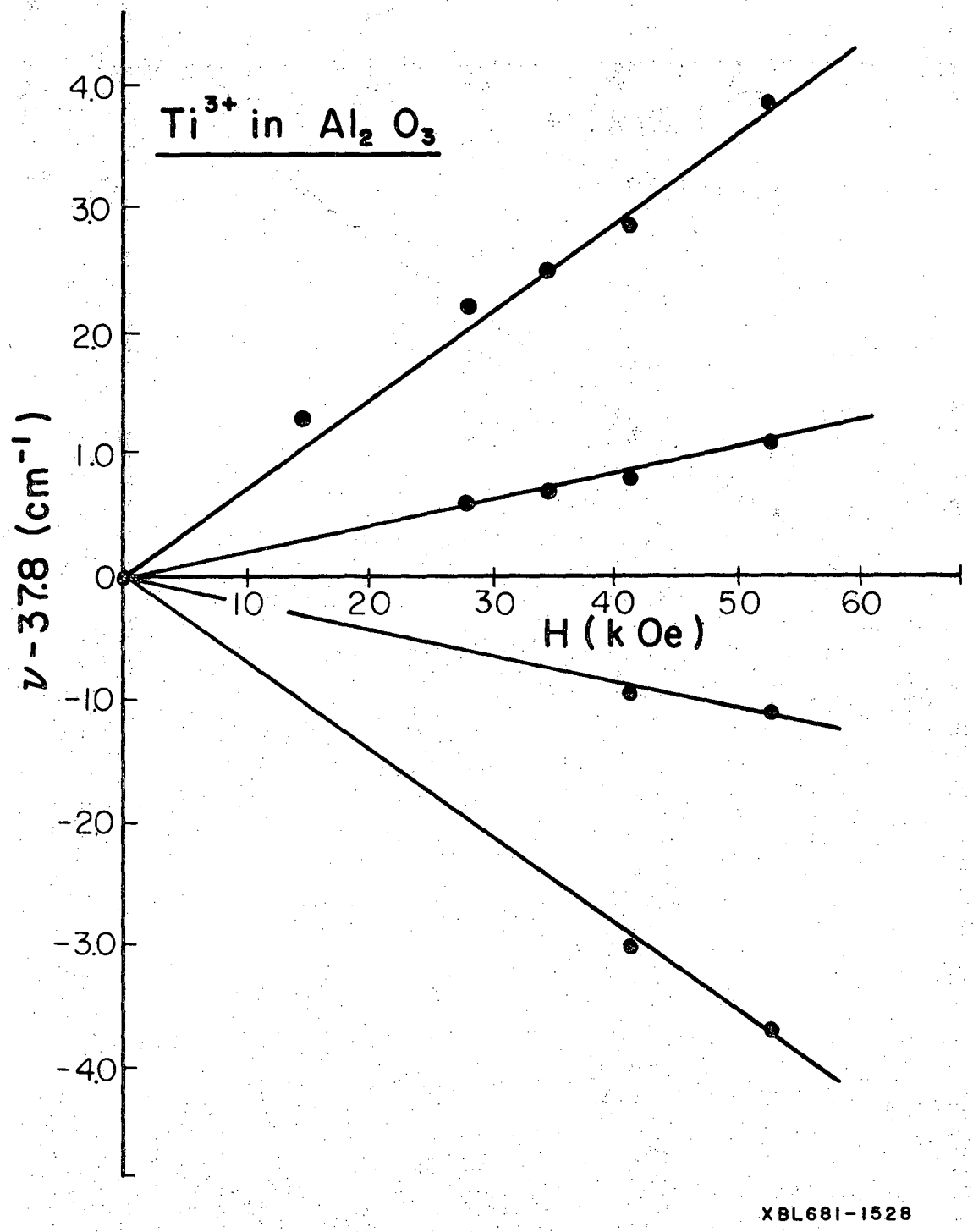
Ti3+ in Al2 O3
4.0
3.0
2.0
1.0
0
-1.0
-2.0
-3.0
-4.0
ν - 37.8 (cm-1)
10
20
30
40
50
60
H (k Oe)
XBL681-1528

Fig. 12

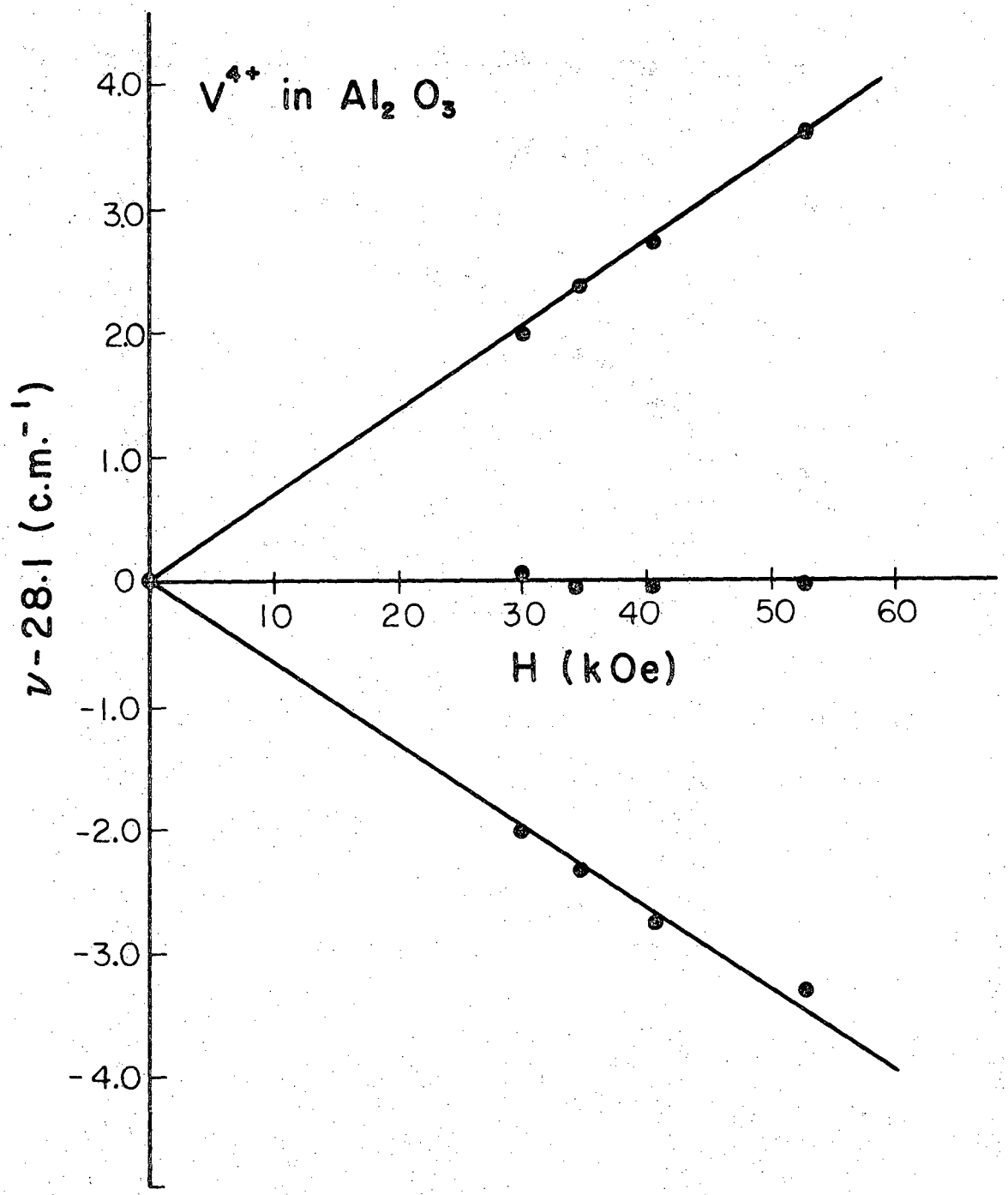

XBL681-1529

Fig. 13

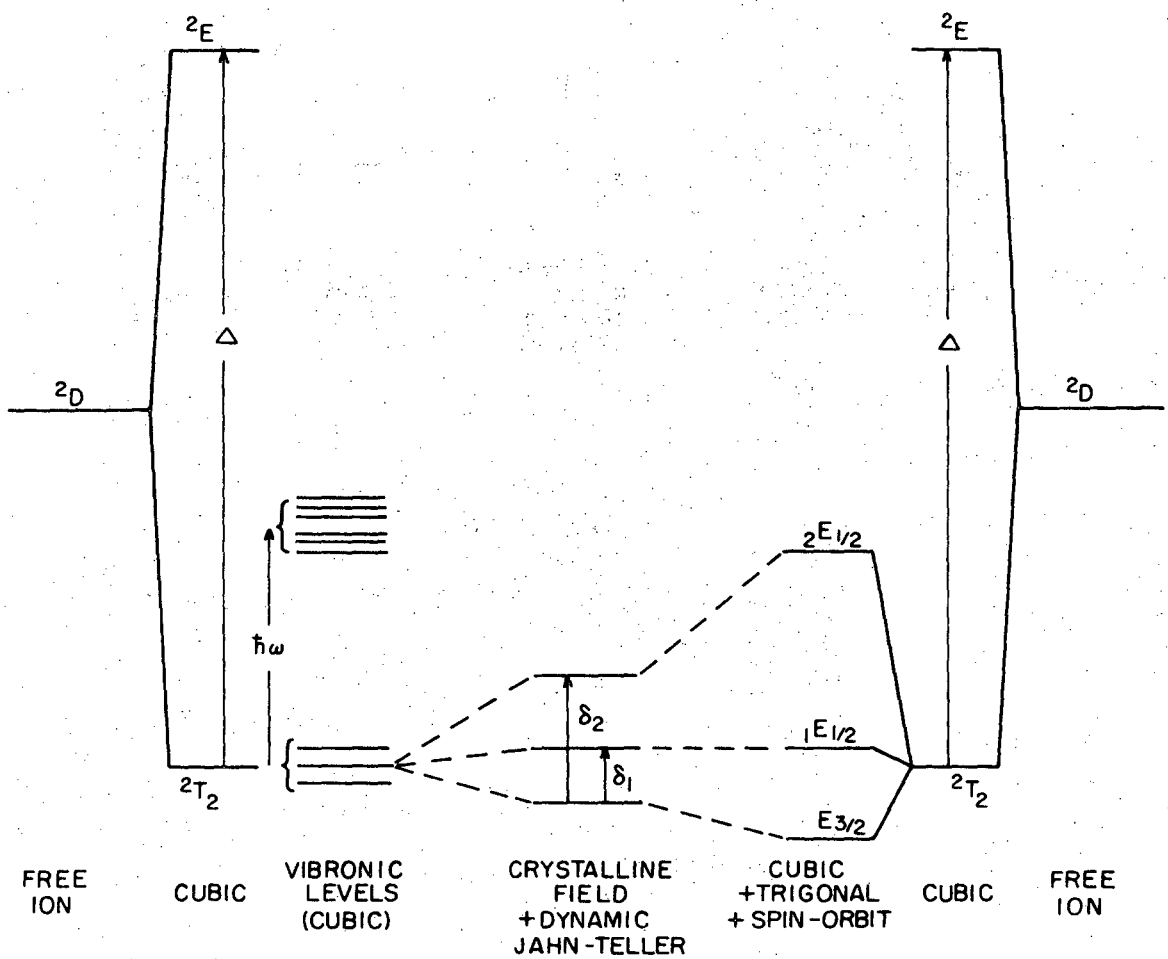

XBL 707-1658

Fig. 14

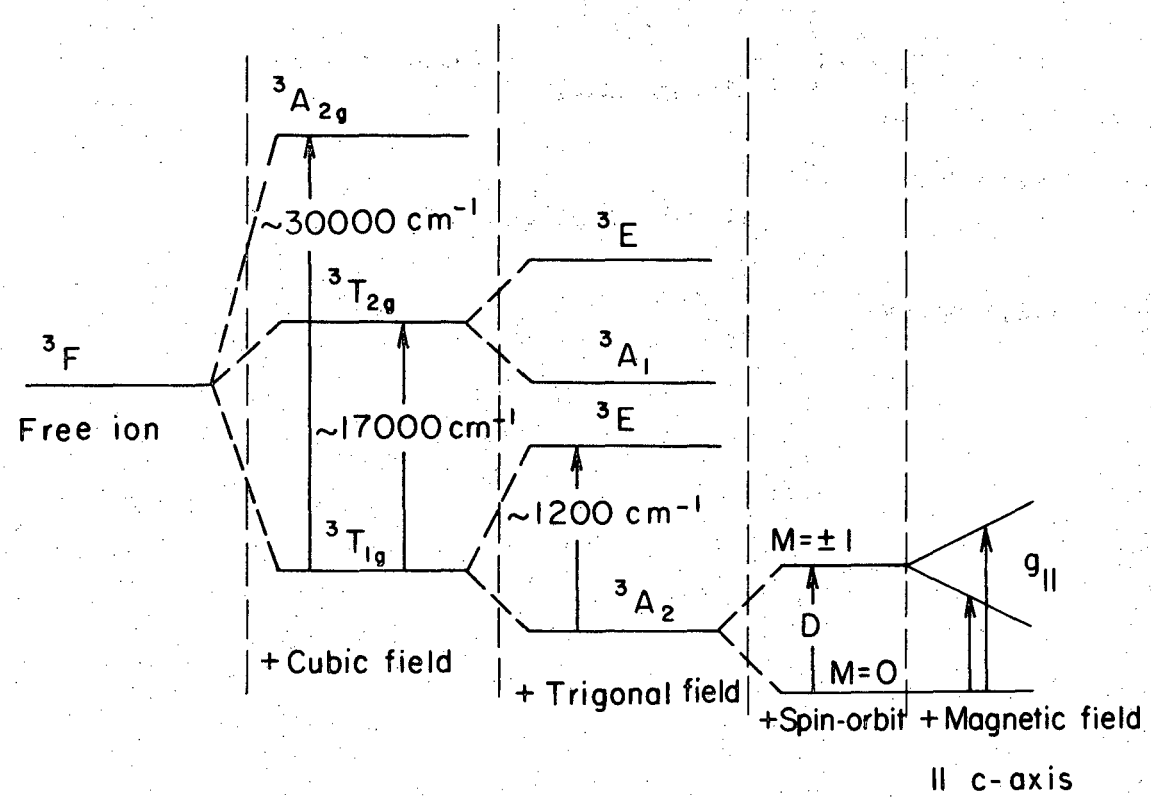

Al_2O_3: d^2 Energy level diagram

XBL684-2514

Fig. 15

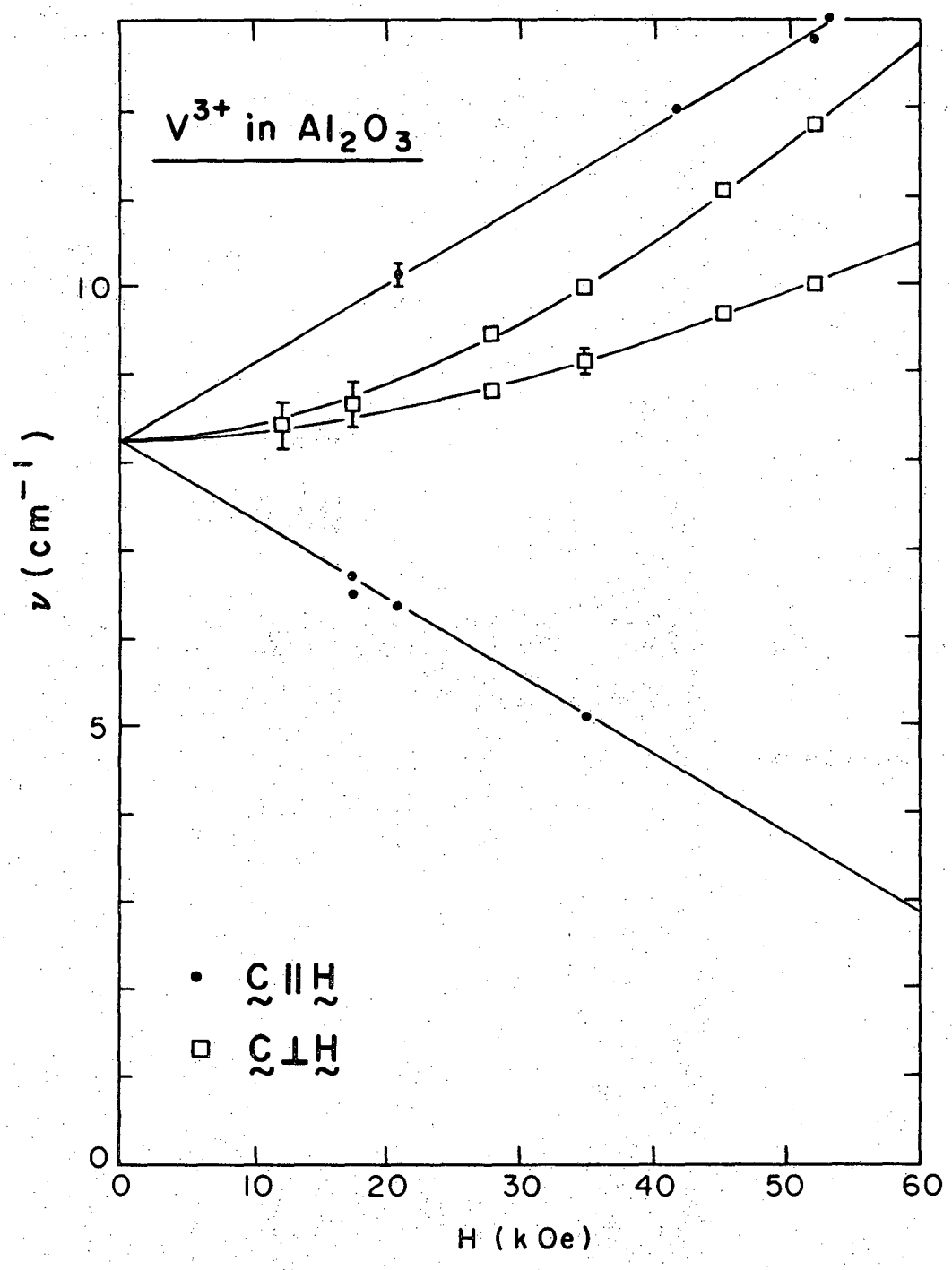

XBL 684-2515-A

Fig. 16

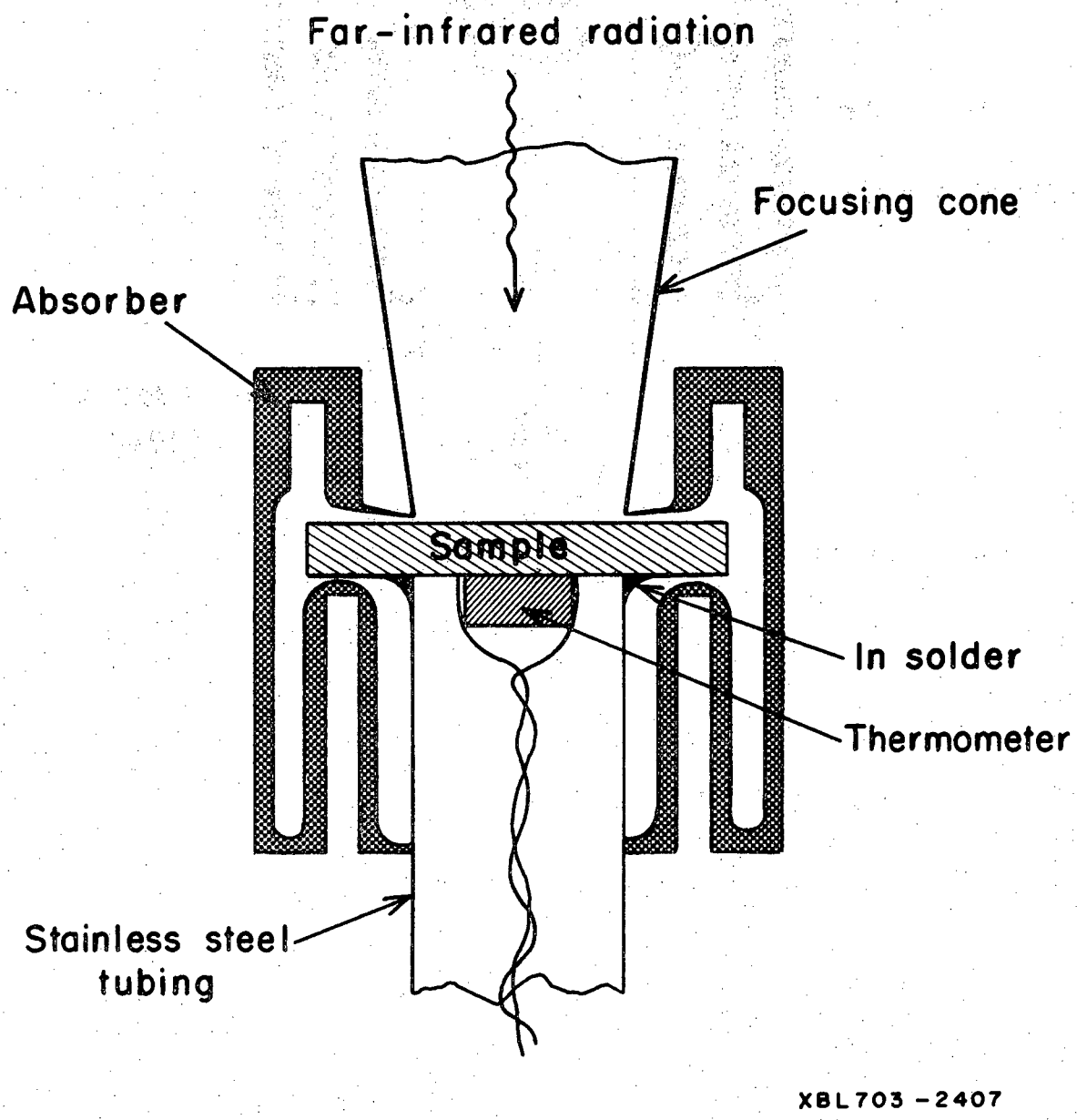
Far-infrared radiation
Focusing cone
Absorber
Sample
In solder
Thermometer
Stainless steel tubing
XBL703-2407

Fig. 17

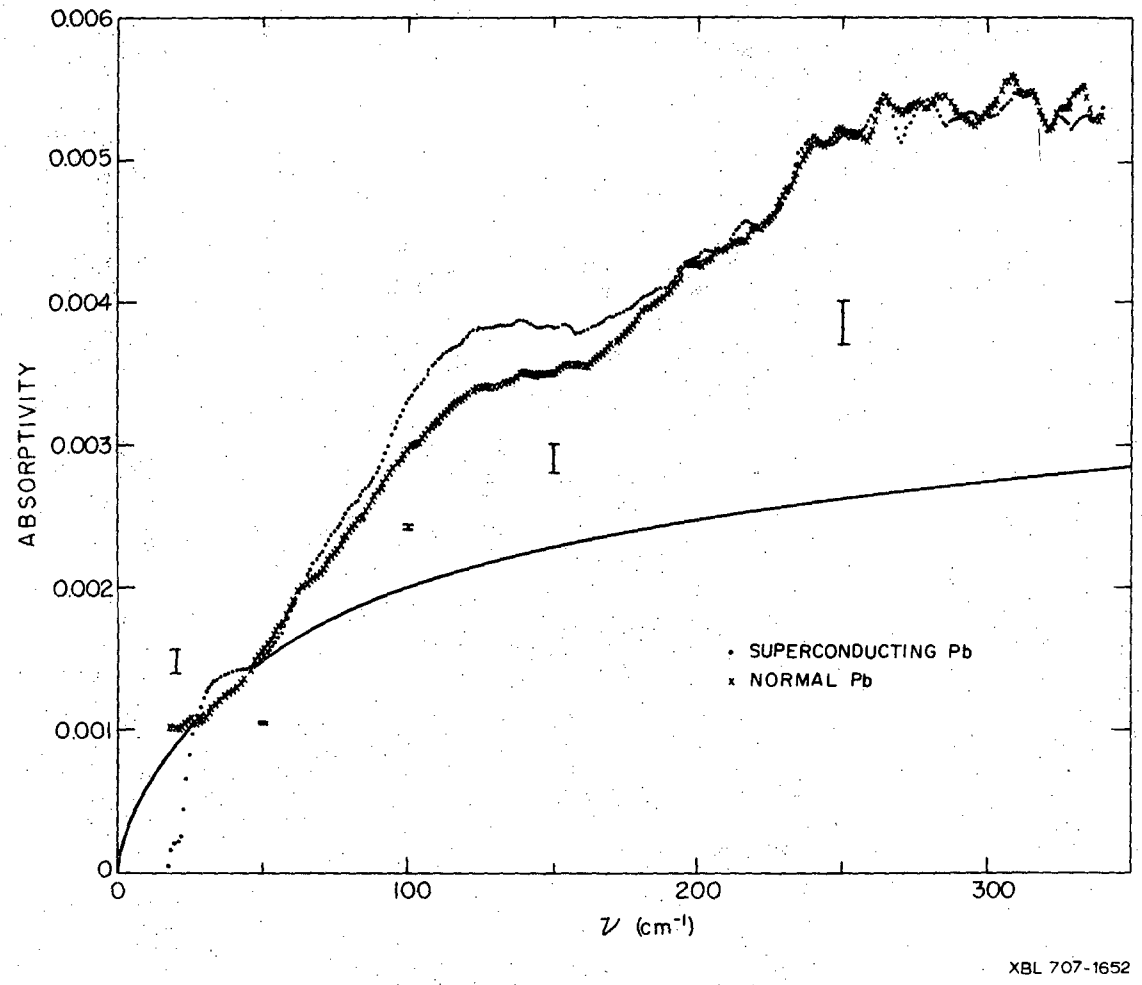
0.006
0.005
0.004
0.003
0.002
0.001
0
ABSORPTIVITY
0
100
200
300
ν (cm⁻¹)
• SUPERCONDUCTING Pb
x NORMAL Pb
XBL 707-1652

Fig. 18

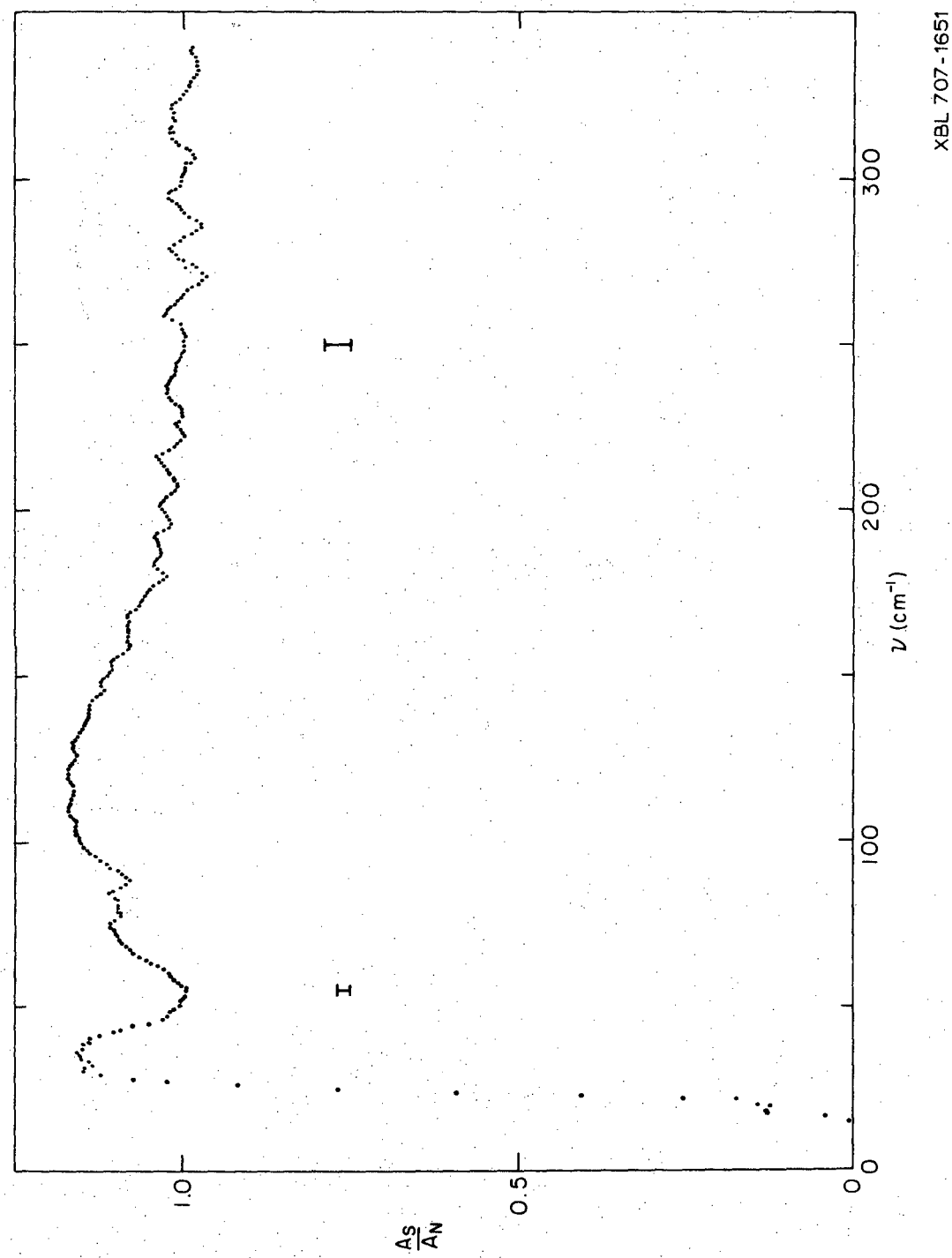

Fig. 19

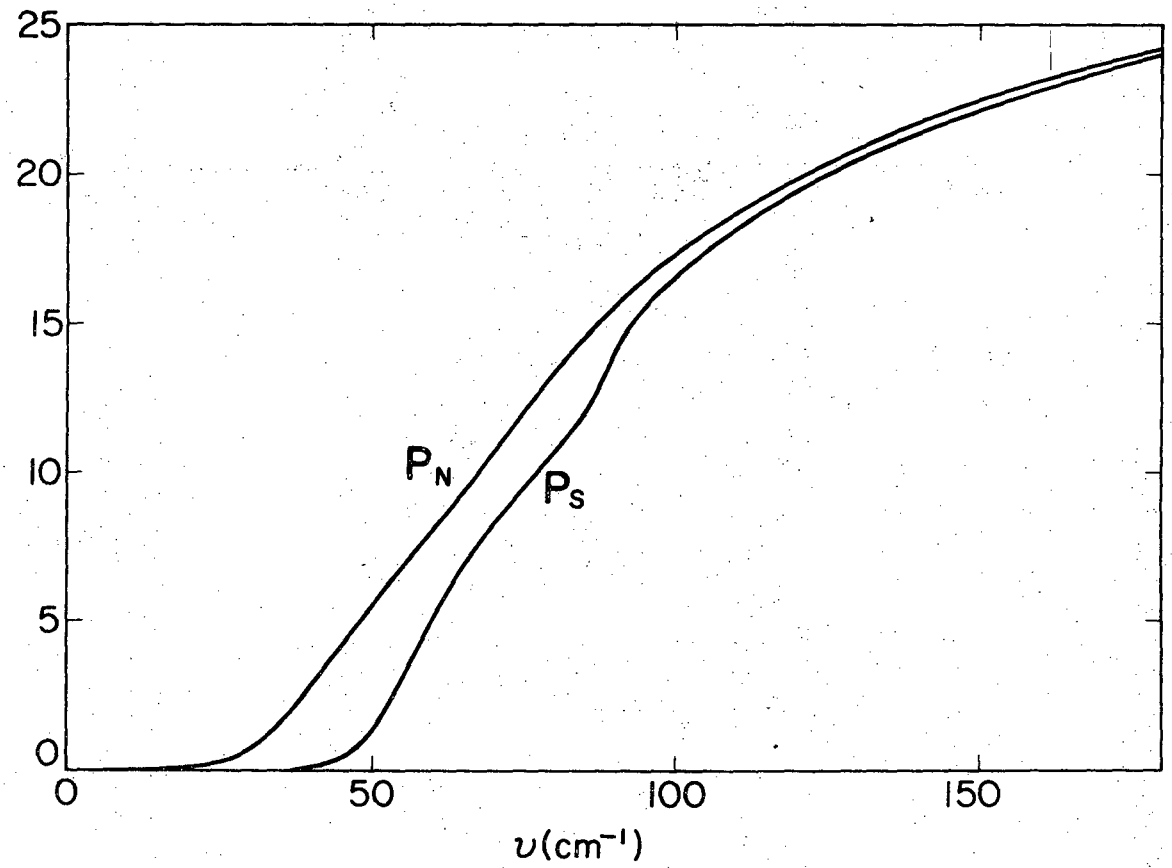

XBL702-2385

Fig. 20

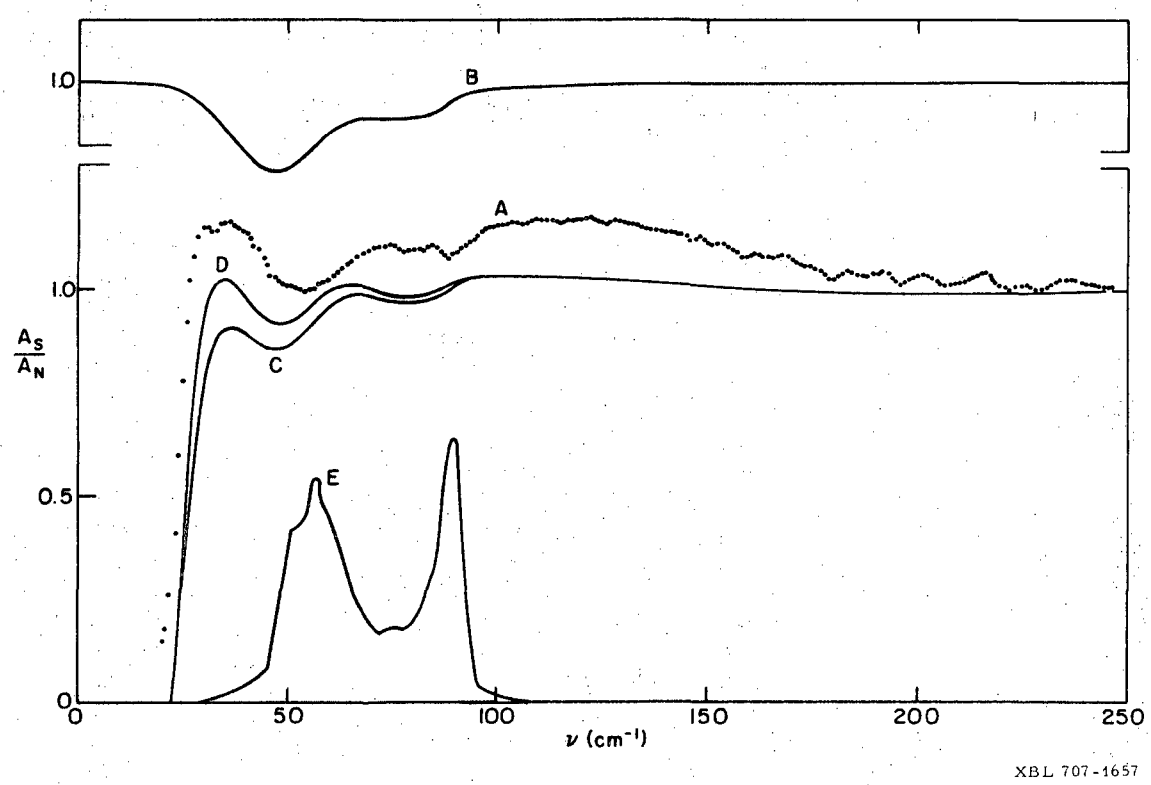

Fig. 21

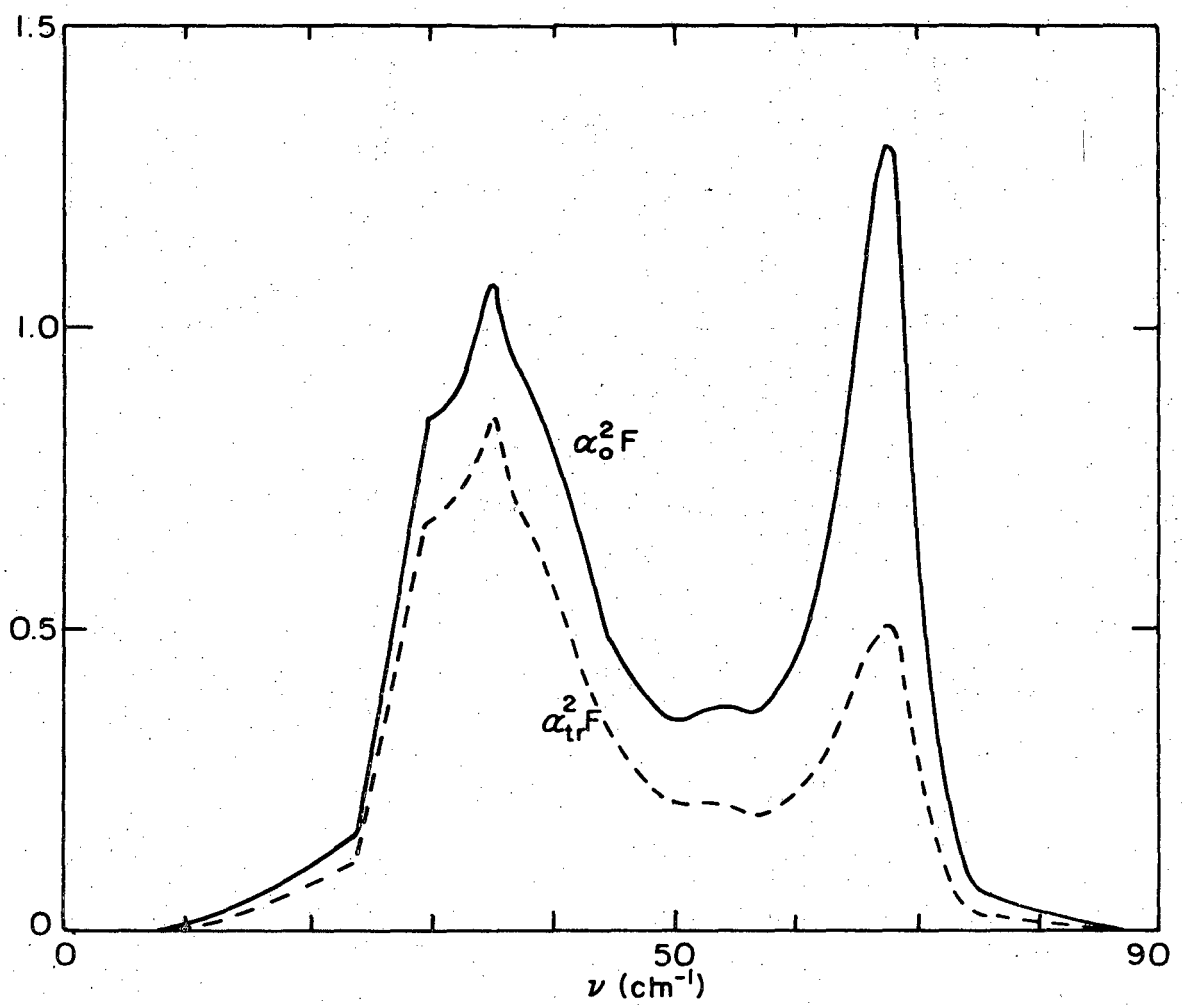

XBL 707-1656

Fig. 22

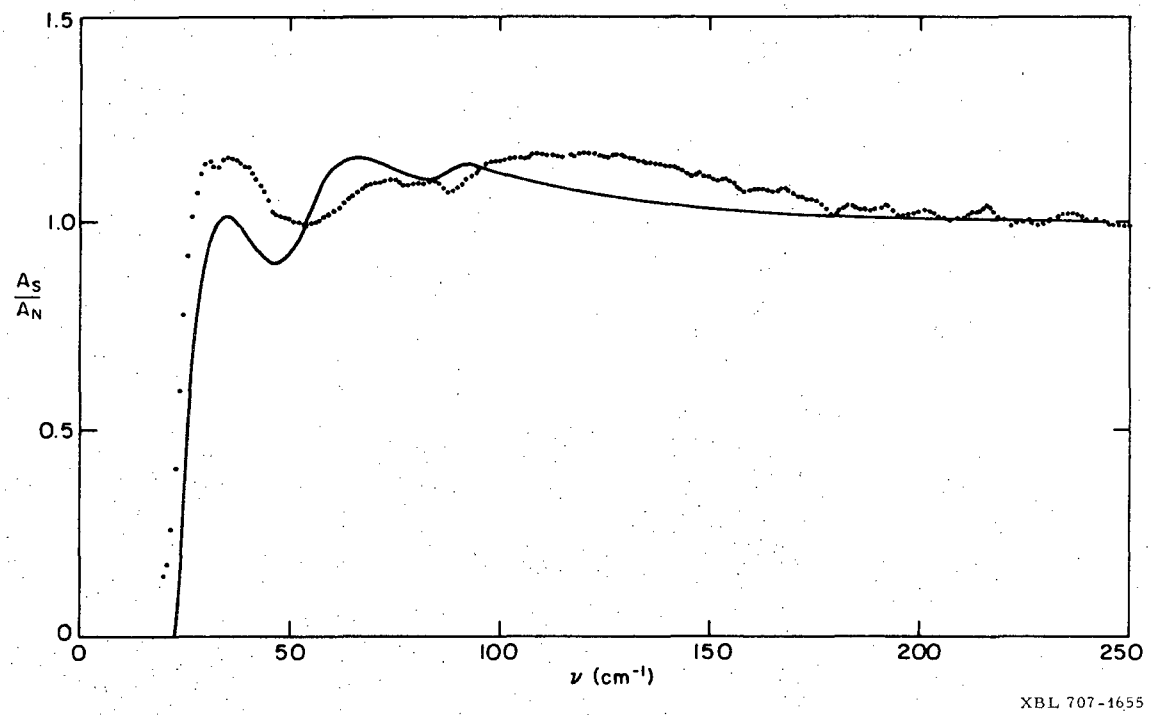

Fig. 23

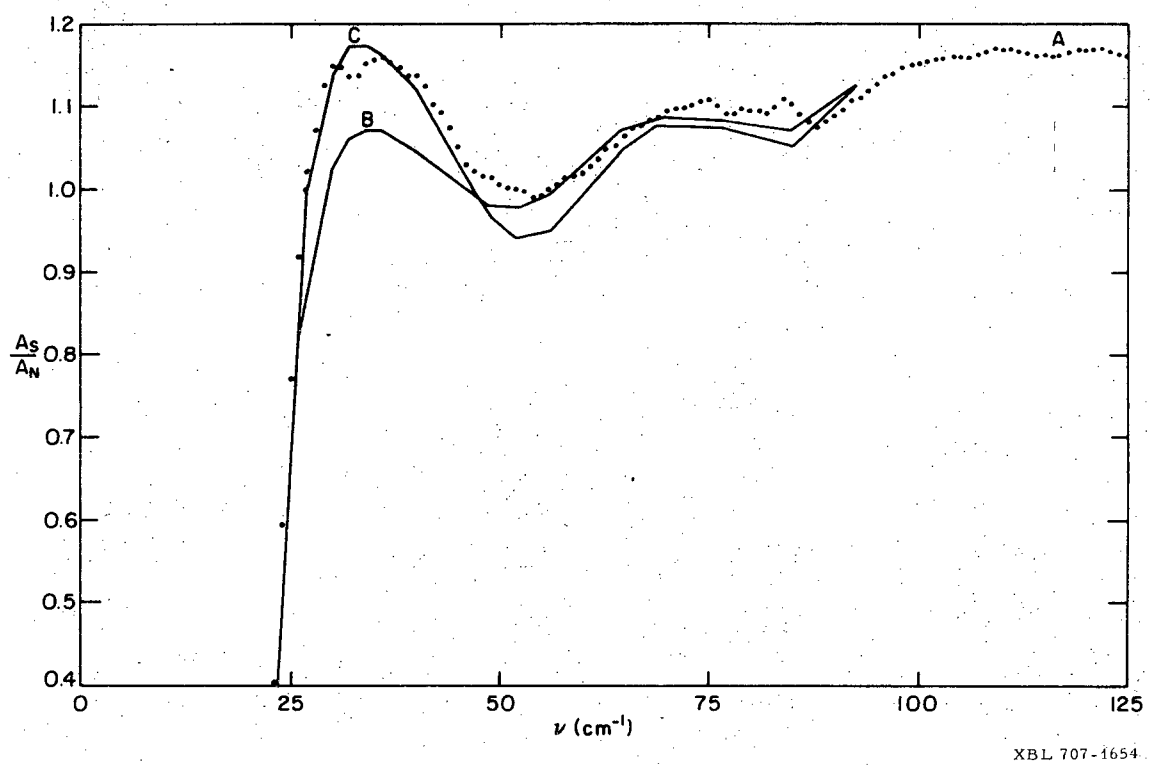
1.2
1.1
1.0
0.9
0.8
0.7
0.6
0.5
0.4
$\frac{A_S}{A_N}$
0
25
50
75
100
125
ν (cm^{-1})
A
B
C
XBL 707-1654

Fig. 24

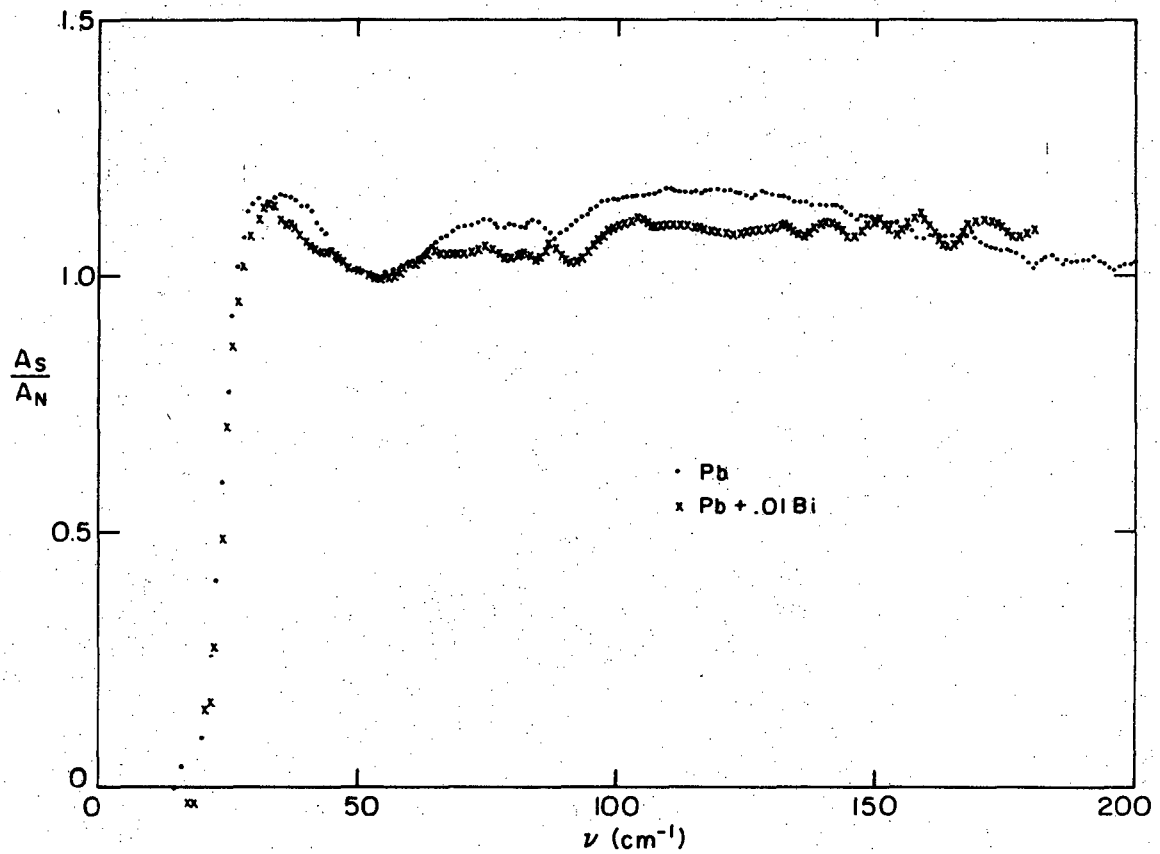

XBL 707-1665

Fig. 25

LEGAL NOTICE

This report was prepared as an account of Government sponsored work. Neither the United States, nor the Commission, nor any person acting on behalf of the Commission:

A. Makes any warranty or representation, expressed or implied, with respect to the accuracy, completeness, or usefulness of the information contained in this report, or that the use of any information, apparatus, method, or process disclosed in this report may not infringe privately owned rights; or

B. Assumes any liabilities with respect to the use of, or for damages resulting from the use of any information, apparatus, method, or process disclosed in this report.

As used in the above, "person acting on behalf of the Commission" includes any employee or contractor of the Commission, or employee of such contractor, to the extent that such employee or contractor of the Commission, or employee of such contractor prepares, disseminates, or provides access to, any information pursuant to his employment or contract with the Commission, or his employment with such contractor.

TECHNICAL INFORMATION DIVISION
LAWRENCE RADIATION LABORATORY
UNIVERSITY OF CALIFORNIA
BERKELEY, CALIFORNIA 94720